Experimental and theoretical investigation of gas purity in alkaline water electrolysis

Doctoral Thesis

(Cumulative Dissertation)

to be awarded the degree

Doctor of Engineering (Dr.-Ing.)

submitted by

Philipp Haug, M. Sc.

from Lindau / Bodensee

approved by the

Faculty of Mathematics / Computer Science and

Mechanical Engineering,

Clausthal University of Technology,

Date of oral examination

25.01.2019

Dean:

Prof. Dr.-Ing. Volker Wesling

Chairperson of the Board of Examiners:

Prof. Dr.-Ing. Armin Lohrengel

Supervising tutor:

Prof. Dr.-Ing. Thomas Turek

Reviewer:

apl. Prof. Dr.-Ing. Ulrich Kunz

Prof. Dr.-Ing. Richard Hanke-Rauschenbach

Abstract

Nowadays hydrogen, which is required in huge quantities for many important industrial processes such as ammonia synthesis, is still being produced through inexpensive, but greenhouse gas emitting processes like steam reforming and coal gasification. In the course of the energy turnaround hydrogen is often seen as the fuel of the future. Within the framework of the power-to-gas concept (PtG), particularly water electrolysis is often discussed as the key technology for future synthesis of hydrogen.

Alkaline water electrolysis has been applied in the industry for decades, but no further research activities have been undertaken for quite some time. For realization and improvement of the PtG concept precise knowledge, especially about the dynamic behavior of the electrolysis process, is indispensable. Usually the acceptable part-load operation of an alkaline water electrolyzer is limited to about 10 % - 40 % of the nominal load. Below this working range the hydrogen quality is significantly reduced through contamination with oxygen, which is also being produced in the process. The increasing hydrogen impurity is mainly based on two aspects. Firstly, the product gases diffuse through the separator into the opposite half-cell to a certain extent. Secondly, the mixing of the hydrogen and oxygen saturated electrolyte leads to a decrease of the product gas quality in the part-load regime as the saturation of the electrolyte is approximately independent of the electrolyzer load. The mixing of the catholyte and anolyte cycle is necessary to compensate an electrolyte concentration gradient which is caused by the occurring half-cell reactions. Particularly through the use of renewable energy sources an intermitting operation of the process may lead to a safety plant shutdown at around 2 vol% H_2 in O_2 in the lower working range. In addition, the current development of alkaline water electrolysis focuses on the increase of the electrolysis pressure to avoid the need of additional mechanical hydrogen compression, which further intensifies the problem of product gas contamination.

In this study, classical mixing of catholyte and anolyte as well as several other electrolyte management concepts are examined with respect to the resulting gas purity. Next to the classical strategy, the complete electrolyte separation or the application of periodic separation-mixing-sequences are conceivable, which promise a reduction of the product gas contamination. In order to investigate these concepts, experiments are carried out in a custom-built laboratory electrolyzer under industrially relevant conditions, which allow an evaluation of the influence of various process parameters and the quantification of the prevailing crossover mechanisms. In addition, a model is being developed that can be used for the support of the experiments and for the optimization of the process.

The results show that a reduction of the electrolyte flow rate and system pressure, an increase of the electrolyte temperature, and an increase of the electrolyte concentration lead to a reduced contamination of the products when the electrolyzer is operated with mixed electrolyte cycles. The analysis of the results further reveals that the main source of contamination is not the permeation of the gases through the separator, but the dissolution in the electrolyte and transport to the other half-cell by electrolyte recycling. Consequently, a significant reduction of gas crossover can be achieved by the separation of the cycles or a dynamic process strategy, which involves a continuous alternation between merged and separated electrolyte cycles. This process management provides an almost constant electrolyte concentration while improving the product gas quality simultaneously.

Kurzfassung

Wasserstoff, der in großen Mengen für viele wichtige industrielle Prozesse wie die Ammoniaksynthese benötigt wird, wird bis heute durch kostengünstige, aber Treibhausgas-emittierende Verfahren, wie die Dampfreformierung oder Kohlevergasung, hergestellt. Im Zuge der Energiewende wird jedoch insbesondere Wasserstoff oft als Kraftstoff der Zukunft angesehen. Im Rahmen des Power-to-Gas-Konzeptes (PtG) wird deswegen die Wasserelektrolyse als Schlüsseltechnologie für die zukünftige Wasserstoffsynthese diskutiert.

Die alkalische Wasserelektrolyse wird technisch bereits seit Jahrzehnten erfolgreich angewendet, ist aber technologisch lange nicht mehr weiterentwickelt worden. Für die Umsetzung und Verbesserung des PtG-Konzeptes sind jedoch genaue Kenntnisse, insbesondere über das dynamische Verhalten des Elektrolyseprozesses, unerlässlich. Normalerweise ist der zulässige Teillastbetrieb eines alkalischen Wasserelektrolyseurs auf etwa 10 % - 40 % der Nominallast beschränkt. Unterhalb dieses Betriebsbereiches wird die Wasserstoffqualität durch die Verunreinigung mit Sauerstoff, der ebenfalls im Prozess entsteht, deutlich reduziert. Die zunehmende Wasserstoffverunreinigung beruht im Wesentlichen auf zwei Aspekten. Zum einen diffundieren die Produktgase durch den Separator in die gegenüberliegende Halbzelle, zum anderen führt die Vermischung des mit Wasserstoff und Sauerstoff gesättigten Elektrolyten zu einer Verminderung der Produktgasqualität im Teillastbereich, da die Sättigung des Elektrolyten von der Auslastung des Elektrolyseurs annähernd unabhängig ist. Die Vermischung des kathodischen und anodischen Elektrolytkreislaufes ist notwendig, um den Konzentrationsgradienten auszugleichen, der durch die ablaufenden Halbzellreaktionen verursacht wird. Insbesondere durch den Einsatz erneuerbarer Energiequellen kann ein intermittierender Betrieb des Prozesses im unteren Lastenbereich zu einer sicherheitstechnischen Abschaltung der Anlage bei etwa 2 vol% H_2 in O_2 führen. Darüber hinaus konzentrieren sich aktuelle Entwicklungen der alkalischen Wasserelektrolyse auf eine Erhöhung des Prozessdrucks, um nachgeschaltete mechanische

Verdichtungsstufen zu vermeiden, was das Problem der Produktgasverunreinigung weiter verschärft.

In dieser Studie werden die klassische Vermischung von Katholyt und Anolyt sowie alternative Elektrolytführungskonzepte hinsichtlich der resultierenden Gasreinheit untersucht. So ist neben der klassischen Prozessführung auch die vollständige Trennung der Kreisläufe oder der Einsatz von periodischen Sequenzen denkbar, die eine Reduzierung der Produktgasverunreinigung versprechen. Um diese Konzepte zu untersuchen, werden in einem eigens angefertigten Labor-Elektrolyseur unter industriell relevanten Bedingungen Experimente durchgeführt, die eine Bewertung des Einflusses verschiedener Prozessparameter und die Quantifizierung der vorherrschenden Crossover-Mechanismen ermöglichen. Zudem wird ein Modell vorgestellt, das zur Unterstützung der Experimente und zur Optimierung des Prozesses eingesetzt werden kann.

Die Ergebnisse zeigen, dass eine Reduzierung des Elektrolytvolumenstroms und des Systemdrucks, eine Erhöhung der Elektrolyttemperatur und eine Erhöhung der Elektrolytkonzentration zu einer geringeren Verunreinigung der Produkte führen, wenn der Elektrolyseur mit zusammengeführten Elektrolytkreisläufen betrieben wird. Die Analyse der Ergebnisse ergibt ferner, dass nicht die Permeation der Gase durch den Separator die Hauptquelle der Kontamination ist, sondern dass die Mischung der Produktgasgesättigten Kreisläufe den einflussreichsten Crossover-Mechanismus darstellt. Somit kann durch die Trennung der Kreisläufe oder eine dynamische Prozessführung eine maßgebliche Reduzierung des gesamten Crossover erzielt werden. Die dynamische Prozessführung sieht hierbei einen kontinuierlichen Wechsel zwischen zusammengeführten und getrennten Kreisläufen vor, welche eine verbesserte Produktgasqualität bei nahezu konstanter Elektrolytkonzentration ermöglicht.

Acknowledgements

I would like to express my sincere gratitude to everyone who contributed to making my years at the Institute so productive and enjoyable.

First of all, I would like to express my extraordinary thanks to my supervisor, Prof. Dr.-Ing. Thomas Turek, who allowed me to work on this interesting subject with a wide range of flexibility and who has always been open to any discussion. I would also like to thank you for the opportunity to attend conferences in foreign countries and to support my stay abroad in the Czech Republic.

My sincere thanks also go to Prof. Dr. Ing. Ulrich Kunz to be reviewer of this thesis and for the ongoing support in experimental matters. It has always been a pleasure to benefit from your tremendous expertise.

In addition to my supervisors, I would like to thank Prof. Dr.-Ing. Richard Hanke-Rauschenbach from Leibniz Universität Hannover for taking over the review of this thesis. Also, I like to thank Petra Ritter for her support and management of numerous organisational matters.

Furthermore, I like to express my special thanks to Matthias Koj for the numerous helpful discussions, the hours spent together in the office and in the laboratory for plant maintenance, as well as countless activities outside of work. Here, my thanks also go to Andreas Köppen and Rafael Kuwertz, who actively supported me at the beginning of my work and familiarized me with the laboratory procedures.

Additionally I like to thank Sebastian Hofmann, who has always been a great support during and outside of work and shared the passion for cycling with me. Our trip across the Alps will remain unforgotten. At this point I also have to thank the other Clausthal cyclists, Matthias Klee, Roland Schmidt and Mauritio Müller. Our trips have always been a pleasure and great fun.

My special thanks also go to my students and later colleagues, Bjarne Kreitz and Jörn Brauns. Your ideas and your enthusiasm were a great support and have contributed significantly to the realization of this work.

Besides, I'd like to thank Jelka Diedenhoven, Malte Bierwirth, Frank Schwering, Katharina Schafner, Aurina Martinez, Can Yilmaz and Jens Friedland for many fruitful discussions during countless cups of coffee and the fun we had outside of work.

Last but not least, I like to thank my long-time fellow student, roommate and friend, Alexander Werner, for the numerous activities and discussions. Without you it wouldn't have been so much fun.

Eventually my special thanks go to my family. Without you my studies would not have been possible in the first place.

And above all, I would like to thank my girlfriend Kathi for her helpful, patient, always supporting, encouraging nature. I wouldn't have gotten this far without you. Thank you!

Contents

1 Introduction

The European Union has set itself the target of reducing greenhouse gas emissions by at least 20 % until 2020 and by 80 % - 95 % until 2050 compared to the level of 1990 [1]. In addition, it was also agreed (EU Directive 2009/28/EC) to increase the share of renewable energies to over 20 % by 2020 [2]. In this context, especially the expansion of solar and wind energy plays an outstanding role. In 2017, the share of these energy sources amounted to 53 % in Denmark, 26 % in Germany and also Ireland, Spain and Portugal could already boast shares of more than 20 %. Worldwide, the installed wind energy capacity increased by 52 GW to 530 GW in total in 2017 [3]. Consequently, due to the intermittent and fluctuating nature of these energy sources, it is inevitable to establish energy storage devices in order to ensure the future stability of our power grid. In Germany, e.g., the residual load is estimated to be 30 GW - 60 GW [4].

While small amounts of energy can temporarily be stored in batteries, flywheels or supercapacitors, chemical storage in the form of hydrogen or methane is particularly suitable for the long-term storage of large amounts of energy. For the emission-free production of hydrogen, the power-to-gas (PtG) concept is discussed, which involves the utilization of surplus renewable energy for the operation of water electrolysis. In a consequent step this hydrogen can then be converted to methane (synthetic natural gas, SNG) by using an external CO or CO_2 source. The produced SNG is applicable for the injection into the gas grid or usable as motor fuel. Alternatively, the direct feeding of hydrogen into the gas grid is also conceivable. However, the permitted proportion of hydrogen is only regulated locally, so that even within the EU varying restrictions between 0 vol% - 12 vol% H_2 can be found [5]. Fig. 1.1 shows a general overview of the PtG concept with possible mass and energy flows. In addition to the possible uses shown in the figure, it is also imaginable to use the hydrogen for fuelling vehicles, for the production of hydrocarbons via Fischer-Tropsch synthesis or other chemicals such as methanol or ammonia [6, 7].

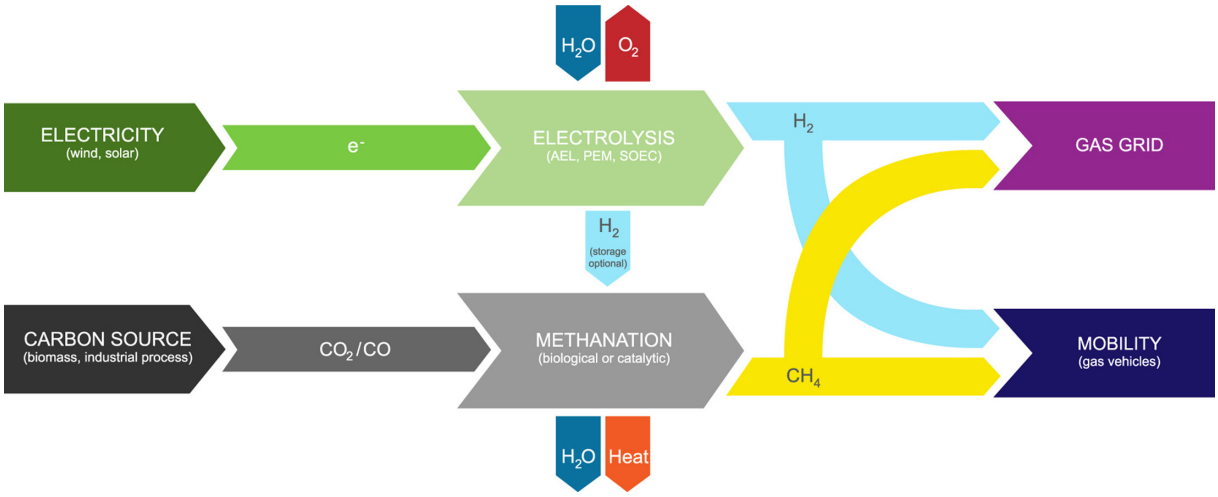

Fig. 1.1: Power-to-gas concept with possible mass and energy flows [4].

As mentioned before, water electrolysis represents the key technology for a successful realization of the PtG concept. In general, water electrolysis can be divided into three different technologies: alkaline, PEM and high-temperature steam electrolysis. These technologies mainly differ in the applied electrolytes and the corresponding half-cell reactions. In addition, all these processes exhibit very different stages of development. In the following, the still more cost-effective methods for the production of hydrogen from fossil fuels are mentioned first, before the various electrolysis technologies are briefly described afterwards.

1.1 Hydrogen demand and production technologies

The global hydrogen demand in 2012 was approximately 600 billion Nm^3 ($\approx$ 54 million tonnes) [8]. It is especially needed in the chemical industry for ammonia production via Haber-Bosch process or petroleum refining [9], which each demand about 45 % of the total production capacity [10]. Today hydrogen is primarily produced by the reformation of natural gas or liquid hydrocarbons. Here, particularly three reforming methods are distinguished: Catalytic steam reforming (CSR), partial oxidation (POX) and autothermal reforming (ATR). A detailed review of these production technologies was published by Holladay et al. [11], who provide the advantages of each technology, state-of-the-art catalyst materials and reaction conditions. Until now, steam reforming of natural gas represents the most economical and established industrial technology for hydrogen production [12]. However, the main downside of this production technology is that depending

on the feedstock 9 t to 12 t of CO_2 are produced per tonne of H_2 [13].

Gasification of coal or biomass represents a further hydrogen production alternative. Using biomass can reduce CO_2 emissions into the atmosphere, since the CO_2 released during gasification has previously been absorbed from the atmosphere and converted by photosynthesis. Furthermore, hydrogen can be produced in a purely biological way by fermentation of biomass or by photobiological processes. However, biological processes are still at an early stage of development and therefore unlikely to become commercially available in the next years [12].

In 2008 96 % of the world hydrogen production was generated from fossil fuels, whereas only the remaining 4 % were produced by water electrolysis as it still cannot compete with the costs of conventional production routes [14]. Thus, production costs between 1.06 € $kg_{H_2}^{-1}$ - 2.08 € $kg_{H_2}^{-1}$ for steam reforming of light hydrocarbons and 1.94 € $kg_{H_2}^{-1}$ - 8.60 € $kg_{H_2}^{-1}$ via alkaline or PEM water electrolysis can be found. The production costs for electrolysis mainly depend on the assumed plant size and the available electrical energy source [12].

1.1.1 Alkaline water electrolysis

Alkaline water electrolysis is the most mature and longest known electrolysis technology for the production of hydrogen. Already in 1789 van Troostwijk and Deiman reported about the decomposition of water into »combustible air« and »life-giving air« [15]. From then on, alkaline electrolysis has continously been developed, so that the first large electrolyzer with a power demand of 125 MW and a production capacity of 27900 Nm^3h^{-1} was already erected in 1927 [12]. Although the technology has been known for a long time, it never found wide deployment, as it could not compete with the production costs of hydrogen from fossil fuels. Nevertheless, alkaline water electrolysis represents the primary electrolysis technology, as it is known for its robustness and longevity and alternative technologies are only slowly being introduced to the market [16].

In general, an alkaline electrolysis cell consists of two nickel-based electrodes, which are immersed in an alkaline electrolyte and are divided by a membrane or porous separator. Usually plates, perforated plates, expanded metals or meshes are applied as anodic and cathodic base materials. As an electrolyte, typically a 20 wt% - 40 wt% KOH solution is used at a temperature between 60 °C - 90 °C to provide a high ionic conductivity [17]. For

the reason of efficiency and safety, the applied separator also has to extend a reasonable ionic conductivity and further needs to keep the product gases apart [18]. Modern alkaline electrolysis cells are assembled according to the zero-gap principle, in which the electrodes are directly pressed onto the separator to minimize the ohmic voltage drop of the cell. A scheme of this assembly is shown in Fig. 1.2.

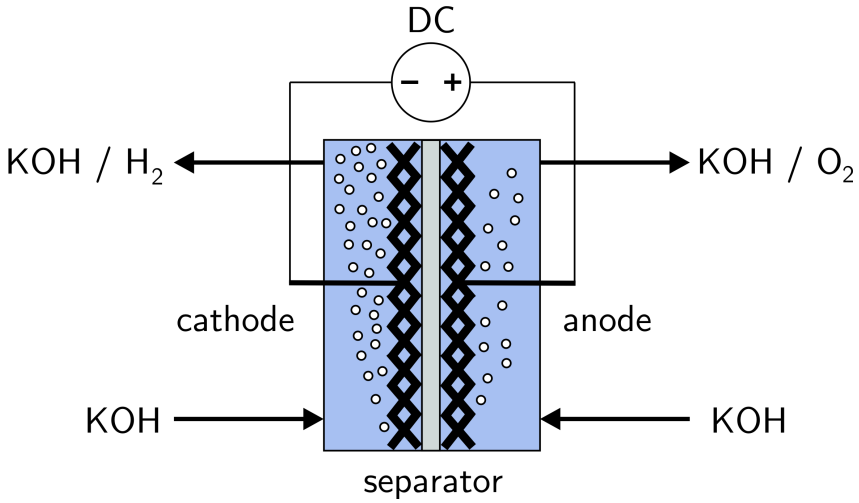

Fig. 1.2: Zero-gap alkaline water electrolysis cell.

Although alkaline electrolysis represents a well-established technology and allows the application of abundant and inexpensive materials, inefficiency is very often associated with it. For this reason, attempts are being made to reduce capital expenses and to improve the process efficiency with new innovative electrode and separator materials [12]. In addition to a high corrosion resistance and electrical conductivity, electrocatalysts must exhibit a high catalytic activity for the desired half-cell reactions, which can be formulated as follows:

$$\text{Cathode: } 2\,H_2O + 2\,e^- \longrightarrow H_2 + 2\,OH^- \tag{1.1}$$

$$\text{Anode: } 2\,OH^- \longrightarrow 0.5\,O_2 + H_2O + 2\,e^- \tag{1.2}$$

$$\text{Overall reaction: } H_2O \longrightarrow H_2 + 0.5\,O_2 \tag{1.3}$$

Under standard conditions, a theoretical cell voltage of approximately $-1.23\,\mathrm{V}$ is required for the electrochemical splitting of water. In practice, however, larger cell voltages are necessary, as in addition to the thermodynamic equilibrium potential, further losses such as the overvoltages at the electrodes, the resistance of the separator and the partially gas-filled electrolyte must be overcome. Typically, the half-cell reactions are referred to as

HER (hydrogen evolution reaction) on the cathode and OER (oxygen evolution reaction) on the anode. Literature [9, 12, 17, 19, 20] provides a large variety of possible materials that can be applied as electrocatalysts for these reactions. Therefore, only a small selection is mentioned here.

Nickel-molybdenum alloys are a famous bimetallic catalyst for the HER. NiMo catalysts can be synthesized in various ways, e.g. production of powders [21], electrodeposition [22], thermal decomposition [23] and also magnetron sputtering [24] is possible. McCrory et al. [25] reviewed several catalyst materials in a recent benchmarking study. It is found that NiMo alloys show excellent catalytic activity under alkaline conditions, even when compared with noble catalyst materials. Other promising HER electrocatalysts include porous Raney nickel or nickel-sulphur alloys [12].

While highly active catalysts have already been found for the HER, OER still remains a major challenge, although it has been studied extensively for years. So, especially metal oxides, e.g. perovskites [26] and spinel oxides [27], have already been the subject of research. Moreover, a growth of interest in hydroxide metals can be observed recently. This is not only the reason, as these kind of catalysts can provide higher activities than metal oxides, but also because metal oxide surfaces are restructured into hydroxide-phases during OER [17]. Typical examples are $LaNiO_3$ as perovskite [28], $NiCo_2O_4$ as spinel oxide [29], nickel-iron-(oxy)hydroxides [30] and also porous Raney nickel [12].

It is the task of the cell separator to prevent short curcuits between the electrodes, to be highly conductive for OH^- ions and to avoid gas crossover. For this purpose, the material needs to be stable under typical operating conditions of alkaline water electrolyzers ($\approx 30\,\mathrm{wt\%}$ KOH, $80\,^\circ\mathrm{C}$, highly oxidizing and reducing conditions at the electrodes [12]). For a long time asbestos-containing materials were used as separators. However, asbestos is not stable under these demanding conditions and was further banned for use by the EU [31] in 1999 as it is classified a carcinogenic material. Today, the porous separator »Zirfon$^{\mathrm{TM}}$ Perl UTP 500« represents the state-of-the-art. It consists of a polysulphone network and an inorganic zirconium oxide filler and is reported to be stable in strong alkaline solutions and up to $110\,^\circ\mathrm{C}$ [32]. However, other materials such as sintered nickel oxide [33] or polyantimonic acid [34] were also investigated for the application as separator in alkaline water electrolysis. In the future a further separator improvement can be expected from the development of anion exchange membranes [35] and ion-solvating

alkaline membranes [36, 37].

Carmo et al. [18] identify three major issues with alkaline water electrolysis: Low partial-load range, limited current density and low operating pressure. Particularly the partial-load capability represents an important safety issue when alkaline water electrolyzers are to be coupled with renewable energies and is therefore the fundamental problem of this work. However, before discussing this issue in more detail in chapter 1.2, a brief excursion into alternative electrolysis technologies is provided for the sake of completeness.

1.1.2 PEM water electrolysis

In contrast to alkaline water electrolysis, proton-conducting (H^+ ions) polymeric membranes are applied as electrolyte in PEM electrolysis. Accordingly, in the literature »PEM« can be found as an abbrevation for proton exchange membrane or polymer electrolyte membrane. Occasionally »solid polymer electrolyte« (SPE) electrolysis is also used as a synonym. Similar to the alkaline technology, PEM electrolyzers are operated below 100 °C, so that a temperature between 50 °C - 80 °C represents the usual operating range [18]. The principle design of a PEM electrolysis cell is depicted in Fig. 1.3.

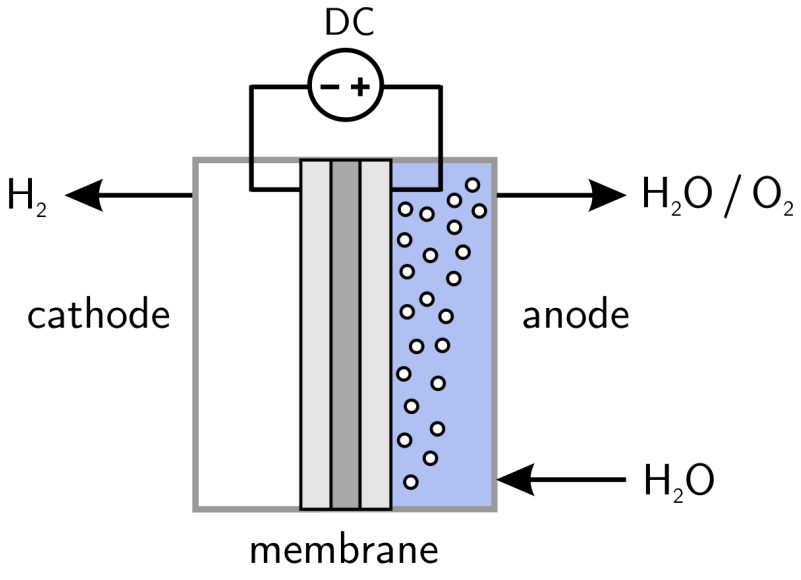

Fig. 1.3: Scheme of PEM electrolysis cell.

Typically, liquid deionized water is supplied to the anodic half-cell, where it is split into its components. While the evolving gaseous oxygen leaves the electrolysis cell, protons pass through the membrane into the cathodic chamber, where the hydrogen evolution

takes place. The corresponding half-cell reactions are shown in Eqs. (1.4) and (1.5).

$$\text{Cathode:} \quad 2\,H^+ + 2\,e^- \longrightarrow H_2 \tag{1.4}$$

$$\text{Anode:} \quad H_2O \longrightarrow 2\,H^+ + 0.5\,O_2 + 2\,e^- \tag{1.5}$$

The centerpiece of most PEM electrolysis cells is the membrane electrode assembly (MEA), which describes the direct coating of porous catalytically active electrodes onto the membrane. The electrical connection to the MEA is typically realized by porous current distributors on both sides, which need to be permeable for the transport of product gases and water and commonly consist of sintered titanium particles [8, 12]. The current distributors are clamped between bipolar plates with flow fields, which provide the electrical connection, enable the transport of liquid water and product gases from and to the electrodes and also separate adjacent cells.

In PEM electrolysis, Nafion®, a sulfonated tetrafluoroethylene based fluoro-polymer-copolymer, represents the most widely employed and famous membrane material today. Nafion® is preferred as it is thin ($\approx 20\,\mu m$ - $300\,\mu m$), ensures high proton conductivity and allows differential pressure operation between anode and cathode. Since the environment is strongly acidic in vicinity to the membrane, catalysts are particularly limited to noble platinum group metals (PGM) to resist the harsh corrosive conditions. The cathodic half-cell reaction is typically promoted by carbon-supported platinum nanoparticles (Pt/C), whereas the OER is catalyzed by ruthenium or iridium oxide based materials [18]. This is one of the biggest disadvantages of PEM electrolysis, as iridium only occurs with an average mass fraction of 1 ppb in the earth's crust. Even platinum is 10 times more abundant [38]. However, significantly higher current densities can be achieved than in alkaline electrolysis. Thus, a current density between $10\,kA\,m^{-2}$ - $30\,kA\,m^{-2}$ below 2 V represents the current state-of-the-art [17, 39]. Consequently, higher voltage efficiencies allow for a more compact system design [40]. Another advantage, which is often associated with PEM electrolysis, is an increased partial load capability [8, 18, 41] in comparison to alkaline water electrolysis, as a lower gas crossover is postulated. However, experimental studies in this thesis allow a contrary conclusion.

PEM electrolysis is increasingly finding its way into the market, with the result that larger projects have already been realized. An example is the »Energiepark Mainz«, where three PEM electrolyzers with a maximum output of 2 MW each are used to produce hydrogen using renewable energy provided by wind turbines [42, 43].

1.1.3 High-temperature steam electrolysis

In contrast to the aforementioned technologies, high-temperature steam electrolysis (HTSE) or solid oxide electrolysis (SOEC) operates in a temperature range between 500 °C and 1000 °C [44]. These high temperatures are advantageous, as electrochemical kinetics are faster and the electrical power demand for splitting of steam is significantly reduced. So, already in 1985 the operation of single cells at $3\,\mathrm{kA\,m^{-2}}$, 1.07 V and 995 °C was successfully demonstrated [45]. However, a operation in this range also involves major challenges. Thus, poor long-term stability and fabrication or material issues are often associated with HTSE. Therefore, research on reduced cell temperatures (500 °C - 700 °C) is gaining more and more attention as material problems are reduced and additional heat energy sources become available [44].

In principle, a SOEC consists of three ceramic layers: two porous electrodes and a dense electrolyte, which simultaneously fulfills the tasks of a membrane. Under given conditions, the applied materials are capable of conducting O^{2-} ions to form a closed electrical circuit. While yttria-stabilized zirconia (YSZ) represents the current state-of-the-art electrolyte material, most commonly Ni/YSZ as cathode and a mixture of YSZ and strontium-doped lanthanum manganite (LSM) as anodic material is found [12]. The basic setup of a SOEC is shown in Fig. 1.4, while the half-cell reactions taking place at the electrodes are given in Eq. (1.6) and Eq. (1.7):

$$\text{Cathode:} \quad H_2O + 2\,e^- \longrightarrow H_2 + O^{2-} \tag{1.6}$$

$$\text{Anode:} \quad O^{2-} \longrightarrow 0.5\,O_2 + 2\,e^- \tag{1.7}$$

It is important to outline, that HTSE represents the least mature electrolysis technology among the presented possibilities and is therefore still at an early stage of development.

1.2 Objective of the thesis

The limited partial load capability of alkaline water electrolysis constitutes a key problem that has to be addressed for a successful realization of the PtG concept. To this day, the partial load operation is usually limited to 10 % - 40 % of the nominal load by the manufacturers [18, 46]. Below this operating regime generated product gases are being

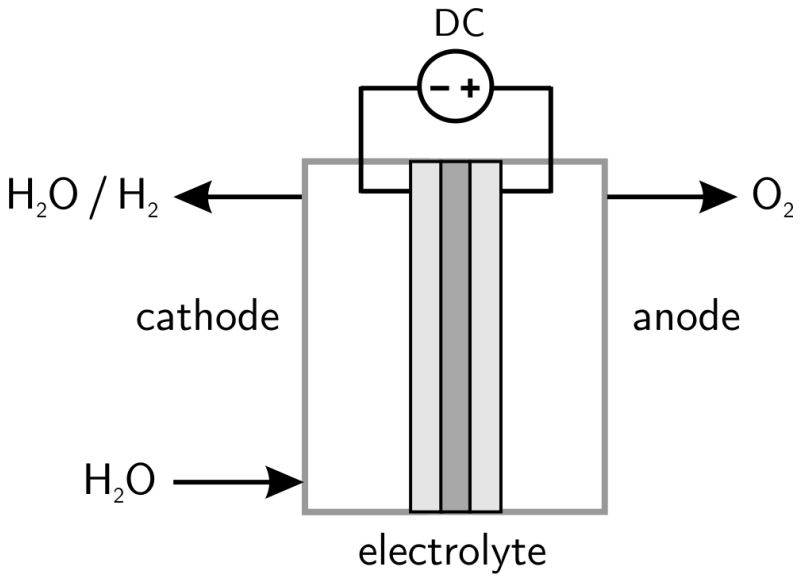

Fig. 1.4: Scheme of high-temperature steam electrolysis cell.

significantly contaminated with the respective other gas, which causes safety problems due to the formation of explosive mixtures. Therefore, this work has the target to identify the mechanisms responsible for gas crossover, to evaluate the influence of various process parameters on these mechanisms and to derive optimization potentials for an extension of the partial load regime.

For this purpose, a lab-scale electrolyzer was set up, which allowed for the experimental determination of the resulting gas purities under atmospheric electrolysis conditions. The experiments were supported by a newly developed and validated stationary, mathematical model, which helped to identify significant influencing factors and optimization measures. In addition, a high-pressure electrolysis cell was designed and manufactured as part of this work, which was later operated in a commercial plant to also investigate the influence of electrolysis pressure on gas crossover.

The present thesis is structured into published manuscripts, which each contribute to the overarching question of this work as follows:

- **Chapter 3** broadly describes the atmospheric experimental setup and electrolysis cell. The experiments carried out here provide an understanding of the influence of diverse process parameters on the product gas quality and allow the deduction of optimized operating conditions. In addition, the experimental proof of a dynamic process management strategy is shown, which could extend the partial load range. Furthermore, an insight into the modelling of gas solubility in highly concentrated

electrolyte solutions is given.

- **Chapter 4** presents a stationary process engineering modelling approach for the overall alkaline electrolysis process. Initially, the model concept is described in detail before a sensitivity analysis and comparison with experimental data is shown afterwards. The model allows a comprehensive insight into the influencing process parameters and thus also provides the possibility to derive optimization potentials.

- **Chapter 5** is intended to point out the significant influence of electrolysis pressure on gas crossover in alkaline water electrolysis and to further provide a fair comparison with PEM electrolysis data. For this purpose, the experimental setup and high-pressure electrolysis cell are described before the mathematical formulation of occuring crossover fluxes and experimental results are provided. The publication concludes with possible mitigation strategies that could be used for a reduction of gas crossover.

2 Publication overview

The following publications were submitted and published in »peer-reviewed« scientific journals and are an integral part of this doctoral thesis.

1. P. Haug, M. Koj, T. Turek, Influence of process conditions on gas purity in alkaline water electrolysis, *Int J Hydrogen Energ* **2017**, *42 (15)*, 9406-9418

   The actual impact factor of the International Journal of Hydrogen Energy is **3.582 (2016)**. It was the contribution of the first author to design and conduct the experiments and to prepare the manuscript. M. Koj assisted in the conception and execution of the experiments. T. Turek advised in the experiment conception and contributed to writing the manuscript. This publication is reprinted in chapter 3 and describes the influence of electrolyzer operating conditions, such as current density, electrolyte flow rate, temperature and process management, on the resulting gas purity. Furthermore, a dynamic process management strategy is proposed, which may enhance the overall operating regime of alkaline electrolyzers. Additionally, the experimental setup as well as the cell design is described in detail.

2. P. Haug, B. Kreitz, M. Koj, T. Turek, Process modelling of an alkaline water electrolyzer, *Int J Hydrogen Energ* **2017**, *42 (24)*, 15689-15707

   The actual impact factor of the International Journal of Hydrogen Energy is **3.582 (2016)**. It was the contribution of the first author to develop the mathematical model, to design and conduct the experiments as well as to prepare the manuscript. B. Kreitz contributed to the model development, carried out theoretical calculations and supported the manuscript preparation. M. Koj assisted in the conception of the experiments. T. Turek supported the model development and contributed to writing the manuscript. This publication is reprinted in chapter 4 and describes the modelling of the overall alkaline electrolysis process based on a classical process

engineering approach. Therefore, the electrolysis cell is depicted by two coupled continously stirred-tank reactors, while mass transport esimations are based on Reynolds and Sherwood correlations. The model is validated with experimental data and enlightens the most influencing process parameters on hydrogen crossover, which allows the deduction of optimization possibilities.

3. P. Trinke, P. Haug, J. Brauns, B. Bensmann, R. Hanke-Rauschenbach, T. Turek, Hydrogen crossover in PEM and alkaline water electrolysis: Mechanisms, direct comparison and mitigation strategies, *J Electrochem Soc* **2018**, *165 (7)*, F502-F513

   The actual impact factor of the Journal of the Electrochemical Society is **3.259 (2016)**. P. Trinke and P. Haug contributed equally to this work. It was the contribution of P. Trinke and P. Haug to design and conduct the electrolysis experiments as well as to prepare the manuscript. The work was divided in such way that the first author worked on PEM related topics, while P. Haug concentrated on alkaline electrolysis. Additional topics were prepared in cooperation. J. Brauns assisted in the conduction of the alkaline electrolysis experiments. B. Bensmann supported the conception of the experiments and the manuscript preparation. R. Hanke-Rauschenbach and T. Turek also assisted in writing the manuscript. This publication is reprinted in chapter 5 and firstly summarizes the crossover effects occuring in PEM and alkaline electrolysis. Consequently, the influence of current density, electrolysis pressure and process management on hydrogen crossover is investigated and compared between the two technologies. Finally, mitigation strategies are mentioned, which can be helpful for the reduction of gas crossover.

3 Influence of process conditions on gas purity in alkaline water electrolysis

P. Haug, M. Koj, T. Turek
Int J Hydrogen Energ **2017**, *42 (15)*, 9406-9418
https://doi.org/10.1016/j.ijhydene.2016.12.111

Abstract

In this paper the influence of operating conditions on the product gas purity of a zero-gap alkaline water electrolyzer was examined. Precise knowledge of the resulting gas purity is of special importance to prevent safety shutdown when the electrolyzer is dynamically operated using a renewable energy source. The investigation in this study involves variation of temperature, electrolyte concentration and flow rate as well as different electrolyte management concepts. The experiments were carried out in a fully automated lab-scale electrolyzer with a 150 cm^2 zero-gap cell and approximately 31 wt% KOH at ambient and balanced cathodic and anodic pressure. The purity of the evolved gases was measured via online gas chromatography. It can be seen from the experiments that a temperature increase and flow rate decrease reduces the gas impurity when mixing catholyte and anolyte. A further reduction of gas impurity can be achieved when both cycles are being separated and a dynamic cycling strategy is applied.

Keywords: alkaline water electrolysis, gas purity, process management, hydrogen production, gas solubility

3.1 Introduction

In 2002 the German government set the goal to reduce CO_2 emissions by 80 % until 2050 and to increase the contribution of renewable energy sources to the total electricity demand above 60 % [1, 2]. For the realization of this objective it is inevitable to establish energy storage devices to compensate the fluctuating nature of wind and solar energy [3–5]. Especially for long-term energy storage energy-rich hydrogen is commonly considered the most promising intermediate or final energy carrier [6–8]. Nowadays hydrogen, which is required in huge quantities for many important industrial processes such as ammonia synthesis, is still being produced through inexpensive, but greenhouse gas emitting processes like steam reforming and coal gasification [9–11]. Hydrogen production through electrolysis represents a share of only 4 % which already reveals that water electrolysis is still too costly because of its limited energy efficiency and large investments [12]. But within the framework of the power-to-gas concept, particularly water electrolysis is often discussed as the key technology for future synthesis of hydrogen because of its fast dynamic response to varying operating conditions [13]. Especially alkaline water electrolysis has been applied in the industry for decades but the dynamic behavior was of minor interest until first investigations came up in the 1990s [14, 15]. For realization and improvement of the power-to-gas-concept precise knowledge especially about the dynamic behavior of the electrolysis process is indispensable. During alkaline water electrolysis H_2O is reduced to H_2 and OH^- ions on the cathode, whereas OH^- is oxidized to form O_2 and H_2O on the anode. In total H_2O is split into H_2 and O_2. The following Equations (3.1) - (3.3) show the half cell and overall reactions with their corresponding electrode potentials against a standard hydrogen electrode (SHE) at 298.15 K and pH = 13.996 [16].

$$\text{Cathode: } 2\,H_2O + 2\,e^- \longrightarrow H_2 + 2\,OH^- \qquad E^0 = -0.8280\,V \tag{3.1}$$

$$\text{Anode: } 2\,OH^- \longrightarrow 0.5\,O_2 + H_2O + 2\,e^- \qquad E^0 = +0.4011\,V \tag{3.2}$$

$$\text{Overall reaction: } H_2O \longrightarrow H_2 + 0.5\,O_2 \qquad E^0 = -1.2291\,V \tag{3.3}$$

As can be seen from the overall reaction a minimum cell voltage of -1.2291 V, also referred to as reversible potential, is necessary for hydrogen production. In addition to this potential the overpotentials of the electrodes, the separator resistance and the bubble resistance have to be overcome as well [9]. Many workers are focusing on the improvement of the catalytic activity of electrode materials to reduce these overvoltages. A review of

promising electrode materials and further optimization strategies for zero-gap electrolyzers was published by Pletcher and Xiaohong [17]. Not only the cell voltage of an electrolyzer but also the purity of the gaseous products is of major interest as these limit the operation range of the plant. In literature the acceptable part-load operation of an industrial alkaline water electrolyzer is typically given with 10 % - 40 % of the nominal load [18–22]. Below this working range the oxygen quality is significantly reduced through contamination of hydrogen and vice versa. One source of this contamination is the diffusion of the product gases through the separator. This does not only decrease the gas quality, but also the overall electrical efficiency of the electrolyzer as oxygen can react back to water with hydrogen present at the cathode. The second source of contamination is the dissolution of gas in the electrolyte. After saturation with the corresponding gas, dissolved gas is able to outgas in the opposite gas separator as the anolyte and catholyte cycle are continuously mixed to compensate the difference in electrolyte concentration caused by the electrode reactions (cf. Equations (3.1) - (3.3)) [23, 24]. This operation mode may lead to safety issues as the lower (LEL) and upper explosion limits (UEL) of H_2/O_2 mixtures are given with 3.8 mol % and 95.4 mol % H_2 at atmospheric pressure and 80 °C [25]. Consequently industrial electrolyzers must be shut down as soon as a content of 2 vol% foreign gas is measured in the exhaust, which is about 50 % of LEL or UEL [26]. The contamination of the product gases is of special importance when the electrolyzer is operated at low current densities and therefore low gas production rates because the mentioned phenomena are mostly independent of the electrolyzer load [23]. An operation in the part-load region is conceivable when the electrolyzer is part of a power-to-gas plant and coupled with a renewable energy source. Hug et al. [14] reported that the daily operation of an alkaline electrolyzer powered with solar energy was mainly restricted by the oxygen purity at low global insolation and the resulting low current density. A possibility to reduce the anodic hydrogen content was mentioned by Grigoriev et al. [27] who proposed a Pt-catalyzed combustion of hydrogen and oxygen back to water by a gas recombiner. Another option was published by Schug [23] who proposed an optimized lye circulation control to keep the gas impurities low. Unfortunately only the qualitative description of this effect was described whereas the quantitative influence of the electrolyte flow rate on the gas purity was not published. Further work was done by Manabe et al. [28, 29] who measured the anodic hydrogen content at specific electrolyte temperatures and flow rates with different

separators.

In the present work the mechanisms and the extent of gas crossover are discussed first. Then the operating conditions of a lab-scale electrolyzer, such as current density, electrolyte flow rate, temperature, electrolyte concentration and process management are varied systematically and analyzed with regard to the resulting gas purity to derive optimum operating conditions. For this purpose a detailed study is performed so that the influence of each single parameter on the gas purity can be indicated. Furthermore the dynamic response of the gas purity during changing operating conditions is investigated.

3.2 Gas crossover

The gas crossover in alkaline water electrolysis is mainly caused by two phenomena – gas dissolution in the electrolyte and diffusion through the separator. In the following it is shown how either of these sources may be estimated quantitatively.

3.2.1 Gas solubility

In reaction engineering the solubility of gases in electrolyte solutions needs to be known for gas-liquid transfer estimations [30]. Unfortunately data for the solubility of hydrogen and oxygen in concentrated potassium hydroxide solution under electrolysis conditions is scarce. Most published papers only provide values for the solubility at room temperature or slightly above. Ruetschi and Amlie [31] measured the H_2 solubility in KOH at 30 °C for a concentration range from $0.0091\,\mathrm{mol\,L^{-1}}$ to $10.23\,\mathrm{mol\,L^{-1}}$, while Davis et al. [32] investigated the O_2 solubility and diffusivity in KOH for temperatures between 0 °C and 60 °C and concentrations of $0\,\mathrm{mol\,L^{-1}}$ - $12\,\mathrm{mol\,L^{-1}}$. Further data of oxygen solubility in several inorganic solutions was published by Tromans [33] and Narita et al. [34]. Only two publications were found which deal with the hydrogen or oxygen solubility under electrolysis conditions. Chatenet et al. [35] measured the oxygen solubility in sodium hydroxide and found that the Henry coefficient of O_2 in $11.1\,\mathrm{mol\,L^{-1}}$ NaOH (33 wt%) at 80 °C was reduced by a factor of 72 compared to an electrolyte of $1\,\mathrm{mol\,L^{-1}}$ NaOH at 25 °C. The other publication by Knaster and Apel'baum [36] provides values for the oxygen and hydrogen solubility in concentrated KOH at 21 °C, 45 °C and 75 °C.

To estimate the amounts of dissolved gases under electrolysis conditions we propose a method for calculation. It is well known that gas solubility mostly decreases with increasing salt concentration. This behavior can be described by applying the Setchenov relation (3.4), which is suitable for electrolyte concentrations of about $c_\mathrm{s} = 2\,\mathrm{mol\,L^{-1}}$ - $5\,\mathrm{mol\,L^{-1}}$. At even higher salt concentrations the gas solubility may be underestimated [30].

$$\log\left(c_{i,0}/c_{i,\mathrm{s}}\right) = K \cdot c_\mathrm{s} \tag{3.4}$$

The variables $c_{i,0}$, $c_{i,\mathrm{s}}$ and c_s describe the gas solubility in pure water, in the salt solution and the molar concentration of the salt solution, respectively. The parameter K is the so called Setchenov constant. It is specific to the dissolved gas and the salt and slightly dependent on temperature [37].

$$K = \sum\left(h_i + h_{\mathrm{G},i}\right) \cdot n_i \tag{3.5}$$

The parameter h_i is a salt specific constant, whereas $h_{\mathrm{G},i}$ takes into account the dissolved gas. Furthermore n_i denotes the index of the ion in the formula of the salt, which is simply multiplied with the sum of the salt- and gas specific constant. For K^+ and OH^- n_i is unity for both ions. The temperature dependence of the gas-specific constant $h_{\mathrm{G},i}$ is assumed to be a linear function of the temperature in the range from 273 K to 363 K [30].

$$h_{\mathrm{G},i} = h_{\mathrm{G},i,0} + h_{\mathrm{T},i} \cdot \left(T - 298.15\,\mathrm{K}\right) \tag{3.6}$$

The necessary parameter values for the calculation of O_2, H_2 and N_2 solubility in concentrated NaOH or KOH are given in Table 3.1.

Tab. 3.1: Model parameters from Ref. [30]. The $h_{\mathrm{T},i}$ value for H_2 and O_2 is valid from 273 K to 353 K, while the value for N_2 is valid from 278 K to 345 K.

Ion	h_i	Gas	$h_{\mathrm{G},i,0}$	$h_{\mathrm{T},i}$
	$\mathrm{m^3\,kmol^{-1}}$		$\mathrm{m^3\,kmol^{-1}}$	$\mathrm{m^3\,kmol^{-1}\,K^{-1}}$
Na^+	0.1143	H_2	−0.0218	−0.000299
K^+	0.0922	O_2	0	−0.000334
OH^-	0.0839	N_2	−0.0010	−0.000605

For calculation of the solubility in pure water $c_{i,0}$ the empirical relationship by Himmelblau [38] is proposed, which relates the Henry coefficient of the gases H_i (in atm) with

the temperature T (in K) of the solvent. Its validity is given in the temperature range from 273 K to 647 K.

$$A\left(\log \overline{H}_i\right)^2 + B\left(1/\overline{T}\right)^2 + C\left(\log \overline{H}_i\right)\left(1/\overline{T}\right) + D\left(\log \overline{H}_i\right) + E\left(1/\overline{T}\right) - 1 = 0 \tag{3.7}$$

This equation is only applicable if $\overline{H}_i$ is inserted as $\overline{H}_i = H_i \cdot 10^{-4}$ and $1/\overline{T} = 1/T \cdot 10^3$. The needed constants are given in Table 3.2.

Tab. 3.2: Model parameters taken from Ref. [38] for Henry coefficients of H_2, O_2 and N_2 in pure H_2O.

Gas	A	B	C	D	E
H_2	−0.1233	−0.1366	0.02155	−0.2368	0.8249
O_2	−0.0005943	−0.1470	−0.05120	−0.1076	0.8447
N_2	−0.1021	−0.1482	−0.01900	−0.03741	0.8510

The calculation of the gas solubility in pure water is then performed with the following equation which takes into account the solvent density ρ, the molar mass M and the partial pressure of the gas p_i above the solvent.

$$c_{i,0} = \frac{\rho}{M} \cdot \frac{p_i}{101325\,\mathrm{Pa} \cdot H_i} \tag{3.8}$$

The usually applied electrolyte in alkaline water electrolysis is a 30 wt% KOH [39] solution, which corresponds to a molar concentration of about 6.9 mol L^{-1} [40]. If a typical electrolysis temperature of about 80 °C and atmospheric pressure $p_{abs} = p_{H_2} = 101325$ Pa is assumed Equations (3.4) and (3.8) provide a H_2 concentration of $c_{H_2,0} = 0.753\,\mathrm{mol\,m^{-3}}$ in pure water and $c_{H_2,KOH} = 0.155\,\mathrm{mol\,m^{-3}}$ in 6.9 mol L^{-1} KOH, respectively. A comparison of this value with the data by Knaster and Apel'baum [36], who measured a concentration of $c_{H_2,KOH} = 0.088\,\mathrm{mol\,m^{-3}}$ at a KOH mass fraction of 30.2 wt% and a temperature of 75 °C, shows that the saturation concentration is overestimated by almost 80 % using the presented method. Another comparison of the calculated oxygen solubility in 11.1 mol L^{-1} NaOH at 80 °C and a partial pressure of $p_{O_2} = 79500$ Pa shows good agreement with the data measured by Chatenet et al. [35]. Thus, an O_2 concentration of $c_{O_2,NaOH} = 0.0098\,\mathrm{mol\,m^{-3}}$ is obtained, while Chatenet et al. measured $c_{O_2,NaOH} = 0.0093\,\mathrm{mol\,m^{-3}}$, which is equal to an overestimation of only 5 %.

Fig. 3.1 shows a comparison of measured and modelled gas solubilities as a function of the potassium hydroxide concentration. It can be seen that the calculated solubilities for hydrogen and oxygen show satisfying agreement with the measured values from Ruetschi and Amlie [31] and Davis et al. [32] over the whole lye concentration range from 0 mol L^{-1} to 12 mol L^{-1}. The modelled temperature dependence of the saturation concentration is further compared with the data of Knaster and Apel'baum [36] in Fig. 3.2. As already mentioned the hydrogen concentration is overestimated by the model and reveals a solubility increase with growing temperature although a decreasing saturation concentration was measured. The oxygen concentration is underestimated in the low temperature region but can be predicted with good accuracy, especially at higher temperature. The modelling results of Tromans [33] are also shown in Fig. 3.2 for comparison. A major advantage of Tromans' model is that a similar trend like the measuring data of Knaster and Apel'baum is predicted, although the oxygen concentration is overestimated in the whole investigated temperature range.

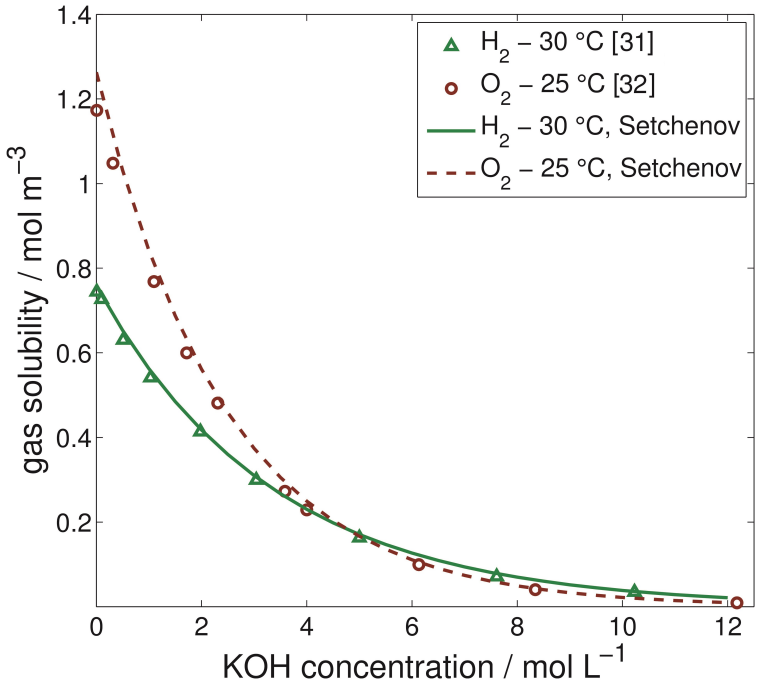

Fig. 3.1: Comparison of measured and modelled hydrogen and oxygen solubility as a function of the KOH concentration at a gas partial pressure of 101325 Pa.

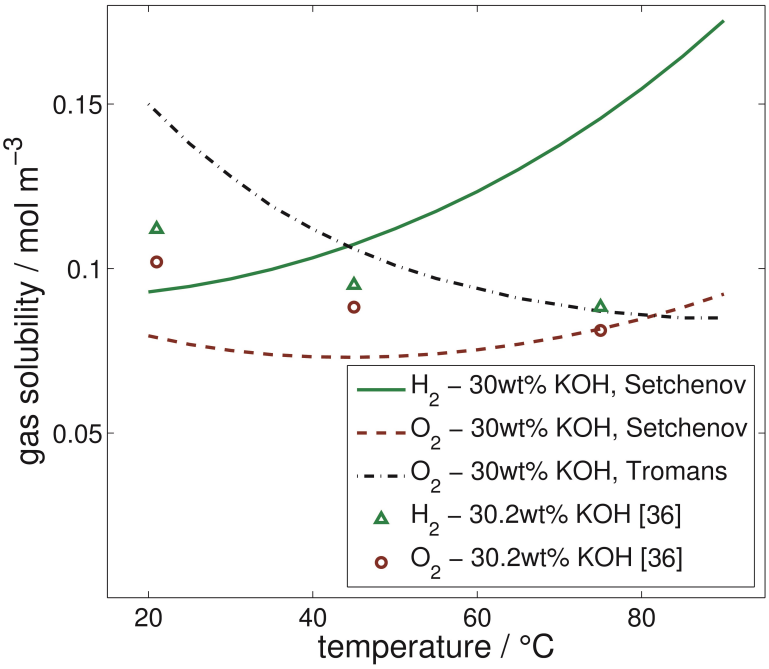

Fig. 3.2: Comparison of measured and modelled hydrogen and oxygen solubility in 6.9 mol L^{-1} KOH as a function of temperature at a gas partial pressure of 101325 Pa.

3.2.2 Crossover through the separator

The separator in an electrochemical cell has two main functions. It is necessary to prevent any short circuits between the electrodes and to avoid the mixing of hydrogen and oxygen. Therefore the separator needs to be stable in the highly alkaline conditions of an alkaline electrolyzer. Furthermore the separator should be very conductive for the transport of OH^- ions between anode and cathode, so that low voltage drops are caused. The conductivity of a separator depends on its porosity and tortuosity as the current passes through the liquid electrolyte present in the pores [21]. The gases dissolved in the electrolyte can diffuse through the pores of the separator and contaminate the evolved gas of the opposite half cell. A small reduction of the diffusion through the separator can be achieved by higher electrolyte flow rates, which increase the nucleation growth rate of the gas bubbles [41, 42]. It has been discussed extensively in the literature that the electrolyte is supersaturated with either oxygen or hydrogen in the vicinity of the electrode [43–48]. In case of a zero-gap cell setup this supersaturation should be responsible for the concentration gradient for gas diffusion across the separator. The gas crossover through the

separator is commonly described using Fick's law (3.9), especially in PEM (proton exchange membrane or polymer electrolyte membrane) electrolysis modelling [26, 49–52] and can be applied for alkaline water electrolysis as well.

$$J_{i,\mathrm{cross}} = \frac{D_{i,j,\mathrm{eff}}}{d_{\mathrm{Sep}}} \cdot \left(c_i^{\mathrm{cat}} - c_i^{\mathrm{ano}}\right) \tag{3.9}$$

If the assumption is made that only dissolved gas can crossover and no pressure gradient is present, $J_{i,\mathrm{cross}}$ describes the overall molar flux density through the separator. In Equation (3.9) c_i denotes the cathodic and anodic concentration of dissolved gas i, whereas d_{Sep} is the separator thickness and $D_{i,j,\mathrm{eff}}$ the effective gas diffusion coefficient in the separator. As the separator is filled with electrolyte the diffusion coefficients $D_{i,j}$ of the gases in the lye need to be known for the calculation of the effective diffusion coefficient. Tham et al. [53] summarized the data of other authors and measured the diffusion coefficients of hydrogen and oxygen in aqueous potassium hydroxide for a concentration range of $0\,\mathrm{mol\,L^{-1}}$ - $14\,\mathrm{mol\,L^{-1}}$ and temperatures between 25 °C and 100 °C. Some of the published data is shown in Table 3.3.

Tab. 3.3: Diffusion coefficients of hydrogen and oxygen in $6.9\,\mathrm{mol\,L^{-1}}$ KOH solution for various temperatures taken from Ref. [53].

ϑ	$D_{\mathrm{H_2,KOH}}$	$D_{\mathrm{O_2,KOH}}$
°C	$\mathrm{m^2\,s^{-1}}$	$\mathrm{m^2\,s^{-1}}$
40	$2.434 \cdot 10^{-9}$	$0.793 \cdot 10^{-9}$
60	$3.679 \cdot 10^{-9}$	$1.172 \cdot 10^{-9}$
80	$5.630 \cdot 10^{-9}$	$1.807 \cdot 10^{-9}$
100	$8.380 \cdot 10^{-9}$	$2.783 \cdot 10^{-9}$

These diffusion coefficients make it possible to estimate the effective diffusion coefficient in the separator in analogy to the diffusion in porous media or membranes. The formula is commonly given as [54, 55]:

$$D_{i,j,\mathrm{eff}} = \frac{\varepsilon \cdot D_{i,j}}{\tau} \tag{3.10}$$

Here, ε and τ describe the separator porosity and tortuosity, respectively. As an example Zirfon$^{\mathrm{TM}}$ Perl UTP 500 is a commercially available separator by AGFA for alkaline water electrolysis with a thickness of $d_{\mathrm{Sep}} = (500 \pm 50)$ µm and a porosity of $\varepsilon = 0.5 \pm 0.1$ [56].

No data for the tortuosity of the separator is available in the literature, but typical values for porous separators in electrochemical cells are in the range from $\tau \approx 2$ - 7 [57]. Since Zirfon^{TM} is reported to be impermeable for gases [52] the previously made assumption that only dissolved gas is able to crossover is applicable.

3.3 Experimental setup

The flowsheet with main components and measuring instruments of the lab-scale electrolyzer is shown in Fig. 3.3 and described in detail in the following. The plant is filled with about 31 wt% potassium hydroxide electrolyte solution, which is continuously being pumped through the cell and gas separators and recycled back to the mixing point to compensate the concentration difference caused by the electrode reactions with two membrane pumps (P-1, P-2; max. $30\,\mathrm{L\,h^{-1}}$; Prominent ALPc 0230). The volumetric flow rate of the electrolyte is measured at the cell inlet with oval gear meters (I-3, I-4; $0\,\mathrm{L\,min^{-1}}$ - $1\,\mathrm{L\,min^{-1}}$, Bopp & Reuther OR015). Pumping of the electrolyte is necessary to avoid gas accumulation within the electrolysis cell and to keep the temperature increase between cell inlet and outlet due to overvoltages and ohmic losses below a certain level. The temperature of the electrolyte is measured and controlled by two heated tubes (I-1, I-2) at the cell inlet and additionally measured at the outlet (I-5, I-6) again. According to Equations (3.1) and (3.2) hydrogen is evolved at the cathode and oxygen production takes place at the anode. The electrodes used are a catalyst-coated nickel-mesh cathode and a bare nickel-mesh anode with a wire thickness of 150 mm, a mesh size of 470 mm and a geometrical area of $150\,\mathrm{cm^2}$. As a separator Zirfon^{TM} Perl UTP 500 by AGFA is used. The electrodes are pressed onto the separator directly, so that a zero-gap cell setup is achieved. The cell is supplied by a DC power supply with a maximum of 8 V and 180 A (TDK-Lambda GENH8-90), which corresponds to a maximum current density of $12\,\mathrm{kA\,m^{-2}}$. The geometrical dimensions of the half cells amount to $(0.16 \times 0.015 \times 0.145)$ m^3 (height $\times$ width $\times$ depth) each, which corresponds to an overall cell volume of approximately 0.7 L. The evolved gases leave the cell with the pumped electrolyte and enter the gas separators downstream, where they are separated from the electrolyte. While the electrolyte is cycled back to the cell inlet again, the gases rise up into the corresponding gas washing bottles. These bottles are used to remove potassium

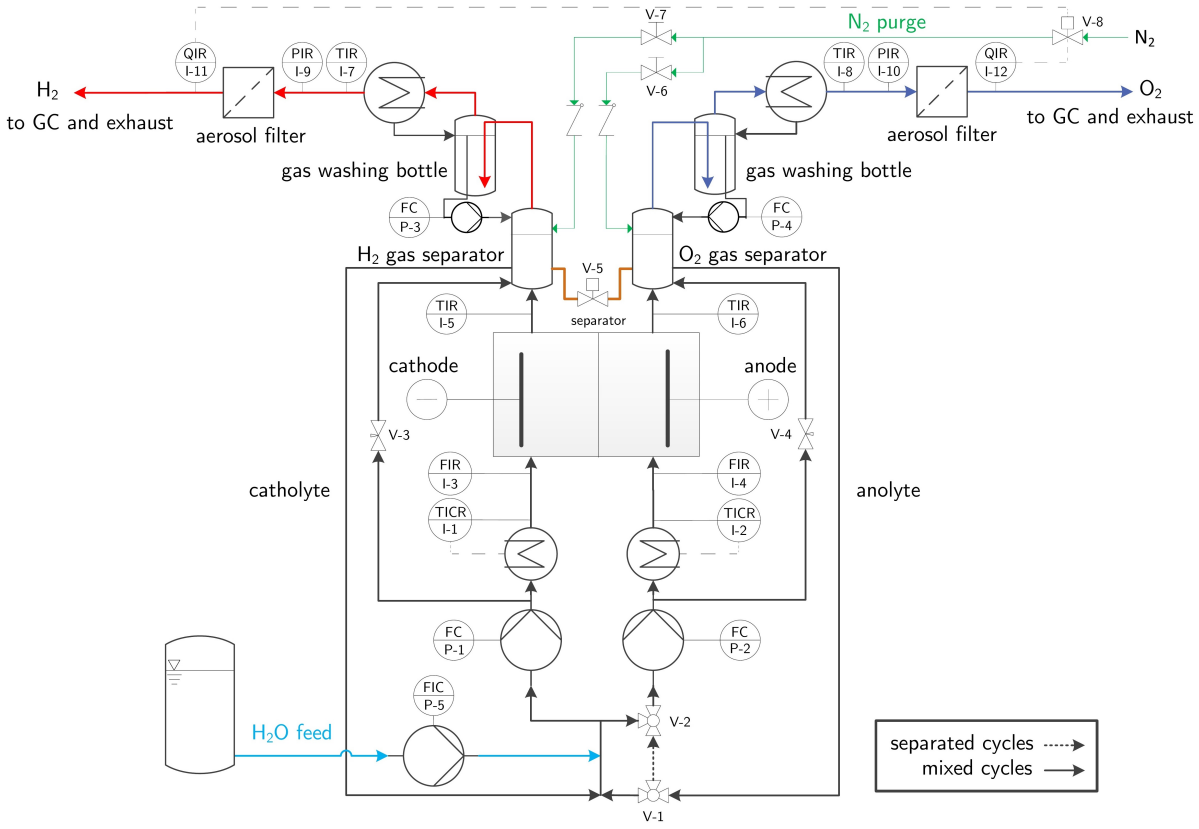

Fig. 3.3: Flowsheet of lab-scale electrolyzer.

hydroxide aerosol by dispersing the hydrogen and oxygen stream in distilled water. As the evolved gases take water vapor with them some water is removed from the plant which would cause an increase of the electrolyte concentration. Part of the transported water condenses in the gas washing bottles and leads to a liquid level rise. After leaving the washing bottles the gases enter reflux condensers, where most of the remaining gaseous water is condensed and fed back to the washing bottles. As soon as the liquid level reaches the height of a rising pipe within the washing bottles a peristaltic pump (P-3, P-4) recycles the water back into the plant. The water consumed by electrolysis is continuously refilled by a membrane pump (P-5, Fink Chem+Tec Ritmo®05/3) according to Faraday's law. In such way the electrolyte concentration can be kept approximately constant, which was continuously checked through titration using a Metrohm 794 Basic Titrino during the experiments. Remaining traces of potassium hydroxide aerosol and water are filtered from the gas flows by aerosol filters (10 µm pore size, polypropylen, Infiltec) before the oxygen content in hydrogen and vice versa is analyzed by electrochemical on-line sensors (I-11, I-12; 0 vol% - 2 vol%, Siegrist MECCOS eTr) qualitatively. These

sensors are installed for safety reasons only and enable the nitrogen purge by opening the solenoid valves (V-6, V-7, V-8) as soon as the safety limit of 2 vol% of foreign gas is exceeded. This corresponds to 50 % of the lower explosion limit of H_2 in O_2 and vice versa [24]. For quantitative determination of gas crossover the gas streams are analyzed in an on-line gas chromatograph (Agilent 7820A) afterwards, which is equipped with two HP Molesieve Columns for permanent gas separation and parallel measurement of anodic and cathodic gas flows. The gas chromatograph was calibrated with different test gas mixtures of H_2, O_2 and N_2. This calibration was checked with one of these gas mixtures daily to guarantee exact measurements. The used GC method is shown in Table 3.4.

Tab. 3.4: GC method for quantification of foreign gas in anodic and cathodic gas flows.

Carrier gas	Argon 5.0
Sample loop	250 µL
Valve temperature	60 °C
Inlet temperature	60 °C
Oven temperature	30 °C, isothermal
Detector temperature	150 °C, TCD
Column flow	12.6 mL min^{-1}
Septum flow	1.1 mL min^{-1}
Reference flow	20.0 mL min^{-1}
Makeup flow	0.5 mL min^{-1}

Besides the classical electrolyzer operation with mixed electrolyte cycles it is possible to separate anolyte and catholyte completely by changing the valve position of the 3/2-way valves (V-1, V-2) and closing valve (V-5) between the hydrogen and oxygen gas separators. This valve is usually opened when operating with mixed cycles to keep the electrolyte level in the separators equal. The separated operation mode makes it possible to characterize gas crossover through different membrane or separator materials directly as gas dissolution in the electrolyte does not affect the product gas quality in this way. Nevertheless it has to be kept in mind that the gas diffusion coefficient through the separator is not measured directly by analyzing the product gas impurity as evolved gas may be reduced or oxidized on the counter electrode. Furthermore it is possible to operate the plant partly separated where the 3/2-way valves (V-1, V-2) are in the position of separated cycles, whereas valve

(V-5) stays opened like in the classical mixed electrolyzer operation. This operation mode prevents gas crossover through mixing of the electrolyte cycles while maintaining liquid level equalization in the gas separators. Thus it is conceivable that gas may not only crossover through the separator but also through the equalization tube using this cycling strategy.

3.4 Results and discussion

In this section the influence of the electrolyte flow rate, temperature, concentration and process management on the resulting gas purity is shown. For all these parameters stationary data was measured with a gas chromatograph at the exhaust of the plant. Stationary data was achieved in such way that a specific current density was applied to the cell and chromatograms were recorded simultaneously. The current density was kept constant until the gas concentration did not change for at least 30 min before it was ramped down to the next operating point.

Fig. 3.4 shows the applied current density and measured anodic hydrogen concentration as a function of time for an average electrolyte flow rate of $\dot{V}_\mathrm{L} = 0.33\,\mathrm{L\,min^{-1}}$, a temperature of 80 °C, an electrolyte concentration of 31.2 wt% and mixed cycles exemplarily. It can be seen that the necessary time to reach a stationary operating point increases significantly with decreasing current density as the volumetric gas flow rate shrinks. The time to achieve stationary data is mainly affected by the gas volume of the plant, which is estimated to be about 1.6 L on each side. The electrolyte volume amounts to approximately 1.9 L whereby most of the volume is taken from the cell with about 0.7 L and the gas separators with 1.2 L. Furthermore it can be seen that the anodic hydrogen content increases with lower applied current density as it is expected. The lowest investigated current density was $0.5\,\mathrm{kA\,m^{-2}}$ as a further decrease would have led to a safety shutdown of the plant.

Fig. 3.5 shows the foreign gas concentration of the anodic and cathodic product gases for different current densities. The O_2 in H_2 content is always less compared to the impurity of the anodic product gas stream. At a current density of $0.5\,\mathrm{kA\,m^{-2}}$ only 0.290 vol% O_2 in H_2 is measured whereas H_2 in O_2 amounts to 1.090 vol%. This is mainly caused by the higher production rate of hydrogen, which is evolved in amolar ratio of 2:1 compared to

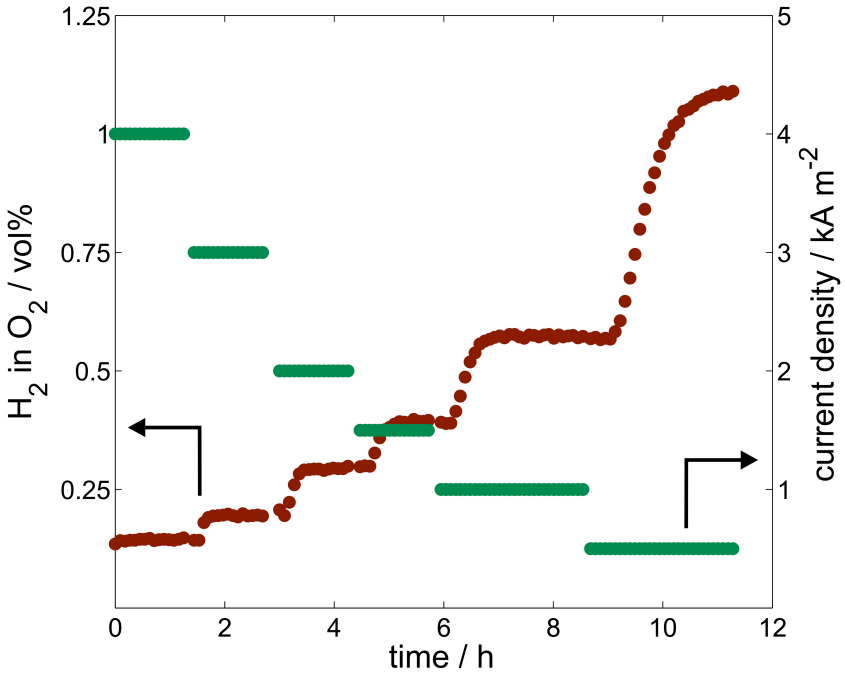

Fig. 3.4: Anodic hydrogen content as a function of current density and time. Operating conditions: mean $\dot{V}_\mathrm{L} = 0.33\,\mathrm{L\,min^{-1}}$, $T = 80\,^\circ\mathrm{C}$, $c_\mathrm{KOH} = 31.2\,\mathrm{wt\%}$, mixed electrolyte cycles.

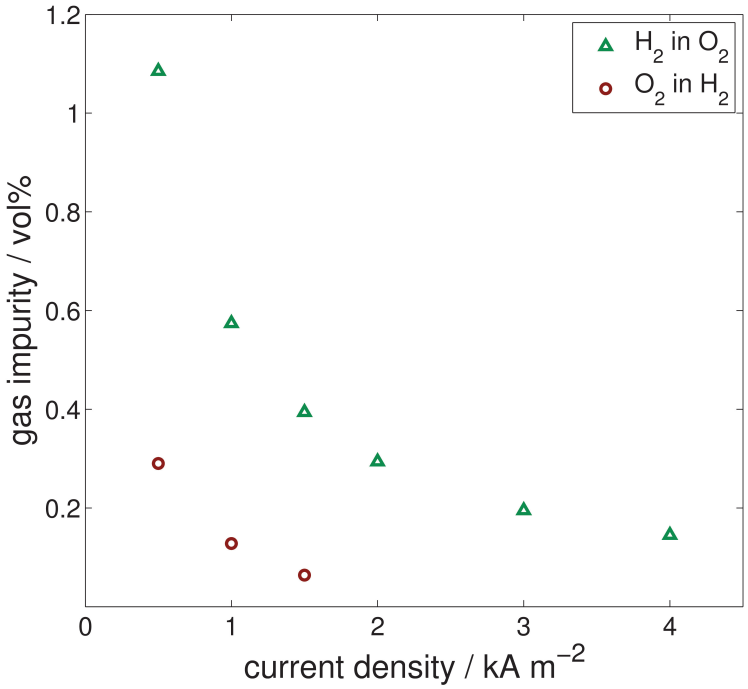

Fig. 3.5: Measuring data of anodic and cathodic foreign gas content as a function of current density. Operating conditions: mean $\dot{V}_\mathrm{L} = 0.33\,\mathrm{L\,min^{-1}}$, $T = 80\,^\circ\mathrm{C}$, $c_\mathrm{KOH} = 31.2\,\mathrm{wt\%}$, mixed electrolyte cycles.

oxygen. Furthermore it was shown that the oxygen solubility and diffusion coefficient in concentrated KOH at operating conditions are smaller too.

As this behavior was identical in all conducted experiments, only the H_2 in O_2 content is discussed in the following.

3.4.1 Flow rate

The flow rate of the electrolyte can be adjusted manually with a switch in 20 % steps directly on the pumps. For this investigation three different electrolyte flow rates, namely 20 %, 40 % and 100 % of the pump rate were chosen, whereas always the same pump rate was fed to the anodic and cathodic chamber. However, different effective flow rates in both cycles resulted, which are shown in Tab. 3.5. Therefore in the further discussion it will be referred to the percentage setting of the pumps.

Tab. 3.5: Effective cathodic and anodic volumetric flow rate with average flow rate and corresponding pump rate setting at a temperature of 80 °C and a KOH concentration of 31.7 wt%.

Pump rate	$\dot{V}_{\mathrm{L,cat}}$	$\dot{V}_{\mathrm{L,ano}}$	$\dot{V}_{\mathrm{L,mean}}$
%	$\mathrm{L\,min^{-1}}$	$\mathrm{L\,min^{-1}}$	$\mathrm{L\,min^{-1}}$
20	0.205	0.185	0.195
40	0.375	0.285	0.330
100	0.452	0.470	0.461

The results of the experiments conducted at a temperature of 80 °C, a KOH concentration of 31.7 wt% and mixed electrolyte cycles are shown in Fig. 3.6. It can be clearly seen that an increase of the electrolyte flow rate led to a decrease of the product gas quality. Especially in the part-load region of $0.5\,\mathrm{kA\,m^{-2}}$, where an anodic hydrogen concentration of 1.636 vol% was measured at the highest flow rate of $\dot{V}_{\mathrm{L}} = 100\,\%$ a reduction down to 0.701 vol% could be achieved by simply decreasing the electrolyte flow rate to $\dot{V}_{\mathrm{L}} = 20\,\%$. This effect can be attributed to the higher amount of dissolved gas which is transferred back to the cell from the gas separators at higher electrolyte flow rates. The mixing of the electrolyte cycles causes a higher feed of dissolved foreign gas to the gas separators as well then. At a current density of $4.0\,\mathrm{kA\,m^{-2}}$ the effect becomes less important because

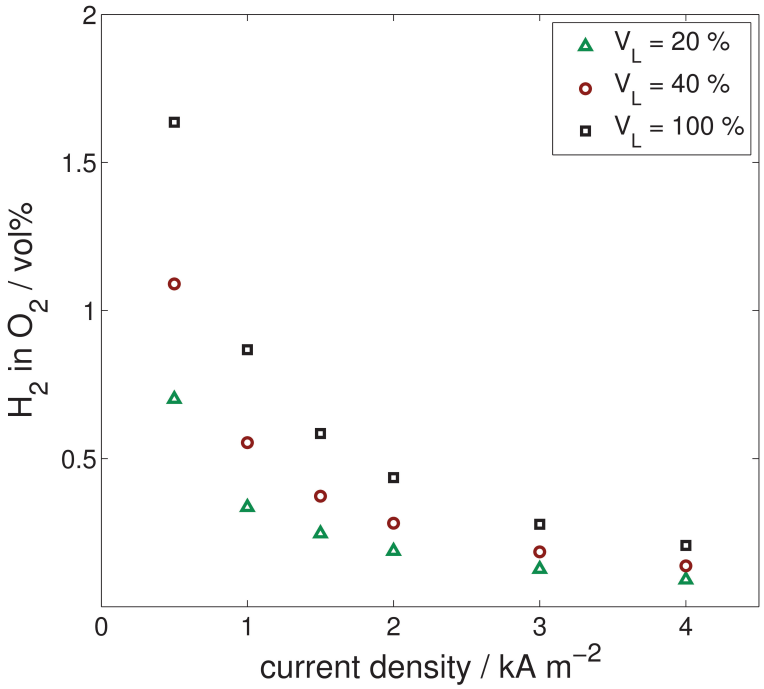

Fig. 3.6: Anodic hydrogen content as a function of current density and electrolyte flow rate. Operating conditions: $T = 80\,°\mathrm{C}$, $c_{\mathrm{KOH}} = 31.7\,\mathrm{wt\%}$, mixed electrolyte cycles.

the produced gas flow is large compared to the outgassing flow from the electrolyte. In literature, however, the crossover through the separator is reported to reduce with an increasing bubble growth rate [41], which can be enhanced through higher electrolyte flow rates. Nevertheless, this effect is negligible in the present experimental setup as the electrolyte flow velocities in the electrolysis cell only vary in the range from $1.4\,\mathrm{mm\,s^{-1}}$ to $3.6\,\mathrm{mm\,s^{-1}}$. Therefore a minimum electrolyte flow rate should be chosen to keep the impurities through anolyte and catholyte mixing small. It must be ensured though that the electrolyte flow rate is high enough to keep the temperature increase within the cell at an acceptable level. Furthermore it should be noted that a decrease of the electrolyte flow rate may lead to an increase of the electrode bubble coverage which causes a cell voltage increase [42]. But this is strongly dependent on the actual cell design so that no general statement can be made. The measurements within this experiment showed a cell voltage increase of $20\,\mathrm{mV}$ at a current density of $4.0\,\mathrm{kA\,m^{-2}}$ from the lowest to highest flow rate, but this may be attributed to an aging effect of the electrodes as well. Thus the lowest possible electrolyte flow rate may not be preferable in terms of Faraday efficiency. However, next to the already mentioned safety reasons a higher gas impurity also causes

a loss of hydrogen which is vented with the evolved oxygen. Furthermore the oxygen in the cathodic hydrogen flow is removed by catalytic deoxygenation and dried afterwards in adsorption columns which causes an additional hydrogen loss of 3 % - 8 % as dried hydrogen is required for regeneration of the columns [58].

3.4.2 Electrolyte concentration

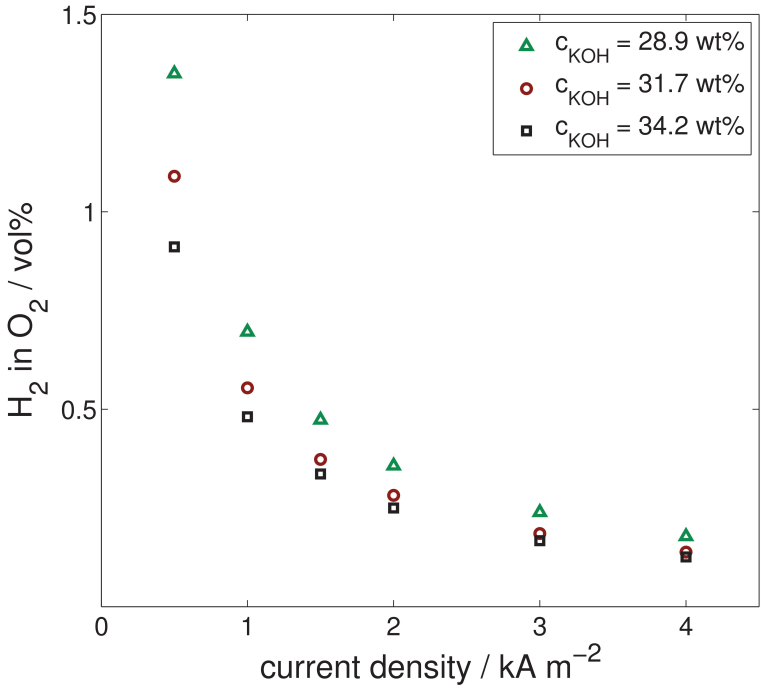

Fig. 3.7: Anodic hydrogen content as a function of current density and electrolyte concentration. Operating conditions: $\dot{V}_L = 40\,\%$, $T = 80\,°C$, mixed electrolyte cycles.

For the measurements of the influence of electrolyte concentration three different KOH concentrations were applied. All experiments were conducted with mixed cycles, a temperature of 80 °C and a flow rate of $\dot{V}_L = 40\,\%$. Fig. 3.7 shows that the gas impurity is decreasing with increasing electrolyte concentration, especially in the low current density region. Thus the H_2 in O2 content is reduced from 1.350 vol% at 28.9 wt% KOH and 0.5 kA m^{-2} to 0.911 vol% at 34.2 wt%. This behavior can be explained using the salting-out effect, which predicts a decreasing gas solubility with increasing salt concentration. Furthermore the diffusion coefficients of H_2 and O_2 are reported to decrease as well [53]. However, it has to be considered that the maximum KOH conductivity of 1393 mS cm^{-1}

at 80 °C is achieved with 32.5 wt% KOH, which corresponds to a molar concentration of 7.5 mol L^{-1} [40]. Therefore an increase of the electrolyte concentration above 32.5 wt% leads to a decrease of the Faraday efficiency.

3.4.3 Temperature

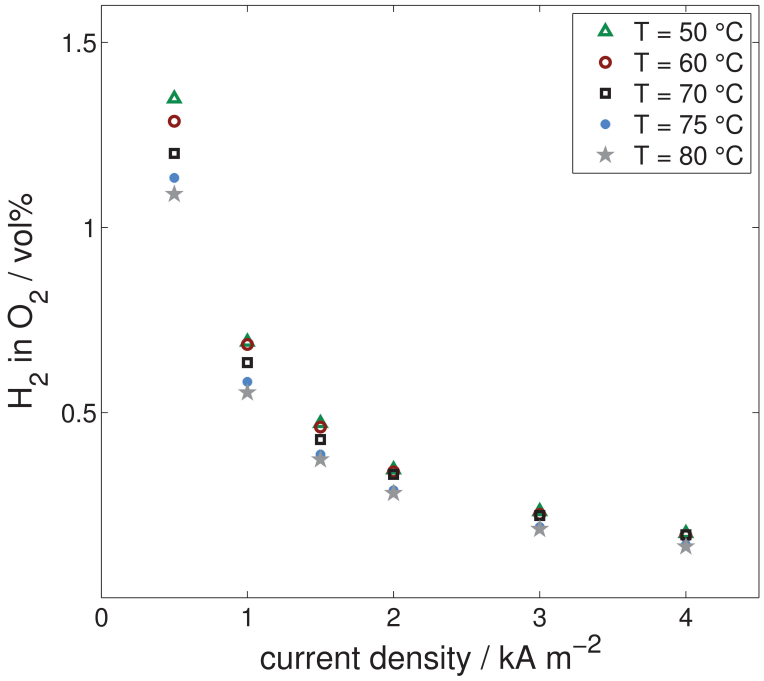

Fig. 3.8: Anodic hydrogen content as a function of current density and electrolyte temperature. Operating conditions: $\dot{V}_L = 40\,\%$, $c_{KOH} = 31.0\,wt\%$, mixed electrolyte cycles.

The investigation of the temperature impact on the gas purity was carried out at an electrolyte flow rate of $\dot{V}_L = 40\,\%$, a KOH concentration of 31.0 wt% and mixed electrolyte cycles. As shown in Fig. 3.8 the gas purity improves with higher electrolyte temperature, but the influence of the electrolyte temperature is not as strong as of the liquid flow rate in the investigated temperature range. At a current density of 0.5 kA m^{-2} a value of 1.090 vol% at 80 °C was measured while a higher value of 1.348 vol% occurred at a temperature of 50 °C. This behavior matches the solubility data from Knaster and Apel'baum [36] who measured a decreasing gas saturation concentration with increasing temperature. Similar to the effect of the electrolyte flow rate, the temperature impact on gas purity levels out at higher current density. Another reason for an increase of the gas

impurity at lower temperatures could be the increase of the electrolyte viscosity, which has a value of 0.88 mPa s at 80 °C and 1.4 mPa s at 50 °C. This slows down the bubble rise velocity in the separators and might result in gas bubbles being sucked back and fed to the cell again.

3.4.4 Process management

With the aim of gas impurity reduction several process management concepts are investigated in the following. This includes the investigation of various electrolyte cycling possibilities such as mixed, separated and partly separated electrolyzer operation. The obtained results are shown in Fig. 3.9. A comparison between the mixed and separated mode reveals that the gas purity is predominantly affected through mixing of the gas saturated electrolyte cycles. Thus the H_2 in O_2 content is reduced from 1.090 vol% to only 0.146 vol% when the plant is operated with a flow rate of $\dot{V}_L = 40\,\%$, a temperature of 80 °C and 31.7 wt% KOH. However, the liquid level and electrolyte concentration in the anodic and cathodic cycle changes with time according to the half cell reactions. Therefore it is not possible to keep the cycles separated over prolonged times as the concentration needs to be equalized to ensure stable cell performance. In addition the plant was operated partly separated, so that electrolyte level and pressure equalization through the equalization tube between the gas separators is possible. As also shown in Fig. 3.9 no significant difference in the gas purity between the partly separated and separated operation modes could be measured. Thus it can be assumed that gas crossover in partly separated operation also occurs only due to crossover through the separator.

It was then investigated how the crossover through the separator is influenced by the electrolyte temperature and concentration. For this purpose the electrolyte cycles were partly separated to keep the pressure in the separators equal. The results are shown in Fig. 3.10 (left) for various electrolyte concentrations at a current density of 0.5 kA m^{-2}. The gas impurity in this operation mode increases with growing temperature within the measured range. This further emphasizes that gas purity in alkaline water electrolysis is mainly affected by gas dissolution in the electrolyte as it was shown before (cf. Fig. 3.8) that gas impurity increases with decreasing temperature although the crossover shrinks. With the assumptions that no hydrogen oxidation takes place at the anode and no oxygen is present in the cathodic exhaust the flux density through the separator can be calculated

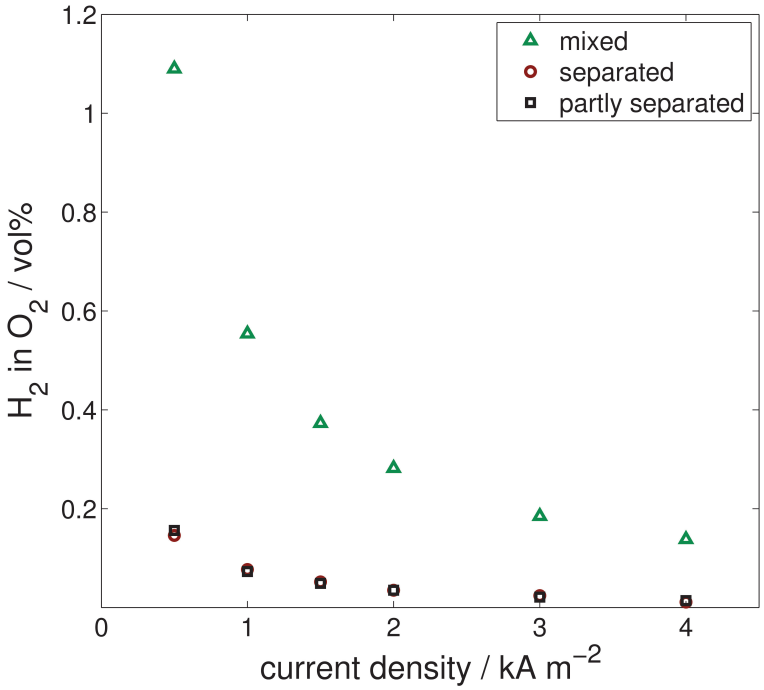

Fig. 3.9: Anodic hydrogen content as a function of current density and electrolyte management. Operating conditions: $\dot{V}_\mathrm{L} = 40\,\%$, $T = 80\,°\mathrm{C}$, $c_\mathrm{KOH} = 31.7\,\mathrm{wt}\%$.

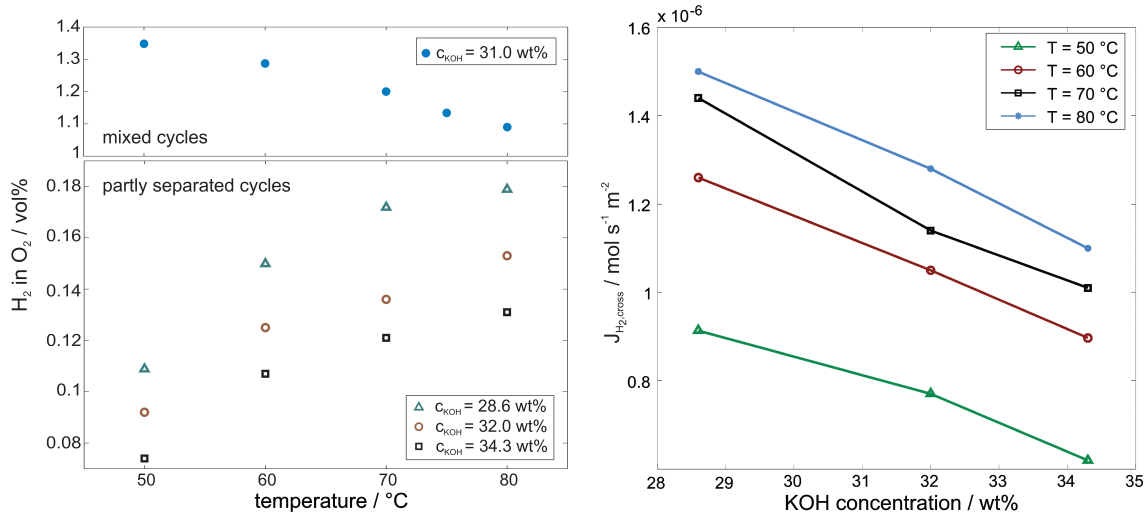

Fig. 3.10: (left) Comparison of anodic hydrogen content at mixed and partly separated cycles as a function of temperature and concentration. (right) Hydrogen flux density through the separator as a function of KOH concentration and temperature. Operating conditions: $j = 0.5\,\mathrm{kA\,m^{-2}}$, $\dot{V}_\mathrm{L} = 40\,\%$.

as follows:

$$J_{\mathrm{H_2,cross}} = \frac{I}{4 \cdot F \cdot \left(\frac{1}{x_{\mathrm{H_2,ano}}} - 1\right) \cdot A_{\mathrm{Sep}}} \tag{3.11}$$

At an electrolyte concentration of 32.0 wt%, a temperature of 80 °C and a Zirfon$^{\mathrm{TM}}$ separator with a geometrical area of $A_{\mathrm{Sep}} = 232\,\mathrm{cm^2}$ a value of $J_{\mathrm{H_2,cross}} = 1.28 \cdot 10^{-6}\,\mathrm{mol\,s^{-1}\,m^{-2}}$ is obtained, which is equal to only 0.08 % of the total hydrogen production at $0.5\,\mathrm{kA\,m^{-2}}$. At mixed cycles this value should be even smaller as the concentration gradient over the separator is lower in this case. If it is further assumed that only dissolved gas is able to diffuse through the separator with a thickness of 500 µm, no pressure gradient is present and the hydrogen concentration in the cathodic chamber equals the saturation concentration of approximately $0.088\,\mathrm{mol\,m^{-3}}$, whereas the anodic hydrogen concentration is zero, the effective diffusion coefficient is estimated to be $D_{\mathrm{H_2,Sep,eff}} = 7.29 \cdot 10^{-9}\,\mathrm{m^2\,s^{-1}}$. However this value is higher than the molecular diffusion coefficient of hydrogen $D_{\mathrm{H_2,KOH}} = 5.35 \cdot 10^{-9}\,\mathrm{m^2\,s^{-1}}$ in 32.0 wt% KOH [53] and therefore impossible. This result is assumed to be caused by supersaturation of the electrolyte. If we assume a tortuosity of $\tau = 2$ in Equation (3.10) an effective diffusion coefficient of $D_{\mathrm{H_2,Sep,eff}} = 1.34 \cdot 10^{-9}\,\mathrm{m^2\,s^{-1}}$ and therefore a supersaturation of 5.4 times the saturation concentration is obtained. In the literature [59] values ranging from 15 to 165 times the saturation concentration in the vicinity of the electrode can be found for various temperatures, electrolytes and electrode materials. For the reason of comparison the hydrogen flux densities through the separator were calculated for all measured data points. The results are shown on the right side of Fig. 3.10 and reveal a linear trend of the hydrogen flux density through the separator within the investigated electrolyte concentration range at a given temperature.

As a result from the previous investigations a dynamic electrolyte cycling strategy is proposed which separates the cycles at low current density and switches to mixing at a given higher current density. Using this method the operation range of an alkaline water electrolyzer could be enhanced. Another improvement of the gas purity can be achieved when the process is mixed and partly separated continuously. This dynamic switching of the electrolyte cycles is shown in Fig. 3.11 where electrolysis was performed at a constant current density of $1.0\,\mathrm{kA\,m^{-2}}$. Before the start of the experiment the cycles were mixed at a temperature of 80 °C and a KOH concentration of 32.0 wt% until a stationary anodic hydrogen content of 0.564 vol% was measured. After about 30 min the cycles were partly

separated and mixed again after another 30 min. The valve switching points are shown in red in Fig. 3.11, whereas the first line indicates the time of separation and the second line the time of mixing the electrolyte cycles. This procedure was repeated three times.

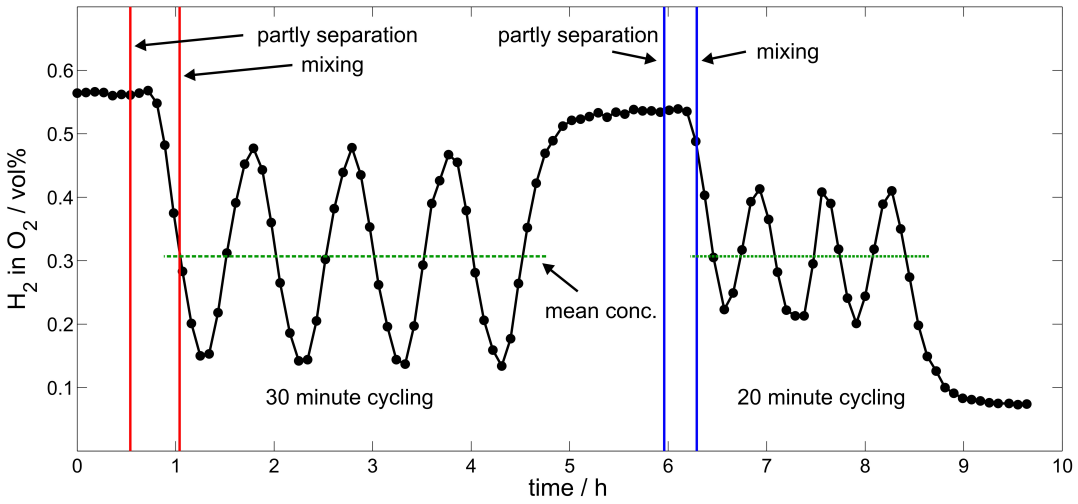

Fig. 3.11: Anodic hydrogen content as a function of time achieved by continous switching between mixed and partly separated operation mode. Operating conditions: $j = 1.0\,\mathrm{kA\,m^{-2}}$, $\dot{V}_\mathrm{L} = 40\,\%$, $T = 80\,^\circ\mathrm{C}$, $c_\mathrm{KOH} = 32.0\,\mathrm{wt\%}$.

As can be seen from Fig. 3.11 a dynamic response of the gas purity is measured. The resulting purity oscillates between the stationary points of mixed (0.564 vol%) and partly separated (0.073 vol%) mode with a period duration of 1 h and a mean value of 0.306 vol%, which is indicated by the green dotted line. The lowest obtained H_2 in O_2 value was 0.132 vol%, whereas the maximum amounts to 0.478 vol%. This dynamic switching has the advantage of approximately constant electrolyte concentration and lower gas impurity. After measuring stationary data at mixed electrolyte cycles again the experiment was repeated with faster switching intervals of 20 min, which is indicated by the blue lines in Fig. 3.11. Again, this switching interval was repeated three times. It is obvious that the amplitude (min: 0.201 vol%, max: 0.413 vol%) becomes smaller and the period duration reduces to 40 min, but the mean value remained exactly on the same level with 0.306 vol%. The experiment was finished as soon as stationary data with partly separated cycles was measured. Thus it can be concluded that even faster switching intervals would lead to a more or less constant and lower gas impurity compared to a mixed electrolyte cycling strategy while maintaining approximately constant electrolyte concentration.

3.5 Summary

In this study the influence of several alkaline water electrolysis process conditions, namely electrolyte flow rate, concentration, temperature and electrolyte management, on the resulting gas purity was investigated. The experiments were conducted in a lab-scale electrolyzer which was equipped with a 150 cm^2 zero-gap cell and a Zirfon^{TM} Perl UTP 500 separator. Classically alkaline electrolyzers are operated with mixed anolyte and catholyte cycles to compensate the difference in electrolyte concentration caused by the half cell reactions. This operation mode leads to a contamination of the evolved gases with the respective other gas. The experiments within this study lead to the conclusion that this contamination may be reduced by adjustment of the mentioned process conditions and therefore increase the part-load operation range of an alkaline electrolyzer. The obtained results are summarized in the following and demonstrate the influence of the investigated process conditions on the resulting gas purity at a current density of 0.5 $kA\,m^{-2}$ and mixed electrolyte cycles.

- A reduction of the average electrolyte flow rate from 0.461 $L\,min^{-1}$ to 0.195 $L\,min^{-1}$ led to a decrease of the anodic hydrogen content from 1.636 vol% to 0.701 vol%.
- The increase of the electrolyte concentration from 28.9 wt% to 34.2 wt% KOH resulted in a reduction of the anodic hydrogen content from 1.350 vol% to 0.911 vol%.
- An increase of the electrolyte temperature from 50 °C to 80 °C led to a decrease of the anodic hydrogen content from 1.348 vol% to 1.090 vol%.

Furthermore different electrolyte management concepts were evaluated. It could be seen that separation of the electrolyte cycles is able to reduce the H_2 in O_2 content from 1.090 vol% to 0.146 vol% at identical process conditions of 80 °C, 31.7 wt% KOH and a current density of 0.5 $kA\,m^{-2}$. This shows that the gas purity of a classical alkaline electrolyzer is mainly affected through mixing of the gas saturated electrolyte cycles, whereas crossover through the separator plays a minor role. Nevertheless, the gas crossover through the separator was investigated with partly separated electrolyte cycles at various temperatures and electrolyte concentrations. It was observed that crossover through the separator increases with rising temperature and decreasing electrolyte concentration.

Furthermore a dynamic electrolyte cycling strategy was investigated, where the electrolyte was mixed and partly separated continuously. It was observed that this procedure

leads to oscillating hydrogen concentrations between the limiting values for mixed and partly separated mode. On average, the hydrogen content could be reduced by 0.258 vol% at a current density of 1.0 kA m^{-2} compared to the classical mixed mode. An increase of the valve switching frequency led to a smaller amplitude with the same average anodic hydrogen concentration. As a result from these investigations either separation of the electrolyte cycles at low current density and mixing at higher current density is conceivable or a dynamic valve switching strategy could be applied to reduce the gas impurity during electrolyzer operation.

Acknowledgements

This research did not receive any specific grant from funding agencies in the public, commercial, or not-for-profit sectors.

Nomenclature

A_{Sep}	separator area	m^2
$c_{i,0}$	gas solubility of component i in pure water	mol m^{-3}
$c_{i,s}$	gas solubility of component i in salt solution s	mol m^{-3}
c_s	concentration of salt solution s	kmol m^{-3}
$D_{i,j}$	pure diffusion coefficient of component i in component j	m^2 s^{-1}
d_{Sep}	separator thickness	m
E^0	electrode potential	V
F	Faraday constant, 96485	C mol^{-1}
$h_{\mathrm{G},i}$	gas specific model parameter of component i	m^3 kmol^{-1}
$h_{\mathrm{G},i,0}$	gas specific model parameter of component i	m^3 kmol^{-1}
h_i	salt specific model parameter of ion i	m^3 kmol^{-1}
H_i	Henry coefficient of component i	atm
$h_{\mathrm{T},i}$	gas specific model parameter for the temperature effect of component i	m^3 kmol^{-1} K^{-1}
I	electric current	A
j	current density	kA m^{-2}

$J_{i,\mathrm{cross}}$	flux density of component i through the separator	$\mathrm{mol\,s^{-1}\,m^{-2}}$
K	Setchenov constant	1
M	molar mass	$\mathrm{kg\,mol^{-1}}$
n_i	index of ion i in chemical formula	1
p	pressure	Pa
T	temperature	K
$\dot{V}_\mathrm{L}$	liquid volumetric flow rate	$\mathrm{L\,min^{-1}}$
x_i	volumetric fraction of component i	1
ε	porosity	1
ϑ	temperature	°C
ρ	density	$\mathrm{kg\,m^{-3}}$
τ	tortuosity	1

References

[1] S. Jacobsson, V. Lauber. The politics and policy of energy system transformation - Explaining the German diffusion of renewable energy technology. *Energ Policy*, 34(3): 256–276, 2006. DOI: 10.1016/j.enpol.2004.08.029.

[2] G. Gahleitner. Hydrogen from renewable electricity: An international review of power-to-gas pilot plants for stationary applications. *Int J Hydrogen Energ*, 38(5):2039–2061, 2013. DOI: 10.1016/j.ijhydene.2012.12.010.

[3] F. Allebrod, C. Chatzichristodoulou, M. B. Mogensen. Alkaline electrolysis cell at high temperature and pressure of 250 °C and 42 bar. *J Power Sources*, 229:22–31, 2013. DOI: 10.1016/j.jpowsour.2012.11.105.

[4] D. Parra, M. K. Patel. Techno-economic implications of the electrolyser technology and size for power-to-gas systems. *Int J Hydrogen Energ*, 41(6):3748–3761, 2016. DOI: 10.1016/j.ijhydene.2015.12.160.

[5] M. Jentsch, T. Trost, M. Sterner. Optimal use of power-to-gas energy storage systems in an 85 % renewable energy scenario. *Enrgy Proced*, 46:254–261, 2014. DOI: 10.1016/j.egypro.2014.01.180.

[6] B. Bensmann, R. Hanke-Rauschenbach, G. Müller-Syring, M. Henel, K. Sundmacher. Optimal configuration and pressure levels of electrolyzer plants in context of power-to-gas applications. *Appl Energ*, 167:107–124, 2016. DOI: 10.1016/j.apenergy.2016.01.038.

[7] M. Götz, J. Lefebvre, F. Mörs, A. McDaniel Koch, F. Graf, S. Bajohr, R. Reimert, T. Kolb. Renewable power-to-gas: A technological and economic review. *Renew Energ*, 85:1371–1390, 2016. DOI: 10.1016/j.renene.2015.07.066.

[8] Ø. Ulleberg. Modeling of advanced alkaline electrolyzers: A system simulation approach. *Int J Hydrogen Energ*, 28(1):21–33, 2003. DOI: 10.1016/s0360-3199(02)00033-2.

[9] K. Zeng, D. Zhang. Recent progress in alkaline water electrolysis for hydrogen production and applications. *Prog Energ Combust*, 36(3):307–326, 2010. DOI: 10.1016/j.pecs.2009.11.002.

[10] S. Sharma, S. K. Ghosnal. Hydrogen the future transportation fuel: From production to applications. *Renew Sust Energ Rev*, 43:1151–1158, 2015. DOI: 10.1016/j.rser.2014.11.093.

[11] M. Momirlan, T. N. Veziroglu. Current status of hydrogen energy. *Renew Sust Energ Rev*, 6(1-2):141–179, 2002. DOI: 10.1016/S1364-0321(02)00004-7.

[12] M. Hammoudi, C. Henao, K. Agbossou, Y. Dubé, M. L. Doumbia. New multi-physics approach for modelling and design of alkaline electrolyzers. *Int J Hydrogen Energ*, 37(19):13895–13913, 2012. DOI: 10.1016/j.ijhydene.2012.07.015.

[13] L. M. Gandia, R. Oroz, A. Ursua, P. Sanchis, P. M. Dieguez. Renewable hydrogen production: Performance of an alkaline water electrolyzer working under emulated wind conditions. *Energ Fuel*, 21(3):1699–1706, 2007. DOI: 10.1021/ef060491u.

[14] W. Hug, J. Divisek, J. Mergel, W. Seeger, H. Steeb. Highly efficient advanced alkaline electrolyzer for solar operation. *Int J Hydrogen Energ*, 17(9):699–705, 1992. DOI: 10.1016/0360-3199(92)90090-J.

[15] W. Hug, H. Bussmann, A. Brinner. Intermittent operation and operation modeling of an alkaline electrolyzer. *Int J Hydrogen Energ*, 18(12):973–977, 1993. DOI: 10.1016/0360-3199(93)90078-O.

[16] S. G. Bratsch. Standard electrode potentials and temperature coefficients in water at 298.15 K. *J Phys Chem Ref Data*, 18(1):1–21, 1989. DOI: 10.1063/1.555839.

[17] D. Pletcher, L. Xiaohong. Prospects for alkaline zero gap water electrolysers for hydrogen production. *Int J Hydrogen Energ*, 36(23):15089–15104, 2011. DOI: 10.1016/j.ijhydene.2011.08.080.

[18] M. Carmo, D. L. Fritz, J. Mergel, D. Stolten. A comprehensive review on PEM water electrolysis. *Int J Hydrogen Energ*, 38(12):4901–4934, 2013. DOI: 10.1016/j.ijhydene.2013.01.151.

[19] A. Ursua, L. M. Gandia, P. Sanchis. Hydrogen production from water electrolysis: Current status and future trends. *P IEEE*, 100(2):410–426, 2012. DOI: 10.1109/JPROC.2011.2156750.

[20] G. Tjarks, J. Mergel, D. Stolten. *Dynamic Operation of Electrolyzers – Systems Design and Operating Strategies*. Hydrogen Science and Engineering: Materials, Processes, Systems and Technology. Wiley-VCH, Weinheim, 2016. DOI: 10.1002/9783527674268.ch14.

[21] N. Guillet, P. Millet. *Alkaline Water Electrolysis*. Hydrogen Production by Electrolysis. Wiley-VCH, Weinheim, 2015. DOI: 10.1002/9783527676507.ch4.

[22] A. Ursua, I. San Martin, E. L. Barrios, P. Sanchis. Stand-alone operation of an alkaline water electrolyser fed by wind and photovoltaic systems. *Int J Hydrogen Energ*, 38(35):14952–14967, 2013. DOI: 10.1016/j.ijhydene.2013.09.085.

[23] C. A. Schug. Operational characteristics of high-pressure, high-efficiency water-hydrogen-electrolysis. *Int J Hydrogen Energ*, 23(12):1113–1120, 1998. DOI: 10.1016/S0360-3199(97)00139-0.

[24] H. Janssen, J. C. Bringmann, B. Emonts, V. Schroeder. Safety-related studies on hydrogen production in high-pressure electrolysers. *Int J Hydrogen Energ*, 29(7):759–770, 2004. DOI: 10.1016/j.ijhydene.2003.08.014.

[25] V. Schroeder, B. Emonts, H. Janssen, H.-P. Schulze. Explosion limits of hydrogen/oxygen mixtures at initial pressures up to 200 bar. *Chem Eng Technol*, 27(8): 847–851, 2004. DOI: 10.1002/ceat.200403174.

[26] M. Schalenbach, M. Carmo, D. L. Fritz, J. Mergel, D. Stolten. Pressurized PEM water electrolysis: Efficiency and gas crossover. *Int J Hydrogen Energ*, 38(35):14921–14933, 2013. DOI: 10.1016/j.ijhydene.2013.09.013.

[27] S. A. Grigoriev, P. Millet, S. V. Korobtsev, V. I. Porembskiy, M. Pepic, C. Etievant, C. Puyenchet, V. N. Fateev. Hydrogen safety aspects related to high-pressure polymer electrolyte membrane water electrolysis. *Int J Hydrogen Energ*, 34(14):5986–5991, 2009. DOI: 10.1016/j.ijhydene.2009.01.047.

[28] A. Manabe, H. Domon, J. Kosaka, T. Hashimoto, T. Okajima, T. Ohsaka. Study on separator for alkaline water electrolysis. *J Electrochem Soc*, 163(11):3139–3145, 2016. DOI: 10.1149/2.0191611jes.

[29] A. Manabe, M. Kashiwase, T. Hashimoto, T. Hayashida, A. Kato, K. Hirao, I. Shimomura, I. Nagashima. Basic study of alkaline water electrolysis. *Electrochim Acta*, 100:249–256, 2013. DOI: 10.1016/j.electacta.2012.12.105.

[30] S. Weisenberger, A. Schumpe. Estimation of gas solubilites in salt solutions at temperatures from 273 K to 363 K. *AIChE J*, 42(1):298–300, 1996. DOI: 10.1002/aic.690420130.

[31] P. Ruetschi, R. F. Amlie. Solubility of hydrogen in potassium hydroxide and sulfuric acid. Salting-out and hydration. *J Phys Chem*, 70(3):718–723, 1966. DOI: 10.1021/j100875a018.

[32] R. E. Davis, G. L. Horvath, C. W. Tobias. The solubility and diffusion coefficient of oxygen in potassium hydroxide solutions. *Electrochim Acta*, 12(3):287–297, 1967. DOI: 10.1016/0013-4686(67)80007-0.

[33] D. Tromans. Oxygen solubility modeling in inorganic solutions: Concentration, temperature and pressure effects. *Hydrometallurgy*, 50(3):279–296, 1998. DOI: 10.1016/S0304-386X(98)00060-7.

[34] E. Narita, F. Lawson, K. N. Han. Solubility of oxygen in aqueous electrolyte solutions. *Hydrometallurgy*, 10(1):21–37, 1983. DOI: 10.1016/0304-386X(83)90074-9.

[35] M. Chatenet, M. Aurousseau, R. Durand. Comparative methods for gas diffusivity and solubility determination in extreme media: Application to molecular oxygen in an industrial chlorine-soda electrolyte. *Ind Eng Chem Res*, 39(8):3083–3089, 2000. DOI: 10.1021/ie000044g.

[36] M. B. Knaster, L. A. Apel'baum. Solubility of hydrogen and oxygen in concentrated potassium hydroxide solution. *Russ J Phys Ch*, 38:120–122, 1964.

[37] A. Schumpe. The estimation of gas solubilities in salt solutions. *Chem Eng Sci*, 48 (1):153–158, 1993. DOI: 10.1016/0009-2509(93)80291-W.

[38] D. M. Himmelblau. Solubilities of inert gases in water. 0 °C to near the critical point of water. *J Chem Eng Data*, 5(1):10–15, 1960. DOI: 10.1021/je60005a003.

[39] R. L. LeRoy. Industrial water electrolysis: Present and future. *Int J Hydrogen Energ*, 8(6):401–417, 1983. DOI: 10.1016/0360-3199(83)90162-3.

[40] R. Gilliam, J. Graydon, D. Kirk, S. Thorpe. A review of specific conductivities of potassium hydroxide solutions for various concentrations and temperatures. *Int J Hydrogen Energ*, 32(3):359–364, 2007. DOI: 10.1016/j.ijhydene.2006.10.062.

[41] A. Roy, S. Watson, D. Infield. Comparison of electrical energy efficiency of atmospheric and high-pressure electrolysers. *Int J Hydrogen Energ*, 31(14):1964–1979, 2006. DOI: 10.1016/j.ijhydene.2006.01.018.

[42] R. J. Balzer, H. Vogt. Effect of electrolyte flow on the bubble coverage of vertical gas-evolving electrodes. *J Electrochem Soc*, 150(1):11–16, 2003. DOI: 10.1149/1.1524185.

[43] L. J. J. Janssen, E. Barendrecht. Mechanism of mass transfer of indicator ions to an oxygen-evolving and a hydrogen-evolving electrode in alkaline solution. *Electrochim Acta*, 30(5):683–694, 1985. DOI: 10.1016/0013-4686(85)80112-2.

[44] J. Eigeldinger, H. Vogt. The bubble coverage of gas-evolving electrodes in a flowing electrolyte. *Electrochim Acta*, 45(27):4449–4456, 2000. DOI: 10.1016/S0013-4686(00)00513-2.

[45] Y. Tanaka, S. Uchinashi, Y. Saihara, K. Kikuchi, T. Okaya, Z. Ogumi. Dissolution of hydrogen and the ratio of the dissolved hydrogen content to the produced hydrogen in electrolyzed water using SPE water electrolyzer. *Electrochim Acta*, 48(27):4013–4019, 2003. DOI: 10.1016/S0013-4686(03)00541-3.

[46] K. Kikuchi, Y. Tanaka, Y. Saihara, M. Maeda, M. Kawamura, Z. Ogumi. Concentration of hydrogen nanobubbles in electrolyzed water. *J Colloid Interf Sci*, 298(2): 914–919, 2006. DOI: 10.1016/j.jcis.2006.01.010.

[47] H. Vogt. The actual current density of gas-evolving electrodes - Notes on the bubble coverage. *Electrochim Acta*, 78:183–187, 2012. DOI: 10.1016/j.electacta.2012.05.124.

[48] P. Chandran, S. Bakshi, D. Chatterjee. Study on the characteristics of hydrogen bubble formation and its transport during electrolysis of water. *Chem Eng Sci*, 138: 99–109, 2015. DOI: 10.1016/j.ces.2015.07.041.

[49] F. Marangio, M. Santarelli, M. Cali. Theoretical model and experimental analysis of a high pressure PEM electrolyser for hydrogen production. *Int J Hydrogen Energ*, 34 (3):1143–1158, 2009. DOI: 10.1016/j.ijhydene.2008.11.083.

[50] S. A. Grigoriev, V. I. Porembskiy, S. V. Korobtsev, V. N. Fateev, F. Auprête, P. Millet. High-pressure PEM water electrolysis and corresponding safety issues. *Int J Hydrogen Energ*, 36(3):2721–2728, 2011. DOI: 10.1016/j.ijhydene.2010.03.058.

[51] H. Kim, M. Park, K. S. Lee. One-dimensional dynamic modeling of a high-pressure water electrolysis system for hydrogen production. *Int J Hydrogen Energ*, 38(6):2596–2609, 2013. DOI: 10.1016/j.ijhydene.2012.12.006.

[52] M. Schalenbach, G. Tjarks, M. Carmo, W. Lueke, M. Mueller, D. Stolten. Acidic or alkaline? Towards a new perspective on the efficiency of water electrolysis. *J Electrochem Soc*, 163(11):3197–3208, 2016. DOI: 10.1149/2.0271611jes.

[53] M. K. Tham, R. D. Walker, K. E. Gubbins. Diffusion of oxygen and hydrogen in aqueous potassium hydroxide solutions. *J Phys Chem*, 74(8):1747–1751, 1970. DOI: 10.1021/j100703a015.

[54] R. B. Evans, G. M. Watson. Gaseous diffusion in porous media at uniform pressure. *J Chem Phys*, 35(6):2076–2083, 1961. DOI: 10.1063/1.1732211.

[55] A. Kumar, J. Dewulf, H. van Langenhove. Membrane-based biological waste gas treatment. *Chem Eng J*, 136(2-3):82–91, 2008. DOI: 10.1016/j.cej.2007.06.006.

[56] Brochure Zirfon Perl UTP 500. `https://www.agfa.com/sp/global/en/binaries/ZirfonPerl_UTP500_tcm611-56748.pdf`. Accessed: 29 September 2016.

[57] J. Landesfeind, J. Hattendorff, A. Ehrl, W. A. Wall, H. A. Gasteiger. Tortuosity determination of battery electrodes and separators by impedance spectroscopy. *J Electrochem Soc*, 163(7):1373–1387, 2016. DOI: 10.1149/2.1141607jes.

[58] T. Smolinka, E. T. Ojong, J. Garche. *Hydrogen production from renewable energies - Electrolyzer technologies*. Electrochemical Energy Storage for Renewable Sources and Grid Balancing. Elsevier, Amsterdam, 2015. DOI: 10.1016/B978-0-444-62616-5.00008-5.

[59] H. Vogt. On the supersaturation of gas in the concentration boundary layer of gas evolving electrodes. *Electrochim Acta*, 25(5):527–531, 1980. DOI: 10.1016/0013-4686(80)87052-6.

4 Process modelling of an alkaline water electrolyzer

P. Haug, B. Kreitz, M. Koj, T. Turek
Int J Hydrogen Energ **2017**, *42 (24)*, 15689-15707
https://doi.org/10.1016/j.ijhydene.2017.05.031

Abstract

In this paper a model for the prediction of the product gas purity in alkaline water electrolysis is proposed. For the estimation of the exhaust gas compositions the operating conditions, such as current density, electrolyte flow rate, concentration and temperature as well as process management possibilities are considered. The development of the model relies on a classical process engineering approach and depicts the electrolysis cell through coupled continuously stirred-tank reactors. Furthermore, the mass transport phenomena between the phases are considered through the application of Reynolds and Sherwood correlations. Finally, the validation of the model is performed through experiments, which are carried out in a lab-scale electrolyzer with a 150 cm^2 zero-gap cell and KOH electrolyte at atmospheric pressure. This investigation reveals that gas purity in alkaline water electrolysis is mainly affected by mixing the anodic and cathodic electrolyte cycles, which transport dissolved electrolysis products into the opposite half cell compartments. However, this transport mechanism can be significantly reduced by adjustment of the operating conditions of the electrolyzer.

Keywords: alkaline water electrolysis, hydrogen production, mathematical modelling, gas purity, process management

4.1 Introduction

The continuous expansion of renewable energy sources requires a certain regulation and storage capacity to ensure a stable and reliable energy supply. This is inevitable due to the fluctuating power output of wind and solar energy [1, 2]. Small amounts of energy can be efficiently stored with batteries or supercapacitators on short term scales, whereas chemical components such as hydrogen or synthetic natural gas are often considered as possibilities for long-term energy storage [3, 4]. The synthesis of hydrogen can be realized with a power-to-gas plant, which couples a renewable energy source with a water electrolyzer [5, 6]. This hydrogen can then be reelectrified in fuel cells, injected into the natural gas grid or further processed to derived products, like methane or ammonia [7, 8].

Among the different available options, alkaline electrolysis is the most mature and industrially widespread water electrolysis technology [9, 10]. In alkaline electrolysis the electrodes are immersed in a 20 wt% - 40 wt% potassium hydroxide solution and separated by a diaphragm or membrane to keep the evolved product gases apart [11]. During electrolysis hydrogen is formed at the cathode, whereas oxygen production takes place at the anode. Equations (4.1) - (4.3) show the half cell and overall reactions with their electrode potentials against a standard hydrogen electrode at 298.15 K and pH = 13.996 [12].

$$\text{Cathode: } 2\,H_2O + 2\,e^- \longrightarrow H_2 + 2\,OH^- \qquad E^0 = -0.8280\,V \tag{4.1}$$

$$\text{Anode: } 2\,OH^- \longrightarrow 0.5\,O_2 + H_2O + 2\,e^- \qquad E^0 = +0.4011\,V \tag{4.2}$$

$$\text{Overall reaction: } H_2O \longrightarrow H_2 + 0.5\,O_2 \qquad E^0 = -1.2291\,V \tag{4.3}$$

Caused by the different consumption and production of water in the half cells, an electrolyte concentration gradient is formed. Therefore the anodic and cathodic electrolyte cycles are continuously mixed to compensate this difference in electrolyte concentration. However, this cycling strategy limits the typical operation range to 10 % - 40 % of the nominal load [13, 14] as the oxygen purity is drastically reduced through the contamination of hydrogen below this limit. The sources of this contamination are the diffusion through the separator and the mixing of the gas saturated electrolyte solution, which enables

dissolved species to reach the opposite gas separator. Consequently industrial electrolyzers are shutdown as soon as a foreign gas content of 2 vol% is detected in the exhaust [15], which corresponds to about 50 % of the explosion limit of H_2/O_2 mixtures [16]. This is of special importance when the electrolyzer is coupled with a renewable energy source and operated in the low current density range [17].

In the literature the modelling of alkaline electrolyzers has mostly been focused on the prediction of the power demand or hydrogen production capacity. Ulleberg [18] developed a mathematical model, which combines thermodynamics, heat transfer theory and empirical electrochemical relationships for the calculation of the overall cell voltage. The model is often used by other authors as it can easily be applied to different electrolyzers. Thus, Dieguez et al. [19] were able to predict the voltage characteristics of a commercially available electrolyzer with high accuracy and developed the model further to calculate its thermal behavior. Furthermore Amores et al. [20] adapted Ulleberg's model and extended it by taking into account the electrolyte concentration and electrode distance. Their model was able to predict the dynamic voltage characteristics of an electrolyzer coupled with a solar energy supply with a maximum error of 3 %.

A more detailed approach was published by Hammoudi et al. [21] who modelled the single electrode overvoltages by application of the Tafel equation and further considered the voltage drop through gas covering the electrodes. The model was further improved by Henao et al. [22] who also developed a model based on an equivalent circuit of the electrolyzer. A similar approach was published by Milewski et al. [23], who presented an electrical analogy describing the electrolyzer behavior.

Furthermore CFD models describing the two-phase flow in the electrolysis cell are available [24, 25]. Schillings et al. [25] show that the model is applicable for the estimation of the flow velocity profiles and gas holdup in an electrolysis cell and suggest an increase of the laminar electrolyte flow rate for a reduction of the electrolyte resistivity.

A recent publication by Schalenbach et al. [26] compares the overall efficiency of acidic and alkaline electrolyzers considering the cell voltages and the product gas crossover. The model was parameterized with experimental data and finally led to the result, that alkaline electrolysis could overcome the efficiency of acidic electrolysis if thinner separators were employed.

The literature does not yet provide models for the estimation of the product gas quality depending on the operating conditions of the alkaline electrolyzer. However, the knowledge of the lower operation range is mandatory when the alkaline electrolyzer is dynamically operated with a renewable energy source. Thus, this study provides a zero-dimensional model based on a classical process engineering approach for the prediction of the resulting hydrogen and oxygen purity. Furthermore a description of the experimental determination of necessary parameters and the model validation via online gas purity measurements is presented.

4.2 Mathematical model of the alkaline electrolyzer

The aim of the developed model is to estimate the resulting gas purity of an alkaline water electrolyzer as a function of the current density, electrolyte flow rate, temperature and concentration as well as electrolyte cycling strategies. These can be divided into a »mixed mode«, where anolyte and catholyte are mixed continuously to compensate the difference in electrolyte concentration caused by the half cell reactions (cf. Eqs. (4.1) and (4.2)), and a »separated mode« where both cycles are separated from each other to prevent the contamination of the opposite product gas through gas dissolution. The overall model concept is based on classical gas-liquid-reactors with physical absorption as shown in Fig. 4.1.

The electrolysis cell is divided into two continuous stirred-tank reactors (CSTR) j, which are connected through a separator allowing a crossover $N_{\mathrm{cross},i}$ of dissolved species i, being hydrogen and oxygen. Each half cell is fed with a gas free flow of the electrolyte solution $\dot{V}_{\mathrm{L}}^{j}$, whereas gas is evolved at the electrodes with the molar flow rate $n_{\mathrm{R},i}^{j}$ caused by the electrochemical reactions. To estimate the gas partial pressures $p_{\mathrm{out},i}^{j}$ and liquid concentrations $c_{\mathrm{out},i}^{j}$ at the anodic and cathodic exit of the electrolysis cell, it is necessary to implement a heterogeneous two-phase model which considers the phase mass transfer $N_{\mathrm{phys},i}^{j}$ through physical absorption and desorption of the species. In practice the two-phase flow, represented by $\dot{V}_{\mathrm{L}}^{j}$ and $\dot{V}_{\mathrm{G}}^{j}$, leaves the electrolysis cell and enters a gas-liquid-separator like it is shown in Fig. 4.2, which depicts the model flowsheet derived from the lab-scale electrolyzer. Within this model it is assumed that no further phase transition takes place within the separators as the effective mass transfer area and coefficient is small

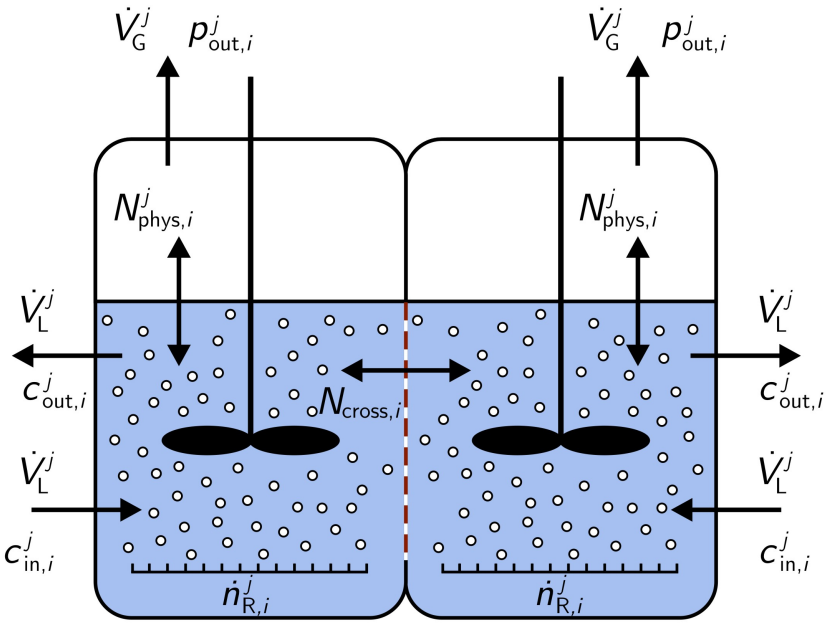

Fig. 4.1: Basic CSTR model concept of the electrolysis cell with occuring fluxes. Compartment j = anodic, cathodic; species i = H_2, O_2, H_2O.

compared to the electrolysis cell. This is caused by bubble coalescence within the tubing behind the exit of the cell and an approximately stagnant fluid in the separators. It is further assumed that the separators behave perfectly, so that only dissolved gases are recycled to the electrolysis cell whereas gas bubbles are removed completely. In »mixed mode« both electrolyte cycles from the anodic and cathodic chamber are merged before they are fed to the electrolysis cell again. In Fig. 4.2 this electrolyte pathway is indicated in green, whereas the »separated mode« is shown in dashed purple.

Furthermore other assumptions and simplifications are made which are summarized in the following:

- stationary process
- ideal CSTR behavior with constant temperature and concentration
- water saturated product gases
- film model for the mass transfer
- neglect of the recombination reaction and assumption of 100 % faradaic efficiency
- monodisperse bubble size distribution
- no mass transfer in pipes and gas separators
- ideal mixer

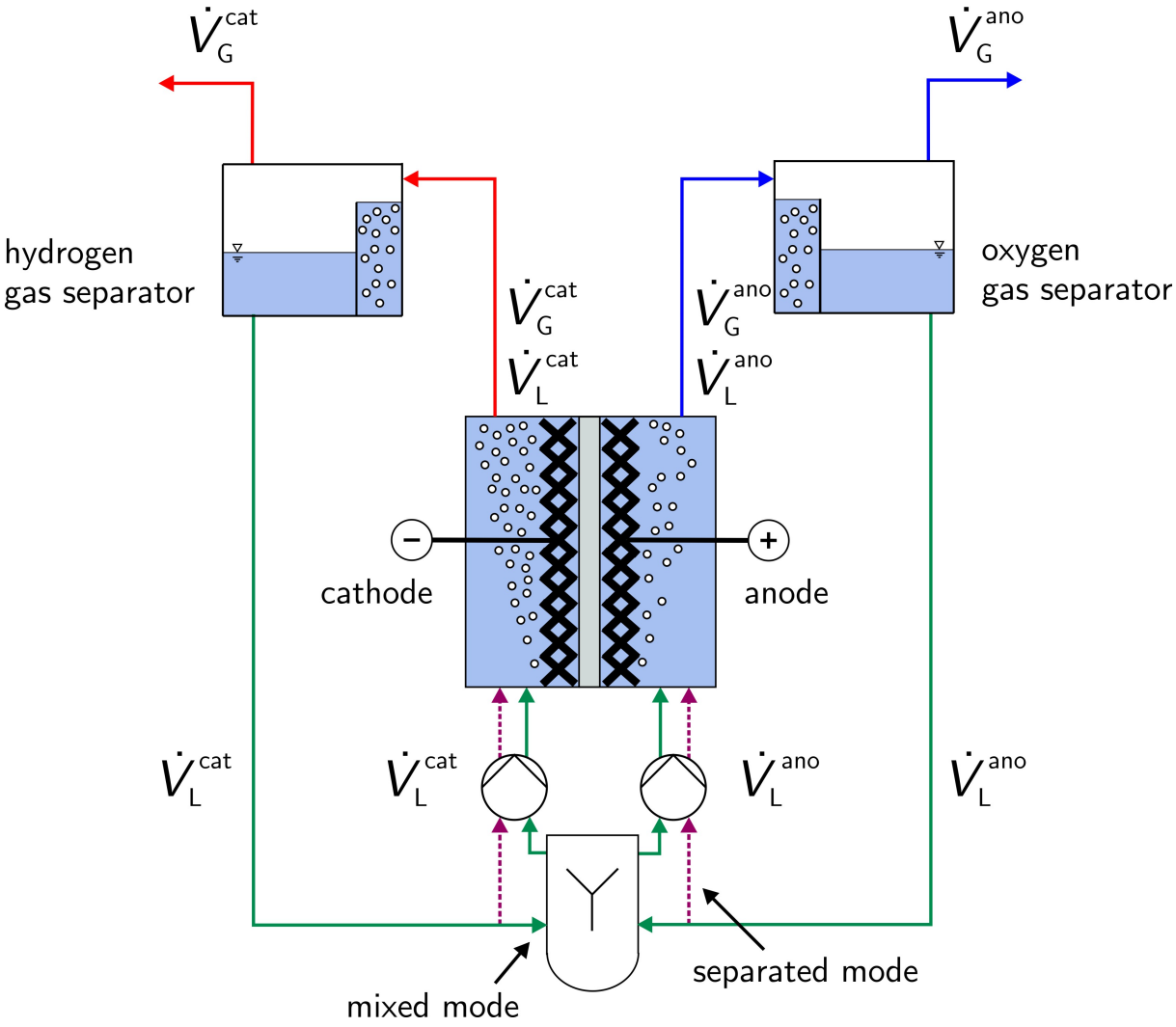

Fig. 4.2: Model flowsheet derived from lab-scale electrolyzer.

The considered gaseous species are hydrogen, oxygen and water whilst only hydrogen and oxygen are taken into account for the liquid phase balance. The crossover through the separator is assumed to occur only in the liquid phase as the solid phase of the employed Zirfon^{TM} separator is reported to be impermeable for gases [27]. Any variations of the OH^- concentrations are assumed to be negligible because of the highly concentrated electrolyte and the continuous replacement of the consumed water in the experimental setup.

The required physical properties, such as the electrolyte viscosity η_L, density ρ_L or diffusion coefficient of the species $D_{i,k}$ are taken from the literature and given in the Appendix. Values, which were found in tables or graphs only, were fitted through appropriate equations and implemented into the model. In the following chapters the model equations and boundary conditions are explained in detail.

4.2.1 Material balance

The material balance of the electrolysis half cells relies on a classical two-phase CSTR, which is a common ideal reactor in chemical engineering [28]. This reactor type is chosen as the half cells are well mixed [25] through gas evolution, which is the reason for bubble induced electrolyte convection [29], and turbulences due to electrolyte entering the cell through nozzles. As shown in Fig. 4.1, the liquid electrolyte enters the half cells with dissolved amounts of hydrogen and oxygen. In the electrolysis cell hydrogen and oxygen is electrochemically produced on the electrodes according to the electrochemical equations (4.1) and (4.2). It is assumed that hydrogen and oxygen are produced in dissolved form [30–32] before gas bubbles grow at active nucleation sites [33] on the electrodes or in the electrolyte bulk. Thus the electrolysis products leave the electrode boundary layer either in dissolved or in gaseous form. This effect is considered in the material balances for the gas and liquid phase through the gas evolution efficiency $f_{G,i}$, which describes the fraction of product leaving the electrode boundary layer in the gaseous phase [34, 35]. A more detailed description of these phenomena is given in the following chapter 4.2.2. The mass transfer between the electrolyte bulk and the gaseous phase is considered using a desorption or absorption flux $N^j_{\text{phys},i}$, whereas the crossover through the separator is described through $N_{\text{cross},i}$, which needs to be added to the liquid anodic material balance and subtracted from its cathodic counterpart. This is due to the definition of the concen-

tration gradient in Fick's law, which is explained in chapter 4.2.4 in detail. With these assumptions the stationary anodic and cathodic liquid (4.4) and gaseous (4.5) material balances write as follows:

$$\begin{aligned} \text{Anode: } 0 = {} & \dot{V}_{\mathrm{L}}^{\mathrm{ano}} \cdot \left(c_{\mathrm{in},i}^{\mathrm{ano}} - c_{\mathrm{out},i}^{\mathrm{ano}}\right) + N_{\mathrm{phys},i}^{\mathrm{ano}} \cdot A_{\mathrm{GL}}^{\mathrm{ano}} \\ & + N_{\mathrm{cross},i} \cdot A_{\mathrm{sep}} + (1 - f_{\mathrm{G},i}) \cdot \dot{n}_{\mathrm{R},i}^{\mathrm{ano}} \end{aligned} \tag{4.4a}$$

$$\begin{aligned} \text{Cathode: } 0 = {} & \dot{V}_{\mathrm{L}}^{\mathrm{cat}} \cdot \left(c_{\mathrm{in},i}^{\mathrm{cat}} - c_{\mathrm{out},i}^{\mathrm{cat}}\right) + N_{\mathrm{phys},i}^{\mathrm{cat}} \cdot A_{\mathrm{GL}}^{\mathrm{cat}} \\ & - N_{\mathrm{cross},i} \cdot A_{\mathrm{sep}} + (1 - f_{\mathrm{G},i}) \cdot \dot{n}_{\mathrm{R},i}^{\mathrm{cat}} \end{aligned} \tag{4.4b}$$

$$0 = \frac{\dot{V}_{\mathrm{G}}^{j}}{R \cdot T} \cdot \left(p_{\mathrm{in},i}^{j} - p_{\mathrm{out},i}^{j}\right) - N_{\mathrm{phys},i}^{j} \cdot A_{\mathrm{GL}}^{j} + f_{\mathrm{G},i} \cdot \dot{n}_{\mathrm{R},i}^{j} \tag{4.5}$$

The solution of these material balances necessitates boundary conditions, which can be derived from the previously described assumptions, electrolyte management strategies and the flowsheet of the electrolyzer model.

In case of mixing anolyte and catholyte both half cells are fed with the same liquid concentration of dissolved species c_i^{mix} from the ideal mixer. Thus the following boundary condition applies:

$$c_{\mathrm{in},i}^{j} = c_i^{\mathrm{mix}} \tag{4.6}$$

If, however, the plant is operated with separated lye cycles the inlet equals the outlet concentration:

$$c_{\mathrm{in},i}^{j} = c_{\mathrm{out},i}^{j} \tag{4.7}$$

As it is assumed that no gas bubbles are recycled from the separators back to the electrolysis cell the inlet partial pressures of the species can be set to zero.

$$p_{\mathrm{in},i}^{j} = 0 \tag{4.8}$$

The absolute pressure of the evolving gas bubbles is defined by equation (4.9) which is the sum of the applied pressure p^0 to the system and an additional pressure Δp^j, which results from the concave curvature of the spherically shaped gas bubbles. This additional pressure can be estimated by applying the Young-Laplace equation (4.10) [36, 37].

$$p^j = p^0 + \Delta p^j \tag{4.9}$$

$$\Delta p^j = 4 \cdot \gamma / d_{\mathrm{b}}^{j} \tag{4.10}$$

Here γ denotes the surface tension of the electrolyte, which is calculated according to the data provided by Feldkamp [38]. As the product gases can be assumed to be saturated with water [39] the water partial pressure p_{H_2O} is equal to the water vapor pressure of the KOH solution, which can be calculated according to Balej [40] in dependence on the electrolyte temperature and concentration. Thus the following relationship between the absolute pressure and the partial pressures of the species applies:

$$p^j = \sum p^j_{\text{out},i} + p_{H_2O} \tag{4.11}$$

Finally, the exit mole fraction of the species can be accessed with the following equation, which considers the removal of water from the exhaust gas flows.

$$x^j_{\text{out},i} = \frac{p^j_{\text{out},i}}{p^j - p_{H_2O}} \tag{4.12}$$

For completion of the model the material balance of the mixing unit is required. With the assumption of an ideal mixer, the material balance can be written as follows:

$$\dot{V}^{\text{mix}}_{\text{L}} \cdot c^{\text{mix}}_i = \sum \dot{V}^j_{\text{L}} \cdot c^j_{\text{out},i} \tag{4.13}$$

4.2.2 Electrochemical reaction

The molar flow rates of the species generated at the electrodes can be calculated with the applied current density J, the electrode area A_{el} and the Faraday constant F according to Faraday's law. The stoichiometric coefficients ν^j_i of the products can be derived from equations (4.1) and (4.2) and amount to $\nu^{\text{cat}}_{H_2} = 1$ and $\nu^{\text{ano}}_{O_2} = 0.5$, if the number of electrons transferred z is set to two.

$$n^j_{\text{R},i} = \frac{\nu^j_i \cdot J \cdot A_{el}}{z \cdot F} \tag{4.14}$$

As already mentioned, the electrolysis products are generated in dissolved form before a growth of gas bubbles becomes possible within the electrode boundary layer. The dissolved species produced there are either transported to the gas-liquid interface of adhering bubbles or to the electrolyte bulk. Since the gas solubility in the highly concentrated alkaline media is low, the electrode boundary layer becomes strongly oversaturated. This supersaturation is mandatory for bubble growth at the electrode as a sufficient deviation from equilibrium is necessary for a nucleation site to become active [30]. Nucleation sites are small electrode surface irregularities, which are strongly dependent on the kind of

material or its roughness [33]. As soon as a nucleation site becomes active bubbles are formed through the supply of dissolved species from the surrounding supersaturated electrolyte. Whether gas is evolved at the electrode or dissolved species are transported to the bulk depends on the operating conditions of the electrolyzer. At low current densities nearly the total amount of produced species is transported to the bulk as the concentration gradient at the electrode is too low for the activation of nucleation sites [41]. If the current density is increased bubbles start to grow at the electrode surface as the supersaturation of the electrolyte becomes high enough to enable diffusion into the gaseous phase. This behavior can be described through the introduction of the gas evolution efficiency $f_{\mathrm{G},i}$, which denotes the fraction of product generated as gas bubbles within the electrode boundary layer [34, 35]. The remaining fraction leaves the boundary layer in dissolved form and may be transported into rising bubbles in a subsequent mass transfer step. Next to the current density the gas evolution efficiency is also affected by the electrode material, electrode potential and the amount of produced gas [41, 42]. It has to be noted that the gas evolution efficiency only reaches unity at very high current densities, while it is significantly smaller in typical electrolysis processes [30].

Vogt [41] published a variety of gas evolution efficiency models as a function of several dimensionless numbers. However due to the complicated flow pattern of the two-phase mixture and the unknown mass transfer behavior of an electrode in a zero-gap assembly a prediction of these numbers is difficult. Thus, empirical correlations have been published which describe the gas evolution efficiency of specific experimental setups. As an example Vogt [43] proposed the following equation (4.15) for a hydrogen evolving electrode in $0.5\,\mathrm{mol\,L^{-1}}$ H_2SO_4 at a temperature of 25 °C and atmospheric pressure.

$$f_{\mathrm{G,H_2}} = 1 - 1.35 \cdot \left(J/\mathrm{A\,m^{-2}}\right)^{-0.095} \tag{4.15}$$

Pierre et al. [44] published another equation for the hydrogen evolution on a Nickel electrode in $1\,\mathrm{mol\,L^{-1}}$ KOH at 25 °C and an electrolyte flow rate of $0.12\,\mathrm{m\,s^{-1}}$, which was derived from the data provided by Chin Kwie Joe et al. [45].

$$f_{\mathrm{G,H_2}} = 0.5653 \cdot \left(1 - \exp\left(-0.002061 \cdot J/\mathrm{A\,m^{-2}}\right)\right) \tag{4.16}$$

Chin Kwie Joe et al. also published data for the oxygen evolution in $1\,\mathrm{mol\,L^{-1}}$ KOH at 25 °C as well as the hydrogen evolution reaction in $6.8\,\mathrm{mol\,L^{-1}}$ NaOH at a temperature

of 80 °C and an electrolyte flow rate of $0.05\,\mathrm{m\,s^{-1}}$. The hydrogen gas evolution efficiency data can be fitted with the following equation:

$$f_{\mathrm{G,H_2}} = 0.16302 \cdot \left(J/\mathrm{A\,m^{-2}}\right)^{0.18527} \tag{4.17}$$

In the present study, the gas evolution efficiency is considered a fitting parameter, because no data for the hydrogen and oxygen evolution reaction under technical relevant conditions, namely 30 wt% KOH and 80 °C, could be found. A description of the fitting procedure is given in chapter 4.3.2.

4.2.3 Mass transfer

The fraction of electrolysis products, which reaches the electrolyte bulk in dissolved form, can be incorporated into the surrounding rising bubbles [30]. This effect is considered by the application of the film theory and the introduction of a species-specific mass transfer coefficient $k^j_{\mathrm{L},i}$.

$$N^j_{\mathrm{phys},i} = k^j_{\mathrm{L},i} \cdot \left(c^{*,j}_i - c^j_{\mathrm{out},i}\right) \tag{4.18}$$

As the electrolyte is supersaturated with the electrolysis products this mass transfer mainly occurs into the direction of the gaseous phase. In film theory, the assumption of a stagnant film between the interconnected phases is made, in which mass transfer only occurs by diffusion. At this interface the gaseous and liquid concentration is assumed to be in equilibrium [46]. If the mass transfer resistance is further assumed to be controlled by the liquid film the liquid equilibrium concentration $c^{*,j}_i$ can be estimated with Henry's law. This assumption is permissible as the solubility of the gases is low [28]. For the estimation of the Henry coefficients in pure water the correlation by Himmelblau [47] is applied, which is necessary for the calculation of the gas solubility in highly concentrated alkaline media using the Setchenov relation [48]. Therefore the Setchenov constants of the species need to be known, which are achieved by fitting the data provided by Knaster and Apel'baum [49] and are shown in the Appendix.

For the estimation of the mass transport coefficient in gas-liquid reactors a variety of Sherwood-Reynolds correlations can be found in the literature. The Reynolds number Re results from the physical properties of the electrolyte, the gas bubble diameter d^j_{b} and the bubble swarm velocity u^j_{sw} [50].

$$Re^j = \frac{\rho_L \cdot d^j_{\mathrm{b}} \cdot u^j_{\mathrm{sw}}}{\eta_{\mathrm{L}}} \tag{4.19}$$

The estimation of the bubble swarm velocity necessitates the rise velocity of a single gas bubble, which can be calculated with the equation by Peebles and Garber [51] for spherical gas bubbles with inner circulation at $Re \geq 2$ [52]. However, the literature provides diverse information about the validity of this equation. According to Kienzlen [53] this equation is also applicable for the estimation of the hydrogen bubble rise velocity in 30 wt% KOH in the range from $1 < Re < 430$. Thus, this equation is applied for the cathodic as well as the anodic bubble rise velocity.

$$u_{\mathrm{b}}^{j} = 0.33 g^{0.76} \left(\frac{\rho_{\mathrm{L}}}{\eta_{\mathrm{L}}}\right)^{0.52} \left(\frac{d_{\mathrm{b}}^{j}}{2}\right)^{1.28} \tag{4.20}$$

A gas bubble, which rises within a swarm, experiences a reduction of the effective rise velocity due to collisions of these bubbles. Kreysa and Kuhn [54] summarized a variety of bubble swarm velocity correlations as a function of the single bubble rise velocity u_{b}^{j} and the gas voidage $\varepsilon_{\mathrm{g}}^{j}$. Here, the reduction of the rise velocity is considered with the equation proposed by Brauer and Thiele [55].

$$u_{\mathrm{sw}}^{j} = u_{\mathrm{b}}^{j} \cdot \frac{1}{1 + \frac{\varepsilon_{\mathrm{g}}^{j}}{\left(1-\varepsilon_{\mathrm{g}}^{j}\right)^{2}}} \cdot \frac{1 - \varepsilon_{\mathrm{g}}^{j}}{1 + \frac{1.05}{\left(1+\frac{0.0685}{\left(\varepsilon_{\mathrm{g}}^{j}\right)^{2}}\right)^{0.5} - 0.5}} \tag{4.21}$$

Under operating conditions of our electrolyzer the mentioned equations lead to Reynolds numbers in the magnitude of $Re \approx 1$. Additionally, the Schmidt number Sc is mandatory for the estimation of the Sherwood number Sh and the mass transfer coefficient, respectively. It is defined by the physical properties of the liquid and the gaseous diffusion coefficient $D_{i,k}$ in the electrolyte.

$$Sc_i = \frac{\eta_{\mathrm{L}}}{\rho_{\mathrm{L}} \cdot D_{i,k}} \tag{4.22}$$

With these equations, it is now possible to find an appropriate Sherwood correlation. We used the equation developed by Brauer and Mewes [50] which is valid for spherical bubbles and $Re \to 0$.

$$Sh_i^{j} = \frac{k_{\mathrm{L},i}^{j} \cdot d_{\mathrm{b}}^{j}}{D_{i,k}} = 2 + \frac{0.651 \cdot \left(Re^{j} \cdot Sc_i\right)^{1.72}}{1 + \left(Re^{j} \cdot Sc_i\right)^{1.22}} \tag{4.23}$$

Thus, mass transfer coefficients for hydrogen and oxygen in the magnitude of $k_{\mathrm{L},i}^{j} \approx 10^{-4}\,\mathrm{m\,s^{-1}}$ are achieved. A comparison with equation (4.24) by Wesselingh and Krishna [46] for small particles or bubbles yields similar values.

$$k_{\mathrm{L},i}^{j} = \frac{2 \cdot D_{i,k}}{d_{\mathrm{b}}^{j}} \tag{4.24}$$

It was shown in the material balance equations (4.4) and (4.5) that the interfacial area A^j_{GL} is required for the calculation of the phase transition fluxes. For an estimation of this area the gas holdup $\varepsilon^j_{\mathrm{g}}$ in the electrolysis half cells must be known. Therefore, the gas fraction $\varepsilon^j_{\mathrm{g,out}}$ at the outlet of the electrolysis cell was experimentally determined, which is described in chapter 4.3.4. However, this measuring method leads to higher gas holdup values than in the electrolysis cell as the gas bubbles coalesce in the tubing behind the cell exit, which causes the pressure of the gaseous phase to decrease since the overpressure due to the spherical shape disappears. Thus, the gas volume and holdup in the electrolysis half cells can be assessed with the following equations.

$$V^j_{\mathrm{gas}} = \varepsilon^j_{\mathrm{g,out}} \cdot V_{\mathrm{hcell}} \cdot \frac{p^0}{p^j} \tag{4.25}$$

$$\varepsilon^j_{\mathrm{g}} = \frac{V^j_{\mathrm{gas}}}{V_{\mathrm{hcell}}} \tag{4.26}$$

For reasons of simplification a monodisperse bubble size distribution is assumed. For a given gas bubble diameter d^j_{b}, the volume V^j_{b} and surface area S^j_{b} of a single spherical bubble can then be achieved through geometrical relationships.

$$V^j_{\mathrm{b}} = \frac{\pi}{6} \cdot \left(d^j_{\mathrm{b}}\right)^3 \tag{4.27}$$

$$S^j_{\mathrm{b}} = \pi \cdot \left(d^j_{\mathrm{b}}\right)^2 \tag{4.28}$$

Finally, the overall interfacial area between the liquid and gaseous phase A^j_{GL} writes as follows:

$$A^j_{\mathrm{GL}} = \frac{V^j_{\mathrm{gas}}}{V^j_{\mathrm{b}}} \cdot S^j_{\mathrm{b}} \tag{4.29}$$

4.2.4 Crossover through the separator

The separator in an alkaline water electrolysis cell has the functions to prevent short circuits between the electrodes and to avoid the mixing of evolved hydrogen and oxygen. For this purpose, the separator needs to be stable under highly alkaline conditions and very conductive for the transport of OH^- ions. The conductivity of a separator mainly depends on its porosity and tortuosity as the current passes through the liquid electrolyte in the pores [56]. Furthermore, these properties influence the transport of dissolved gas through the separator. In PEM (proton exchange or polymer electrolyte membrane) electrolysis modelling gas crossover is typically described through a combination of differential

pressure driven convection and diffusional species transport across the membrane [15, 57–60]. For a proper estimation of these crossover fluxes the electrolyte supersaturation with electrolysis products, which was mentioned in chapter 4.2.2, should be considered as it may enhance the overall species transport across the separator [15, 60]. Alkaline water electrolyzers, however, are usually operated with equal anodic and cathodic pressures, so that only diffusional crossover occurs, which can be described by application of Fick's law.

$$N_{\mathrm{cross},i} = \frac{D_{i,k}^{\mathrm{eff}}}{d_{\mathrm{sep}}} \cdot \left(c_{\mathrm{out},i}^{\mathrm{cat}} - c_{\mathrm{out},i}^{\mathrm{ano}} \right) \tag{4.30}$$

In this equation d_{sep} denotes the separator thickness, whereas $c_{\mathrm{out},i}^{j}$ is the cathodic and anodic concentration of dissolved gas and $D_{i,k}^{\mathrm{eff}}$ the effective diffusion coefficient of the species in the separator. According to equation (4.30) a positive diffusion flux is achieved, if the cathodic is greater than the anodic outlet concentration. This is the case for hydrogen as its liquid concentration is generally higher in the cathodic compartment. This results in a flux of dissolved hydrogen from the cathodic to the anodic half cell. Therefore this flux needs to be subtracted from the liquid, cathodic material balance and added to its anodic counterpart. Moreover, in the case of oxygen, equation (4.30) delivers a negative flux, as the oxygen concentration is always greater in the anodic compartment. This is valid for the anodic material balance, as oxygen diffuses from the anodic to the cathodic compartment. However, in the cathodic compartment this flux needs to be subtracted for an addition to the material balance equation. This is the reason why $N_{\mathrm{cross},i}$ is provided with a positive sign in the anodic and a negative sign in the cathodic compartment.

The calculation of the effective diffusion coefficient requires the molecular diffusion coefficient $D_{i,k}$ in the electrolyte, because the pores are filled with the liquid solution. These binary diffusion coefficients are calculated from polynomials, which represent the data provided by Tham et al. [61] and are shown in the Appendix. Furthermore, the porosity and tortuosity of the separator are required for the estimation of the effective diffusion coefficient.

$$D_{i,k}^{\mathrm{eff}} = D_{i,k} \cdot \frac{\varepsilon}{\tau} \tag{4.31}$$

In the experiments Zirfon$^{\mathrm{TM}}$ Perl UTP 500 by AGFA is used, which is a porous separator consisting of a zirconium oxide coated polyphenylene sulfide mesh. The separator thickness and porosity are given with $d_{\mathrm{sep}} = (500 \pm 50)$ µm and $\varepsilon = 0.5 \pm 0.1$ [62]. Ad-

ditionally, the tortuosity can be estimated from data recently published by Schalenbach et al. [27], who report a ratio of $D^{\text{eff}}_{\text{H}_2,\text{KOH}}/D_{\text{H}_2,\text{KOH}} = 0.159$. Accordingly, equation (4.31) yields a tortuosity of $\tau = 3.14$ if a porosity of $\varepsilon = 0.5$ is applied.

In alkaline water electrolysis the aforementioned electrode boundary layer is strongly oversaturated with the dissolved electrolysis product. The succeeding mass transfer pathway of the product is usually controlled by two competing mechanisms. Thus, the product is either transported to the electrolyte bulk in dissolved form or to the liquid-gas interface of bubbles present in the electrode boundary layer, which is considered through the gas evolution efficiency. This implies, that the flux of dissolved gas from the electrode to the electrolyte bulk changes with electrode distance [63]. Furthermore, the dissolved product may also be transported through the separator, which is considered through application of equation (4.30). As the electrodes are directly pressed onto the diaphragm in a zero-gap configuration, the supersaturated concentration within the electrode boundary should actually be applied for estimation of the diffusional crossover flux. However, due to the assumption of an ideal CSTR with uniform concentration distribution the local concentration gradient from the electrode to the electrolyte bulk cannot be considered in this model yet. Therefore, the model predicts a lower crossover flux through the separator than experimentally determined, as a smaller concentration gradient across the separator is applied for calculation.

4.3 Experimental determination of modelling parameters

The experimental parameterization and validation of the model presented in this study was performed with a fully automated lab-scale electrolyzer, which is described in detail in a previously published paper [64]. Therefore, only a short overview of the overall setup is given in chapter 4.3.1. Furthermore, the model application necessitates the determination of unknown operational parameters, such as the gas evolution efficiency, gas bubble diameter and gas volume in the electrolysis half cells. A description of the determination and applied measurement techniques is also given in the following.

4.3.1 Electrolyzer setup

The electrolysis cell is equipped with a commercially available Zirfon^{TM} PERL UTP 500 separator, a catalyst-coated nickel mesh cathode and a bare nickel mesh anode with a geometrical area of 150 cm^2. These electrodes are pressed directly onto the separator, so that a zero-gap cell setup is achieved. A DC power supply (TDK-Lambda GENH8-90) powers the cell with a maximum of 8 V and 180 A, which is equal to a maximum current density of 12 $kA\,m^{-2}$. The geometrical dimensions of the half cells amount to $(0.16 \times 0.015 \times 0.145)$ m^3 (height $\times$ width $\times$ depth), which result in an overall cell volume of 0.7 L. The electrolyte, which is a potassium hydroxide solution with a concentration of about 31 wt%, is continuously pumped through the electrolysis cell to avoid gas accumulation and to keep the temperature increase small. Downstream of the electrolysis cell the anodic and cathodic gas-liquid mixtures are fed to the gas separators, where either the oxygen or hydrogen is removed from the electrolyte. The gas purity of the gases is measured via online gas chromatography after the water content has been removed by reflux condensers and desiccant dryers. For permanent gas separation and detection, the GC (Agilent 7820A) is equipped with two HP Molesieve Columns and thermal conductivity detectors, so that a simultaneous measurement of the anodic and cathodic gas flows is possible.

4.3.2 Gas evolution efficiency

It was mentioned in chapter 4.2.2 that the gas evolution efficiency is considered a fitting parameter as no information about the hydrogen and oxygen evolution efficiency at technical relevant conditions is available in the literature.

Therefore, the modelled anodic gas purity at mixed electrolyte cycles, an electrolyte flow rate of 330 $mL\,min^{-1}$, a concentration of 31.7 wt% KOH, and a temperature of 80 °C is fitted to the chromatographically determined anodic hydrogen concentration using the parameter estimation function of the gPROMS ModelBuilder. As a result from this fitting process the gas evolution efficiency for the hydrogen evolution reaction as a function of the current density is obtained.

$$f_{G,H_2} = 0.25744 \cdot \left(J/A\,m^{-2}\right)^{0.14134} \tag{4.32}$$

Thusly achieved values are in good agreement with the data reported by Chin Kwie Joe et al. [45], which may be attributed to the similar operating conditions. A comparison of equations (4.15) - (4.17) and (4.32) is shown in Fig. 4.3, which also emphasizes that typical efficiencies are below unity in the industrial current density range.

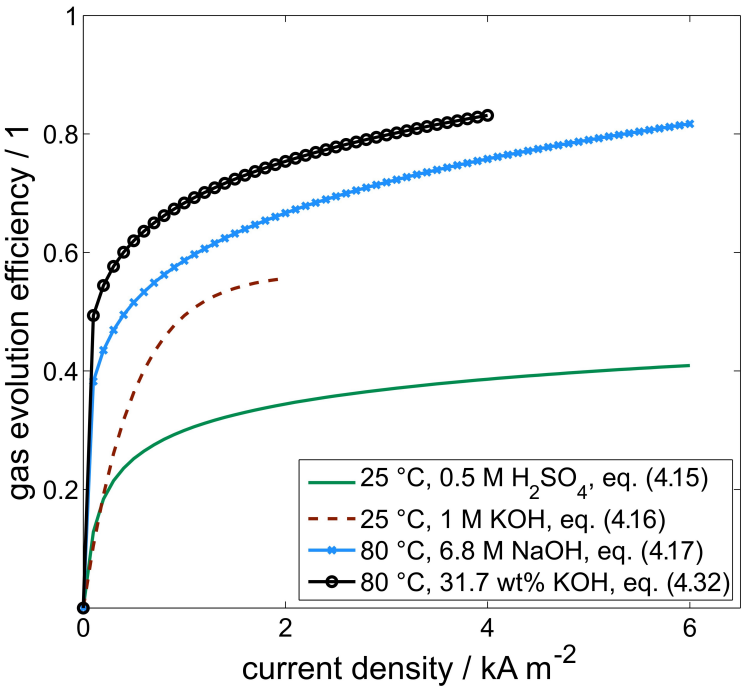

Fig. 4.3: Comparison of gas evolution efficiencies for the hydrogen evolution reaction under various operating conditions.

However, the anodic gas evolution efficiency could hardly be determined by application of the method mentioned above. The cathodic oxygen impurity is typically small compared to the anodic hydrogen content due to the higher production rate of hydrogen, which is evolved in a molar ratio of 2:1 compared to oxygen. With the assumption of a current density dependent O_2 gas evolution efficiency of $f_{G,O_2}(J) < 1$ the model predicts slightly higher cathodic oxygen contents than those determined with the lab-scale electrolyzer. This problem is assumed to be caused by an underestimation of the anodic oxygen mass transfer from the liquid to gaseous phase, which leads to an overestimated dissolved oxygen concentration entering the cathodic half cell. Furthermore, it is possible that the neglected reduction of dissolved oxygen to water at the cathode is responsible for the lower cathodic oxygen content. Thus, the oxygen gas evolution efficiency is defined as unity in the model. Although this is physically incorrect, a sensitivity analysis of the model revealed that the anodic hydrogen content is not influenced by this assumption.

In particular the anodic hydrogen content is of major interest as this impurity limits the part-load region of an alkaline electrolyzer coupled with a renewable energy source [65].

4.3.3 Gas bubble diameter

The gas bubble diameter has an impact on the gas purity in alkaline water electrolysis as it directly influences the mass transfer area of the liquid and gaseous interface. Usually gas bubbles detach from the electrode surface as soon as buoyancy and shear forces exceed the adhesion forces [30]. However, it is difficult to solve this equilibrium of forces as many parameters, such as the roughness of the electrode, the contact angle and the electrolyte velocity in the vicinity of the electrode surface have to be known. Therefore, simplified empirical relations have been developed, which relate the breakoff diameter to operational characteristics of the electrolyzer. Vogt and Balzer [66] found that the diameter $d^j_{\mathrm{b},0}$ estimated with the modified Fritz equation, which is usually applied in heat transfer calculations and valid at zero current, shows good agreement with the regression lines of their measuring data.

$$d^j_{\mathrm{b},0} = 1.20 \cdot \beta^j \cdot \sqrt{\frac{\gamma}{g \cdot \left(\rho_{\mathrm{L}} - \rho^j_{\mathrm{G}}\right)}} \tag{4.33}$$

Experiments [66, 67] have shown that the breakoff diameter decreases with increasing current density, which is assumed to be caused through the stirring effect of nearby bubbles or the electrode potential dependent variation of the contact angle. Vogt and Balzer correlate this varying breakoff diameter with the following equation (4.34), according to which a strong decay of the diameter occurs at low current density while an approximately constant value at a current density $\geq 1\,\mathrm{kA\,m^{-2}}$ is reached.

$$\frac{d^j_{\mathrm{b}}\left(J\right)}{d^j_{\mathrm{b},0}} = \left(1 + 0.2\left(\frac{J}{\mathrm{A\,m^{-2}}}\right)\right)^{-0.45} \tag{4.34}$$

It has to be mentioned, though, that other researchers [68, 69] made contrary observations and reported a growing bubble diameter with increasing current density. Ibl et al. [70] explained this contradiction with the great difference in the observed current density range, possible coalescence [71] and varying measurement techniques. Consequently there is still disagreement in the literature about the exact bubble diameter dependence as it is strongly influenced by the electrode material, the electrolyte and possible additives [42]. Therefore, the bubble diameter in our electrolysis cell was experimentally

determined as no specific data for the used electrodes and electrolyte solution could be found in the literature.

The electrolysis cell frame consists of acrylic glass, which allows an optical access to the backside of the electrode in each half cell compartment. Thus, images of evolved gas bubbles in the electrolyte flow behind the electrodes were taken using a Nikon D5200 DSLR camera equipped with a macro lens. The camera was attached to a tripod in such a way, that always the same part of the electrolysis cell could be photographed. Since with the experimental setup coalesced gas bubbles are photographed as well, the overall interfacial gas-liquid area can be estimated. During the experiments, current density and electrolyte flow rate were systematically varied in order to achieve surface area data as a function of these parameters. Afterwards post processing and evaluation of the images was performed with the open source software ImageJ. The processing steps are shown exemplarily for the cathodic compartment at a current density of $0.1\,\mathrm{kA\,m^{-2}}$ in Fig. 4.4.

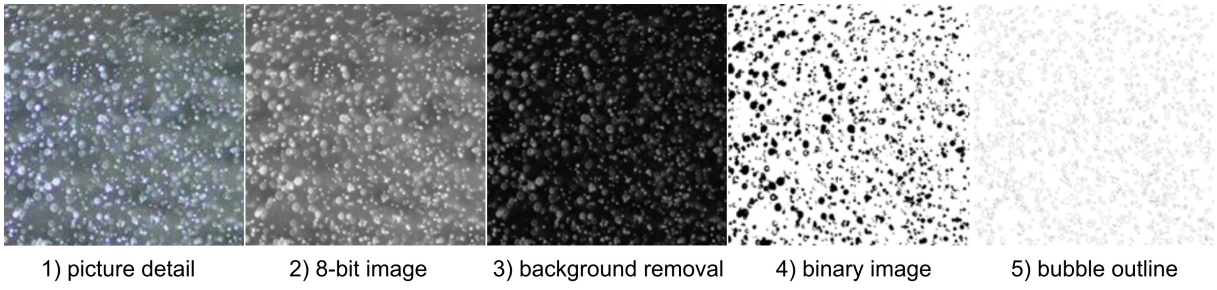

Fig. 4.4: ImageJ processing steps for the determination of anodic and cathodic gas bubble diameters.

Firstly, a specific picture detail was cut from the entire photo, which was then transformed into an 8-bit graphic. Next the background was removed and the image could further be transformed into a binary image, which gave the outlines and therefore the diameter of the spherical bubbles. For the verification of this method the results were partly compared with manually evaluated images.

The current density was varied in the range from $0.1\,\mathrm{kA\,m^{-2}}$ to $3\,\mathrm{kA\,m^{-2}}$ at a KOH concentration of 28.6 wt%, a temperature of 80 °C and three different electrolyte flow rates. The obtained results for the cathodic and anodic compartment are shown in Fig. 4.5 with an exemplary diameter distribution for an electrolyte flow rate of $285\,\mathrm{mL\,min^{-1}}$. The shown diameter equals the mean value of all individually evaluated diameters. It can be seen that the cathodic gas bubble diameter firstly grows from about 170 µm to 220 µm in

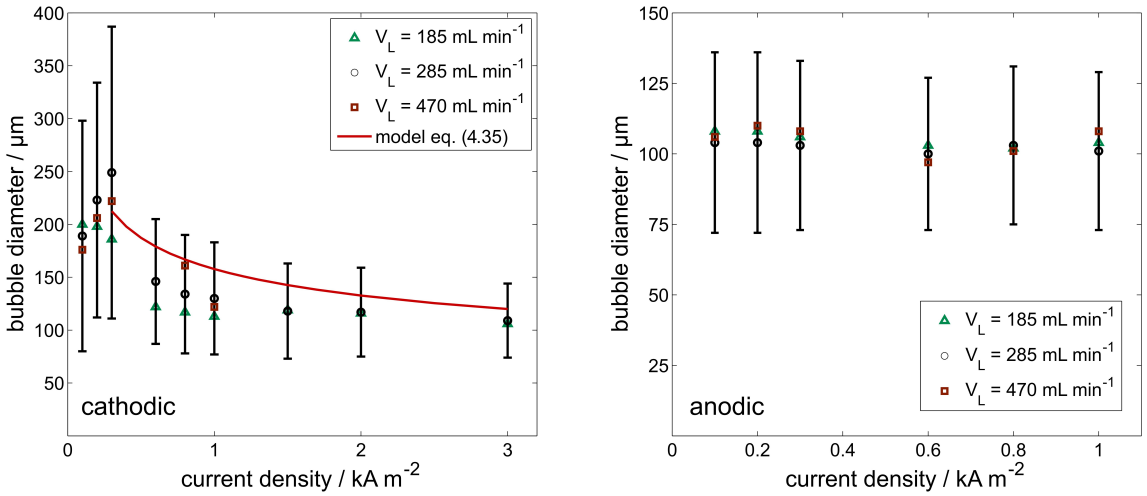

Fig. 4.5: Results of optical gas bubble diameter evaluation in the cathodic and anodic half cell compartments. Operating conditions: $T = 80\,°\mathrm{C}$, $c_{\mathrm{KOH}} = 28.6\,\mathrm{wt\%}$, mixed electrolyte cycles.

the range from $0.1\,\mathrm{kA\,m^{-2}}$ to $0.3\,\mathrm{kA\,m^{-2}}$ and then decreases to an approximately constant value of 115 µm. Furthermore, there is no clear relationship between electrolyte flow rate and bubble diameter. Overall, the observed behavior can be approximately described with an adapted form of equation (4.34) for all electrolyte flow rates, which is valid for a current density $\geq 0.3\,\mathrm{kA\,m^{-2}}$.

$$d_{\mathrm{b}}^{\mathrm{cat}} = 593.84\,\mu\mathrm{m} \cdot \left(1 + 0.2 \cdot \left(\frac{J}{\mathrm{A\,m^{-2}}}\right)\right)^{-0.25} \tag{4.35}$$

However, it must be noted that the analysis of the diameters at current densities $> 0.8\,\mathrm{kA\,m^{-2}}$ becomes uncertain as the high bubble population density blurs the contours of the single gas bubbles. The same problem occurs during the evaluation of the anodic gas bubble diameters, where the bubble population density already reaches critical values at a current density of $0.2\,\mathrm{kA\,m^{-2}}$. Therefore, the anodic bubble diameter is assumed to be 100 µm for all electrolyte flow rates in this model.

4.3.4 Gas holdup

It was shown in chapter 4.2.3 that the gas holdup is necessary for the calculation of the bubble swarm velocity and the interfacial area between the liquid and gaseous phase. Due to the application of a highly concentrated potassium hydroxide solution in the electrolysis process it is possible to perform conductivity measurements for the determination of the

gas voidage at the outlet of the electrolysis cell. The electrical conductivity of a liquid is reduced through the dispersion of gas within this solution and directly related to the gas voidage through the Bruggemann equation [72].

$$\frac{\kappa_{\mathrm{L}}}{\kappa_{\mathrm{L},0}} = \left(1 - \varepsilon^{j}_{\mathrm{g,out}}\right)^{\frac{3}{2}} \tag{4.36}$$

Here $\kappa_{\mathrm{L},0}$ and κ_{L} denote the conductivity of the gas-free liquid and the dispersion, respectively. For the determination of the gas voidage $\varepsilon^{j}_{\mathrm{g,out}}$ the outgoing gas-liquid flows of the cathodic and anodic compartment were led through a measurement cell, where the flow had to pass a conductivity sensor (WTW TetraCon® 925; 0.01 mS cm^{-1} - 2000 mS cm^{-1}; ±0.5 % of value) with a cross-sectional area of (6 × 30) mm^2 (width × height). Before the start of the electrolysis the conductivity of the gas-free electrolyte was determined at 80 °C and 28.6 wt% KOH. Then conductivity values for each current density and electrolyte flow rate were recorded every second for 5 min and averaged afterwards to compensate the fluctuation of the measurement. The obtained results are shown in Fig. 4.6 for a current density range of 0.1 kA m^{-2} - 4 kA m^{-2} and identical electrolyte flow rates as during the gas bubble diameter determination.

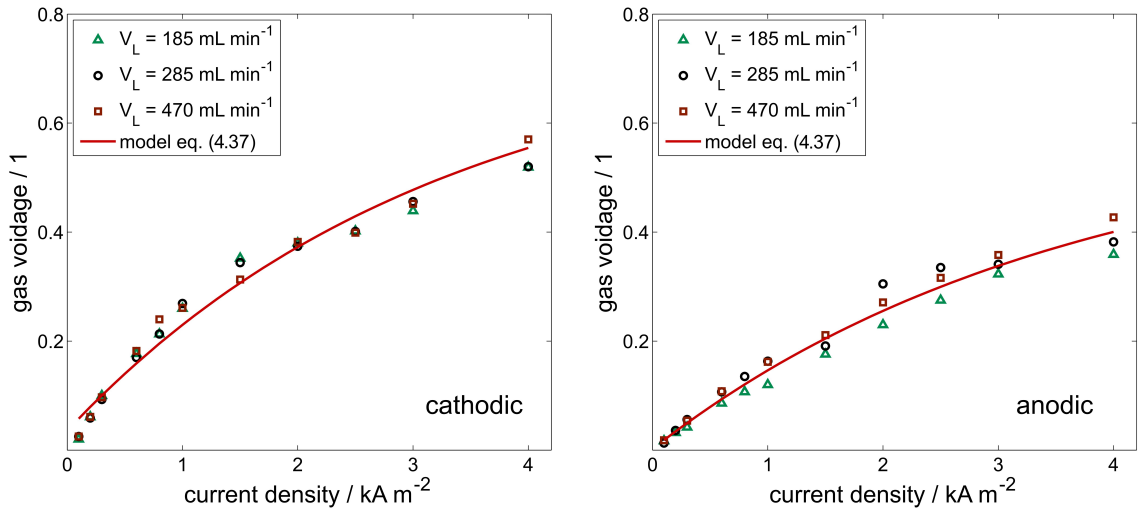

Fig. 4.6: Experimentally determined gas voidages at the cathodic and anodic electrolysis cell outlet. Operating conditions: T = 80 °C, c_{KOH} = 28.6 wt%, mixed electrolyte cycles.

It is evident that the cathodic and anodic gas fraction at the cell outlet increases with growing current density, which is simply a consequence of the higher gas production rate. Furthermore, it can be seen that the electrolyte flow rate or velocity, which only slightly

changes from $1.4\,\mathrm{mm\,s^{-1}}$ to $3.6\,\mathrm{mm\,s^{-1}}$, hardly influences the gas voidage in the investigated current density range. Additionally both gas voidage trends seem to reach limiting values at even higher current densities, which has been reported in the literature [54] before. Nevertheless, it should be noted, that the demonstrated gas voidage trends are only valid for the applied lab-scale electrolyzer as these are heavily dependent on the cell geometry and flow conditions.

For the integration into the model, equation (4.37) describing the anodic and cathodic gas voidage in dependence of the current density was developed. The required parameters are shown in Table 4.1 and the equation is assumed to be valid for all electrolyte flow rates from $185\,\mathrm{mL\,min^{-1}}$ to $470\,\mathrm{mL\,min^{-1}}$. In the low current density range, the cathodic gas voidage is overestimated by the fit function. Due to the validity range of the cathodic bubble diameter equation (4.35), the developed model is applicable for a current density $\geq 0.3\,\mathrm{kA\,m^{-2}}$, where the gas voidage is accurately represented.

Tab. 4.1: Parameters of equation (4.37) for estimation of the anodic and cathodic gas holdup.

Compartment	X_1	X_2	X_3
Anodic	0.59438	0.59231	0.75647
Cathodic	0.76764	0.73233	0.73457

$$\varepsilon^{j}_{\mathrm{g,out}} = X_1 - X_2 \cdot X_3^{\left(\frac{J}{1000\,\mathrm{A\,m^{-2}}}\right)} \tag{4.37}$$

4.4 Validation and results of gas purity modelling

This chapter presents the model validation through a comparison of the modelling results and the experimentally determined product gas purity. Furthermore, the influence of specific sub models, like gas solubility or mass transfer coefficient estimations, on the models' results shall be investigated as the literature offers a wide variety of available estimation possibilities. Therefore, alternative sub models have also been integrated and compared to the results, which are achieved with the equations depicted in chapter 4.2. The outcome of this sensitivity analysis will also be shown in the following.

It was mentioned before that the cathodic foreign gas content is overestimated by the model if an oxygen gas evolution efficiency $f_{G,O_2} < 1$ is applied. Therefore, this efficiency was determined to be unity regardless of the actual current density. Typically the cathodic oxygen concentration is of minor interest as the lower operating limit of an alkaline electrolyzer is mainly restricted by the anodic hydrogen content [17]. On the one hand this is caused by the fact that twice the amount of hydrogen compared to oxygen is produced in the process. On the other hand hydrogen is more soluble in the alkaline electrolyte [49] and has a higher molecular diffusion coefficient [61], which results in a greater flux through the separator. Fig. 4.7 shows a comparison of the modelled and measured gas concentrations in the exhaust gas flows. It can be seen that the model is able to predict the measured anodic and cathodic values with good accuracy for an average electrolyte flow rate of $\dot{V}_L = 330\,\mathrm{mL\,min^{-1}}$, a temperature of 80 °C, an electrolyte concentration of 31.7 wt% and mixed electrolyte cycles. Furthermore, Table 4.2 lists an excerpt of important model parameter values at identical operating conditions and a current density of $0.5\,\mathrm{kA\,m^{-2}}$ to provide an overview on their order of magnitude and how they were achieved.

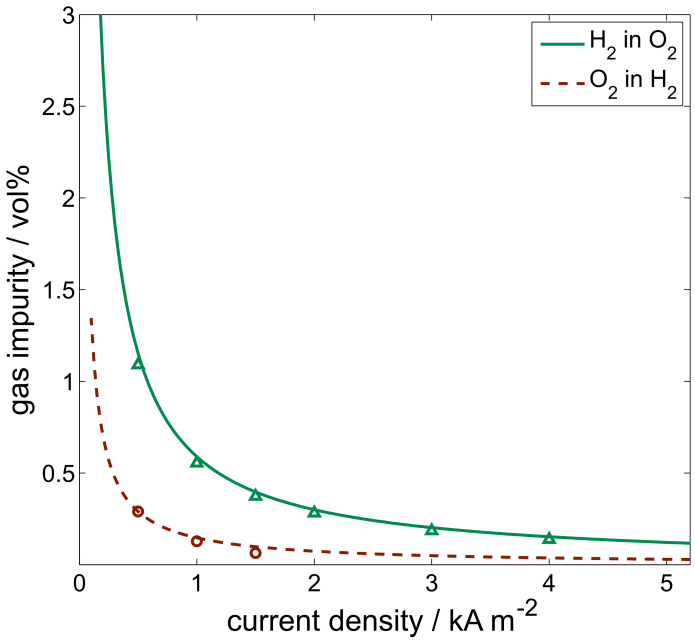

Fig. 4.7: Comparison of experimentally determined (symbols) and modelled (lines) anodic and cathodic foreign gas concentration as a function of current density. Operating conditions: $\dot{V}_L = 330\,\mathrm{mL\,min^{-1}}$, $T = 80\,°\mathrm{C}$, $c_{KOH} = 31.7\,\mathrm{wt\%}$, mixed electrolyte cycles.

Tab. 4.2: Overview of parameters and their values at specific operating conditions: $J = 0.5\,\mathrm{kA\,m^{-2}}$, $\dot{V}_\mathrm{L} = 330\,\mathrm{mL\,min^{-1}}$, $T = 80\,^\circ\mathrm{C}$, $c_\mathrm{KOH} = 31.7\,\mathrm{wt\%}$, mixed electrolyte cycles.

Parameter	Value	Source
$c^{*,\mathrm{cat}}_{\mathrm{H_2}}$	$0.056\,\mathrm{mol\,m^{-3}}$	[49]
$c^{*,\mathrm{ano}}_{\mathrm{H_2}}$	$6.4 \cdot 10^{-4}\,\mathrm{mol\,m^{-3}}$	[49]
d_sep	$500 \pm 50\,\mu\mathrm{m}$	[62]
$D_{\mathrm{H_2,KOH}}$	$5.38 \cdot 10^{-9}\,\mathrm{m^2\,s^{-1}}$	[61]
η_L	$8.76 \cdot 10^{-4}\,\mathrm{Pa\,s}$	[73]
ε	0.5 ± 0.1	[62]
τ	3.14	[27]
$p_{\mathrm{H_2O}}$	27583 Pa	[40]
p^0	101325 Pa	
$d^\mathrm{cat}_\mathrm{b}$	187 µm	experimental, eq. (4.35)
$\varepsilon^\mathrm{cat}_\mathrm{g,out}$	0.14	experimental, eq. (4.37)
$\varepsilon^\mathrm{ano}_\mathrm{g,out}$	0.08	experimental, eq. (4.37)
$f_{\mathrm{G,H_2}}$	0.62	fit, eq. (4.32)

In the following sections, only the influence of the operating conditions on the anodic hydrogen content is discussed as the oxygen content in the cathodic exhaust is always smaller and therefore less important for the safe operation of an alkaline electrolyzer.

4.4.1 Sensitivity analysis

The following sensitivity analysis is performed for several mass transfer, bubble rise velocity and solubility calculation methods. The analysis reveals that the obtained results are particularly dependent on the applied solubility model whereas the bubble rise velocity and mass transfer correlations are of minor importance as the predicted values are mostly in the same order of magnitude. Thus the mass transfer correlation by Brauer and Mewes [50], which is applied in this model, leads to values of $k^\mathrm{cat}_{\mathrm{L,H_2}} = 3.96 \cdot 10^{-4}\,\mathrm{m\,s^{-1}}$ and $k^\mathrm{cat}_{\mathrm{L,O_2}} = 2.09 \cdot 10^{-4}\,\mathrm{m\,s^{-1}}$ at a temperature of 80 °C, a KOH concentration of 31.7 wt% and a current density of $0.5\,\mathrm{kA\,m^{-2}}$. This current density is chosen as a reference point

as the lower operation limit of the electrolyzer is of special importance in this study. The predicted bubble swarm velocity at identical operating conditions yields values of $u_{\mathrm{sw}}^{\mathrm{cat}} = 0.93\,\mathrm{cm\,s^{-1}}$ and $u_{\mathrm{sw}}^{\mathrm{ano}} = 0.59\,\mathrm{m\,s^{-1}}$, whereas the single bubble velocities amount to $u_{\mathrm{b}}^{\mathrm{cat}} = 2.0\,\mathrm{cm\,s^{-1}}$ and $u_{\mathrm{b}}^{\mathrm{ano}} = 0.93\,\mathrm{cm\,s^{-1}}$, respectively. The application of either the single bubble or swarm velocity hardly influences the outcome of the anodic gas purity, as only a difference of 0.1 vol% is obtained. Nevertheless, the single bubble velocity leads to a slightly improved anodic gas purity as it enhances the mass transfer from the liquid to gaseous phase and therefore reduces the concentration of solved species, which are fed to the opposite half cells.

The gas solubility model can be clearly identified as the main influencing factor for the resulting gas purity. In the present model, the hydrogen and oxygen solubility are estimated through application of the Setchenov relation. A description of this solubility model has already been published in a previous paper [64], where the specific Setchenov constants were calculated according to Weisenberger and Schumpe [48]. However, it turned out that the temperature dependence of the hydrogen Setchenov constant is not precisely predicted and therefore leads to an overestimation of the hydrogen solubility under electrolysis process conditions. Consequently the Setchenov constants in this study are fitted to the data by Knaster and Apel'baum [49], who reported a descending hydrogen and oxygen solubility in highly concentrated potassium hydroxide solution at 21 °C - 75 °C. Fig. 4.8 compares the modelling results of the anodic hydrogen content, which are obtained by application of different gas solubility models available in the literature. Hereby the black dots represent the simulation results, which are achieved with the solubility data provided by Knaster and Apel'baum, whereas the Setchenov constants by Weisenberger and Schumpe lead to the concentration shown in dashed red. The comparison indicates that the anodic hydrogen content increases by 0.63 vol%, when the hydrogen saturation concentration changes from $0.058\,\mathrm{mol\,m^{-3}}$ to $0.105\,\mathrm{mol\,m^{-3}}$ at a current density of $0.5\,\mathrm{kA\,m^{-2}}$, as estimated according to Knaster and Apel'baum or Weisenberger and Schumpe, respectively. Furthermore an alternative oxygen solubility model by Tromans [74] was implemented and compared with our results. Tromans' model predicts an approximately 35 % higher oxygen saturation concentration at the identical process conditions of Fig. 4.8, which consequently leads to a significant increase of the cathodic oxygen concentration. However, the applied oxygen solubility model does not affect the

anodic hydrogen concentration as can be seen from the identical results obtained with the hydrogen solubility according to Knaster and Apel'baum and Tromans' oxygen solubility model depicted in solid green.

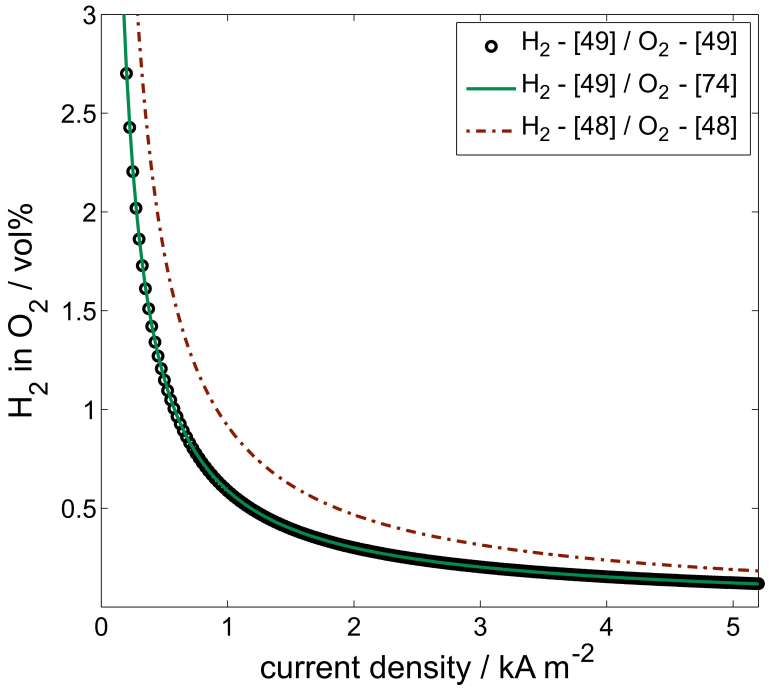

Fig. 4.8: Comparison of anodic hydrogen content as a function of current density and different gas solubility models. (black dots) hydrogen and oxygen solubility according to Knaster and Apel'baum [49], (solid green) hydrogen solubility according to Knaster and Apel'baum [49], oxygen solubility according to Tromans [74], (dashed red) hydrogen and oxygen solubility according to Weisenberger and Schumpe [48]. Operating conditions: $\dot{V}_{\mathrm{L}} = 330\,\mathrm{mL\,min^{-1}}$, $T = 80\,^{\circ}\mathrm{C}$, $c_{\mathrm{KOH}} = 31.7\,\mathrm{wt\%}$, mixed electrolyte cycles.

4.4.2 Effect of electrolyte flow rate

Three different electrolyte flow rates were fed to the half cells for investigating the impact of the electrolyte flow rate on the gas purity. Due to the fact that the electrolyte pumps did not behave perfectly the same, different effective flow rates resulted at identical set points. These effective flow rates were used for the parameter variation in the model and are shown in Table 4.3. For the reason of clarity, it will only be referred to the mean electrolyte flow rate in the following, which is also shown in Table 4.3.

Tab. 4.3: Experimentally determined cathodic, anodic and average electrolyte flow rate at a temperature of 80 °C and a KOH concentration of 31.7 wt%.

$\dot{V}_{\mathrm{L}}^{\mathrm{cat}}$	$\dot{V}_{\mathrm{L}}^{\mathrm{ano}}$	avg. $\dot{V}_{\mathrm{L}}$
$\mathrm{mL\,min^{-1}}$	$\mathrm{mL\,min^{-1}}$	$\mathrm{mL\,min^{-1}}$
205	185	195
375	285	330
452	470	461

A comparison of the measured and modelled anodic hydrogen content is given in Fig. 4.9. The left-hand graph reveals that the model results are in good agreement with the experimentally determined values and that an increasing electrolyte flow rate leads a decline of the gas quality, especially in the part-load operation range when mixing the electrolyte cycles. This behavior is caused through the higher feed of dissolved species to the opposite half cell. This can be clearly seen from comparison of the anodic hydrogen desorption fluxes at a current density of $0.5\,\mathrm{kA\,m^{-2}}$, which amount to $N_{\mathrm{phys,H_2}}^{\mathrm{ano}} = 8.66 \cdot 10^{-8}\,\mathrm{mol\,m^{-2}\,s^{-1}}$ and $N_{\mathrm{phys,H_2}}^{\mathrm{ano}} = 19.46 \cdot 10^{-8}\,\mathrm{mol\,m^{-2}\,s^{-1}}$ for the lowest and highest electrolyte flow rates, respectively. Furthermore, it can be deducted from the results that the anodic gas purity follows a linear trend within the investigated flow rate range at a constant current density as it is shown in Fig. 4.9 (right) for three different current densities. Consequently, a smaller electrolyte flow rate is preferable in terms of gas quality and may be able to enhance the lower operation limit if the electrolyzer is operated with mixed electrolyte cycles. Nevertheless, the electrolyte flow rate should be high enough to avoid an increase of the electrode bubble coverage, which leads to an additional voltage drop and therefore reduces the efficiency of the electrolysis cell.

4.4.3 Effect of electrolyte concentration

The electrolyte concentration directly influences both gas solubility and diffusion coefficients of the dissolved species. The gas solubility mostly decreases with a growing electrolyte concentration, which is commonly described as salting-out effect [75]. Furthermore, the diffusion coefficients also decrease due to an increase of the solution viscosity.

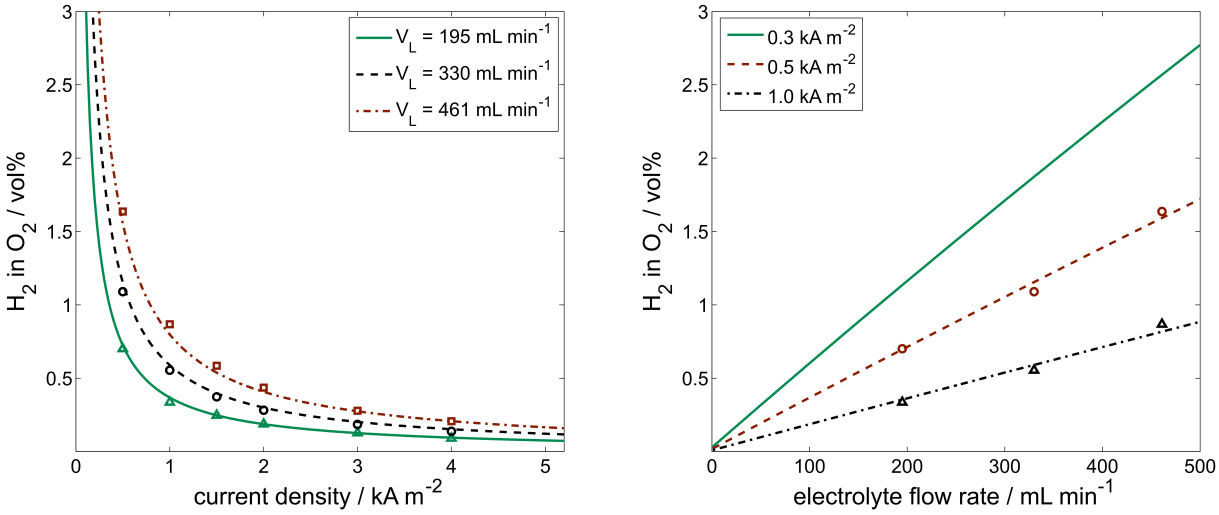

Fig. 4.9: (left) Comparison of experimentally determined (symbols) and modelled (lines) anodic hydrogen content as a function of current density and (right) electrolyte flow rate. Operating conditions: $T = 80\,°C$, $c_{KOH} = 31.7\,wt\%$, mixed electrolyte cycles.

The anodic hydrogen content was experimentally determined for electrolyte concentrations of 28.6 wt%, 31.7 wt% and 34.2 wt% KOH and is compared with the modelling results in Fig. 4.10. It can be seen that a good agreement is achieved, although the gas evolution efficiency determined at 31.7 wt% KOH (cf. eq. (4.32)) has been applied for the whole investigated concentration range. The oxygen impurity decreases with a growing electrolyte concentration at a given current density as can be seen in Fig. 4.10 (right). The reduction of the anodic hydrogen content is mainly due to the lower saturation concentration at higher electrolyte concentrations, which is reduced from $0.108\,mol\,m^{-3}$ to $0.061\,mol\,m^{-3}$ at 80 °C, a hydrogen partial pressure of 101325 Pa and 27 wt% or 35 wt% KOH, respectively. Furthermore, the gas-liquid mass transfer is additionally reduced through smaller mass transfer coefficients, which result from the diminishing binary diffusion coefficients at higher electrolyte concentrations. However, it has to be noted that a concentration increase above 32.5 wt% leads to a reduction of the electrical conductivity at 80 °C [76]. Therefore, an economic analysis considering the gas purity and the power consumption of an electrolyzer should be carried out for an optimized operation.

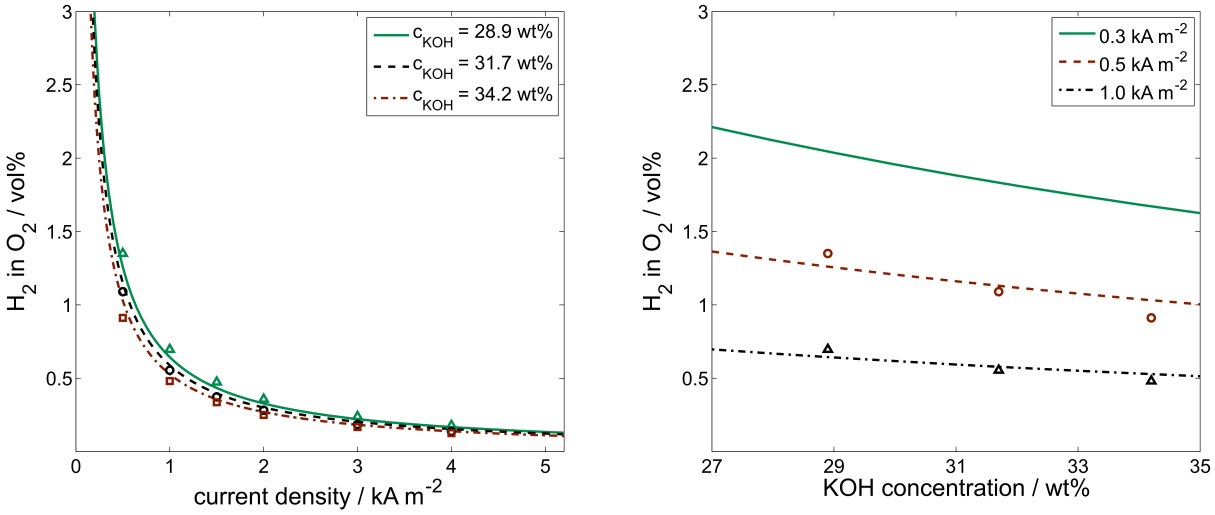

Fig. 4.10: (left) Comparison of experimentally determined (symbols) and modelled (lines) anodic hydrogen content as a function of current density and (right) electrolyte concentration. Operating conditions: $\dot{V}_\mathrm{L} = 330\,\mathrm{mL\,min^{-1}}$, $T = 80\,^\circ\mathrm{C}$, mixed electrolyte cycles.

4.4.4 Effect of temperature

Further measurements and simulations were carried out at temperatures of 50 °C, 70 °C and 80 °C. Due to the fact that the binary diffusion coefficients of O_2 and H_2 in KOH solution were only available for 40 °C, 60 °C and 80 °C [61] the simulation at 50 °C was carried out with the coefficient of 60 °C, whereas the diffusion coefficient of 80 °C was used for the simulations at 70 °C and 80 °C. According to the experimental data of Knaster and Apel'baum [49] the gas solubility is reduced with an increasing electrolyte temperature. The model also reveals that the gas purity is reduced with elevated process temperature, which is depicted in Fig. 4.11. A comparison with the experimentally obtained results shows that the anodic gas purity at 70 °C and 80 °C can be predicted with good accuracy, whereas the data is slightly overestimated at a temperature of 50 °C. Thus, the model predicts a hydrogen content of 1.48 vol% at 50 °C and 0.5 kA m^{-2}, which is about 0.2 vol% higher than the experimental value. This difference is believed to be caused by an overestimation of the applied diffusion coefficient or the hydrogen solubility. For a more detailed modelling a temperature dependent Setchenov constant could be implemented as the applied one results from averaging the data by Knaster and Apel'baum.

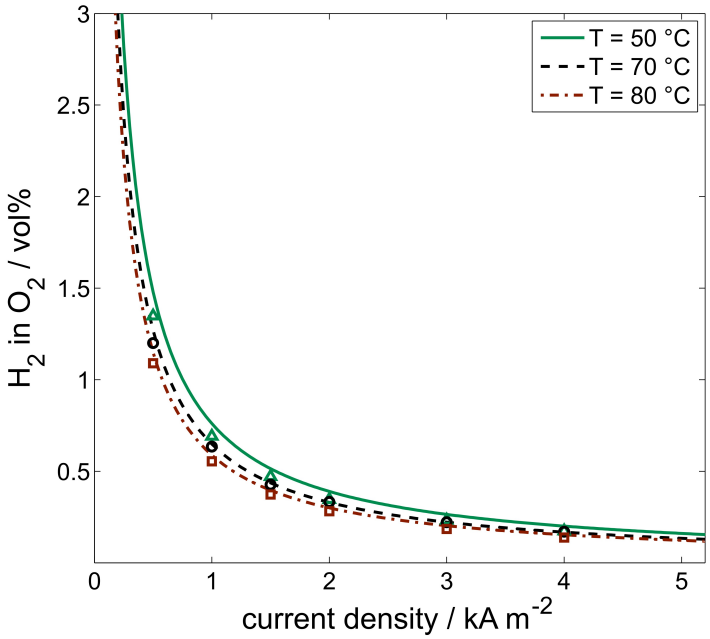

Fig. 4.11: Comparison of experimentally determined (symbols) and modelled (lines) anodic hydrogen content as a function of current density and electrolyte temperature. Operating conditions: $\dot{V}_{\mathrm{L}} = 330\,\mathrm{mL\,min^{-1}}$, $c_{\mathrm{KOH}} = 31.0\,\mathrm{wt\%}$, mixed electrolyte cycles.

4.4.5 Effect of process management

Besides the classical mixing of the electrolyte cycles the electrolyzer was also operated with separated cycles for the improvement of the product gas quality. In separated operation a decrease from 1.090 vol% to only 0.146 vol% H_2 in O_2 could be achieved experimentally. The separation of the lye cycles is able to drastically reduce the foreign gas content as the convective transport of dissolved species to the opposite half cell is avoided in this operation mode. Thus, gas crossover can only occur due to transport of dissolved species through the separator, which is considered by application of Fick's law (cf. eq. (4.30)). A comparison of the modelled and measured anodic hydrogen content when mixing and separating the electrolyte cycles is given in Fig. 4.12 (left). It is obvious that the gas crossover is underestimated by the model as the calculated concentration gradient across the separator is smaller than in the experiment, which results from the assumption of an ideal CSTR. Furthermore, gas could also be transported through the separator due to a pressure gradient, which has been neglected in the present model as the experimental values were determined at balanced ambient pressure. Nevertheless, this effect may play

a significant role when the electrolyzer is operated at elevated pressure and has therefore been considered in the publication by Schalenbach et al. [26].

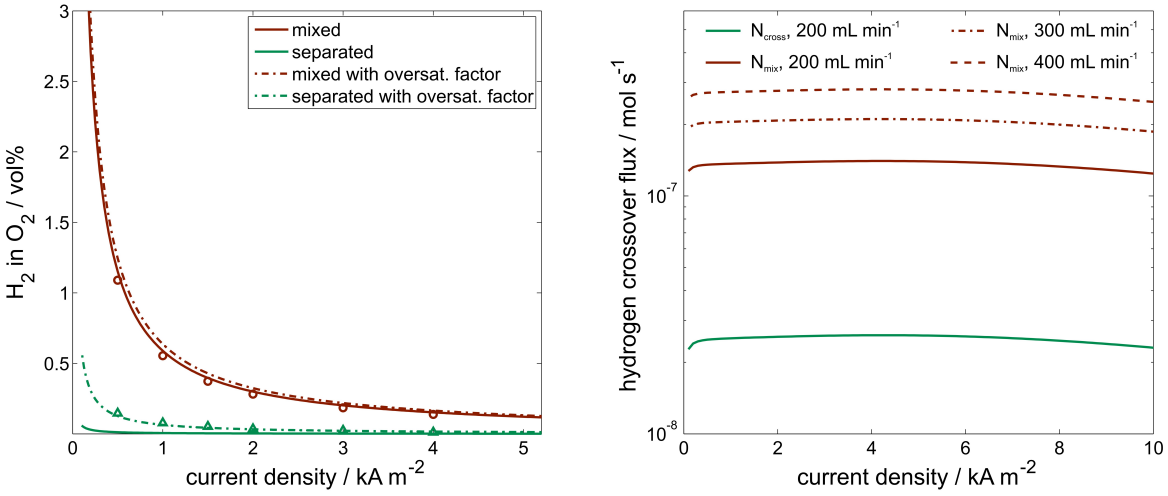

Fig. 4.12: (left) Comparison of experimentally determined (symbols) and modelled (lines) anodic hydrogen content as a function of current density and electrolyte management. Additionally demonstration of modelling results with and without implemented oversaturation factor. Operating conditions: $\dot{V}_\mathrm{L} = 330\,\mathrm{mL\,min^{-1}}$, $T = 80\,^\circ\mathrm{C}$, $c_\mathrm{KOH} = 31.7\,\mathrm{wt\%}$, mixed electrolyte cycles. (right) Comparison of hydrogen crossover mechanisms with implemented oversaturation factor as a function of current density and electrolyte flow rate. Operating conditions: $T = 80\,^\circ\mathrm{C}$, $c_\mathrm{KOH} = 31.7\,\mathrm{wt\%}$, mixed electrolyte cycles.

In order to achieve a better agreement between measured and modelled results at separated cycles, an oversaturation factor was implemented into the model, which simply multiplies the dissolved hydrogen concentration in the cathodic chamber. The fitting to the measured anodic hydrogen content yields an oversaturation of 10 times the equilibrium concentration of hydrogen at a current density of $0.5\,\mathrm{kA\,m^{-2}}$, which results in a molar flux of $N_{\mathrm{cross,H_2}} = 1.07 \cdot 10^{-6}\,\mathrm{mol\,m^{-2}\,s^{-1}}$ through the separator. As this factor has not been considered in the results presented in the prior chapters, a simulation with mixed cycles and identical oversaturation factor is also shown in Fig. 4.12 (left). However, it can be seen that the crossover through the separator is of minor importance when the electrolyzer is operated with mixed cycles as a decrease of the gas purity can hardly be noticed. Thus, an effective molar flux through the separator ($A_\mathrm{sep} = 232\,\mathrm{cm^2}$) of $N_{\mathrm{cross,H_2}} \cdot A_\mathrm{sep}$ has a share of only 9 % of the total hydrogen flux entering the anodic half cell. This is further emphasized

in Fig. 4.12 (right), which shows the comparison of the hydrogen crossover fluxes through electrolyte mixing $\dot{n}_{\mathrm{mix}}$ and diffusion through the separator $\dot{n}_{\mathrm{cross}}$ for electrolyte flow rates from $200\,\mathrm{mL\,min^{-1}}$ to $400\,\mathrm{mL\,min^{-1}}$ and mixed electrolyte cycles. The figure only depicts the diffusional crossover at a flow rate of $200\,\mathrm{mL\,min^{-1}}$ as the simulations showed no significant dependency on flow rate variations. However, it becomes obvious, that the hydrogen crossover flux through electrolyte mixing is strongly influenced by a flow rate increase.

4.5 Summary

In this study a stationary mathematical model for the estimation of the product gas purity in alkaline water electrolysis is presented. The model is based on a classical process engineering approach and permits an estimation of the product gas concentrations as a function of the current density, electrolyte flow rate, concentration, temperature and cycling strategy. Thus, the model can be applied for the estimation of the lower operation limit. The model is validated and parametrized with experimental data, which was achieved in a lab-scale electrolyzer equipped with a $150\,\mathrm{cm^2}$ zero-gap cell and a Zirfon$^{\mathrm{TM}}$ UTP 500 Perl separator. The measuring and modelling results suggest an improvement of the gas purity through a reduction of the electrolyte flow rate, an increase of the electrolyte temperature and an increase of the electrolyte concentration. Moreover, a further reduction of the foreign gas content can be achieved through separation of the electrolyte cycles. For a precise prediction of the measurement data the solubility model is of special importance as could be demonstrated with a sensitivity analysis. However, the model predicts lower gas impurities than experimentally determined in separated mode, because the concentration gradient across the separator is underestimated due to the assumption of a CSTR. Therefore, an oversaturation factor has been implemented into the model, which then leads to similar results as in the experiment. To overcome this disadvantage the further model development should be concentrated on the integration of locally distributed material balances, which would enable the calculation of the dissolved concentration profiles in the electrode boundary layer. Thus, a direct estimation of the supersaturated electrolyte concentration in the vicinity of the separator would be possible. Furthermore, the model development should be focused on the integration of dynamic mass balances,

which would enable the investigation of dynamic cycling strategies and the connection to a downstream hydrogen processing unit.

Acknowledgements

This research did not receive any specific grant from funding agencies in the public, commercial, or not-for-profit sectors.

Appendix

– Dynamic viscosity of aqueous KOH solution (30 wt% KOH [73]):

$$\frac{\eta_\mathrm{L}}{\mathrm{Pa\,s}} = \sum_{n=0}^{4} \eta_{\mathrm{L},n} \cdot \left(\frac{T}{\mathrm{K}}\right)^n$$

$\eta_{\mathrm{L},0}$	0.9105535967
$\eta_{\mathrm{L},1}$	-0.01062211683
$\eta_{\mathrm{L},2}$	$4.680761561 \cdot 10^{-5}$
$\eta_{\mathrm{L},3}$	$-9.209312883 \cdot 10^{-8}$
$\eta_{\mathrm{L},4}$	$6.814919843 \cdot 10^{-11}$

Validity: $T = 273.15\,\mathrm{K} - 363.15\,\mathrm{K}$

– Density of pure H_2O [77]:

$$\frac{\rho_{\mathrm{H_2O}}}{\mathrm{kg\,m^{-3}}} = \left(\sum_{n=0}^{5} \rho_{\mathrm{H_2O},n} \cdot \left(\frac{\vartheta}{^\circ\mathrm{C}}\right)^n\right) \cdot \left(1 + 16.879850 \cdot 10^{-3} \cdot \left(\frac{\vartheta}{^\circ\mathrm{C}}\right)\right)^{-1}$$

$\rho_{\mathrm{H_2O},0}$	999.83952
$\rho_{\mathrm{H_2O},1}$	16.945176
$\rho_{\mathrm{H_2O},2}$	$-7.9870401 \cdot 10^{-3}$
$\rho_{\mathrm{H_2O},3}$	$-46.170461 \cdot 10^{-6}$
$\rho_{\mathrm{H_2O},4}$	$105.56302 \cdot 10^{-9}$
$\rho_{\mathrm{H_2O},5}$	$-280.54253 \cdot 10^{-12}$

Validity: $\vartheta = 0.01\,^\circ\mathrm{C} - 150\,^\circ\mathrm{C}$

– Density of aqueous KOH solution [76]:

$$\frac{\rho_\mathrm{L}}{\mathrm{kg\,m^{-3}}} = \left(\sum_{n=0}^{4} \rho_{\mathrm{L},n} \cdot \left(\frac{\vartheta}{^\circ\mathrm{C}}\right)^n\right) \cdot \exp\left(0.86 \cdot w_\mathrm{KOH}\right)$$

$\rho_{\mathrm{L},0}$	1001.53053
$\rho_{\mathrm{L},1}$	-0.08343
$\rho_{\mathrm{L},2}$	-0.00401
$\rho_{\mathrm{L},3}$	$5.51232 \cdot 10^{-6}$
$\rho_{\mathrm{L},4}$	$-8.20994 \cdot 10^{-10}$

Validity: $\vartheta = 0.01\,^\circ\mathrm{C} - 200\,^\circ\mathrm{C}$; $w_\mathrm{KOH} = 0 - 0.5$

– Binary diffusion coefficients of H_2 and O_2 in aqueous KOH solution [61]:

$$\frac{D_{\mathrm{H_2,KOH}}}{\mathrm{m^2\,s^{-1}}} = \sum_{n=0}^{2} D_{\mathrm{H_2,KOH},n} \cdot (w_\mathrm{KOH})^n$$

$$\frac{D_{\mathrm{O_2,KOH}}}{\mathrm{m^2\,s^{-1}}} = \sum_{n=0}^{3} D_{\mathrm{O_2,KOH},n} \cdot (w_\mathrm{KOH})^n$$

	H_2 - 80 °C	H_2 - 60 °C
$D_{i,\mathrm{H_2,KOH},0}$	$1.14983 \cdot 10^{-8}$	$8.04542 \cdot 10^{-9}$
$D_{i,\mathrm{H_2,KOH},1}$	$-2.67273 \cdot 10^{-8}$	$-2.07309 \cdot 10^{-8}$
$D_{i,\mathrm{H_2,KOH},2}$	$2.34582 \cdot 10^{-8}$	$2.02214 \cdot 10^{-8}$
	O_2 - 80 °C	O_2 - 60 °C
$D_{\mathrm{O_2,KOH},0}$	$6.09167 \cdot 10^{-9}$	$4.27612 \cdot 10^{-9}$
$D_{\mathrm{O_2,KOH},1}$	$-2.40451 \cdot 10^{-8}$	$-1.90911 \cdot 10^{-8}$
$D_{\mathrm{O_2,KOH},2}$	$3.90584 \cdot 10^{-8}$	$3.6684 \cdot 10^{-8}$
$D_{\mathrm{O_2,KOH},3}$	$-2.15785 \cdot 10^{-8}$	$-2.53386 \cdot 10^{-8}$

Validity: H_2 - $w_\mathrm{KOH} = 0.20 - 0.47$; O_2 - $w_\mathrm{KOH} = 0.10 - 0.47$

– Surface tension of aqueous KOH solution [38]:

$$\frac{\gamma}{\mathrm{N\,m^{-1}}} = \sum_{n=0}^{3} \gamma_n \cdot (w_{\mathrm{KOH}})^n$$

	80 °C	70 °C	60 °C	50 °C
γ_0	0.06291173	0.06420781	0.06588789	0.06741636
γ_1	0.01621055	0.02568782	0.02454658	0.02291793
γ_2	0.1778083	0.1319524	0.1283735	0.1352026
γ_3	−0.1017403	−0.04673823	−0.0330648	−0.03852598

Validity: $w_{\mathrm{KOH}} = 0.01 - 0.58$

– Henry coefficients of H_2 and O_2 in H_2O [47]:

$$A\left(\log \overline{H}_i\right)^2 + B\left(1/\overline{T}\right)^2 + C\left(\log \overline{H}_i\right)\left(1/\overline{T}\right) + D\left(\log \overline{H}_i\right) + E\left(1/\overline{T}\right) - 1 = 0$$

with $\overline{H}_i = (H_i/\mathrm{atm}) \cdot 10^{-4}$ and $1/\overline{T} = (1/T/\mathrm{K}) \cdot 10^3$

Gas	A	B	C	D	E
H_2	−0.1233	−0.1366	0.02155	−0.2368	0.8249
O_2	−0.0005943	−0.1470	−0.05120	−0.1076	0.8447

Validity: $T = 273\,\mathrm{K} - 353\,\mathrm{K}$

– H_2 and O_2 solubility in aqueous KOH solution:

$$\log\left(\frac{c^*_{i,\mathrm{H_2O}}}{c^*_i}\right) = K_i \cdot w_{\mathrm{KOH}}$$

$$K_{\mathrm{H_2}} = 3.14,\ K_{\mathrm{O_2}} = 3.66$$

The Setchenov constant K_i is estimated from experimental solubility data in 5.4 wt% - 39.8 wt% KOH by Knaster and Apel'baum [49] at a temperature of 75 °C.

– Equilibrium water vapor pressure above aqueous KOH solution [40]:

$$\begin{aligned}\log\frac{p_{\mathrm{H_2O}}}{\mathrm{bar}} = &-0.01508\frac{m_{\mathrm{KOH}}}{\mathrm{mol\,kg^{-1}}} - 0.0016788\left(\frac{m_{\mathrm{KOH}}}{\mathrm{mol\,kg^{-1}}}\right)^2 \\ &+ 2.25887\cdot10^{-5}\left(\frac{m_{\mathrm{KOH}}}{\mathrm{mol\,kg^{-1}}}\right)^3 + \left(1 - 0.0012062\frac{m_{\mathrm{KOH}}}{\mathrm{mol\,kg^{-1}}}\right. \\ &\left.+ 5.6024\cdot10^{-4}\left(\frac{m_{\mathrm{KOH}}}{\mathrm{mol\,kg^{-1}}}\right)^2 - 7.8228\cdot10^{-6}\left(\frac{m_{\mathrm{KOH}}}{\mathrm{mol\,kg^{-1}}}\right)^3\right) \\ &\cdot\left(35.4462 - \frac{3343.93}{\frac{T}{\mathrm{K}}} - 10.9\log\frac{T}{\mathrm{K}} + 0.0041645\frac{T}{\mathrm{K}}\right)\end{aligned}$$

Validity: $m_{\mathrm{KOH}} = 0\,\mathrm{mol\,kg^{-1}} - 18\,\mathrm{mol\,kg^{-1}}$, $T = 273.15\,\mathrm{K} - 573.15\,\mathrm{K}$

– Conversion of molality and mass fraction of aqueous KOH solution:

$$m_{\mathrm{KOH}} = \frac{w_{\mathrm{KOH}}}{M_{\mathrm{KOH}}\,(1 - w_{\mathrm{KOH}})}$$

Nomenclature

A_{el}	geometrical electrode area	$\mathrm{m^2}$
A_{GL}^{j}	gas-liquid interfacial area in compartment j	$\mathrm{m^2}$
A_{sep}	separator area	$\mathrm{m^2}$
c_i^{mix}	mixer outlet concentration of component i	$\mathrm{mol\,m^{-3}}$
$c_{\mathrm{in},i}^{j}$	inlet concentration of component i in compartment j	$\mathrm{mol\,m^{-3}}$
$c_{\mathrm{out},i}^{j}$	outlet concentration of component i in compartment j	$\mathrm{mol\,m^{-3}}$
$c_i^{*,j}$	equilibrium concentration of component i in compartment j	$\mathrm{mol\,m^{-3}}$
d_{b}^{j}	gas bubble diameter in compartment j	m
d_{sep}	separator thickness	m
$D_{i,k}$	binary diffusion coefficient of component i in electrolyte solution k	$\mathrm{m^2\,s^{-1}}$
$D_{i,k}^{\mathrm{eff}}$	effective diffusion coefficient of component i in the separator	$\mathrm{m^2\,s^{-1}}$
E^0	standard electrode potential	V
F	Faraday constant, 96485	$\mathrm{C\,mol^{-1}}$
$f_{\mathrm{G},i}$	gas evolution efficiency of component i	1
g	gravity, 9.81	$\mathrm{m\,s^{-2}}$
H_i	Henry coefficient of component i	atm

J	current density	$\mathrm{A\,m^{-2}}$
$k^j_{\mathrm{L},i}$	mass transfer coefficient of component i in compartment j	$\mathrm{m\,s^{-1}}$
M_{KOH}	molar mass of potassium hydroxide, 0.0561056	$\mathrm{kg\,mol^{-1}}$
m_{KOH}	molality of potassium hydroxide solution	$\mathrm{mol\,kg^{-1}}$
$N_{\mathrm{cross},i}$	flux density through the separator of component i	$\mathrm{mol\,m^{-2}\,s^{-1}}$
$N^j_{\mathrm{phys},i}$	de- or absorption flux density of component i in compartment j	$\mathrm{mol\,m^{-2}\,s^{-1}}$
$\dot{n}^j_{\mathrm{R},i}$	molar reaction flow rate of component i in compartment j	$\mathrm{mol\,s^{-1}}$
p^0	applied system pressure	Pa
p^j	absolute pressure in compartment j	Pa
$p_{\mathrm{H_2O}}$	partial pressure of water	Pa
$p^j_{\mathrm{in},i}$	inlet partial pressure of component i in compartment j	Pa
$p^j_{\mathrm{out},i}$	outlet partial pressure of component i in compartment j	Pa
R	universal gas constant, 8.314	$\mathrm{J\,mol^{-1}\,K^{-1}}$
Re^j	Reynolds number in compartment j	1
S^j_{b}	single gas bubble surface area in compartment j	$\mathrm{m^2}$
Sc_i	Schmidt number of component i	1
Sh^j_i	Sherwood number of component i in compartment j	1
T	temperature	K
u^j_{b}	single bubble rise velocity in compartment j	$\mathrm{m\,s^{-1}}$
u^j_{sw}	bubble swarm rise velocity in compartment j	$\mathrm{m\,s^{-1}}$
V^j_{b}	single gas bubble volume in compartment j	$\mathrm{m^3}$
V^j_{gas}	total gas volume in compartment j	$\mathrm{m^3}$
V_{hcell}	total half cell volume, $3.48 \cdot 10^{-4}$	$\mathrm{m^3}$
$\dot{V}^j_{\mathrm{G}}$	volumetric gas flow rate in compartment j	$\mathrm{m^3\,s^{-1}}$
$\dot{V}^j_{\mathrm{L}}$	volumetric liquid electrolyte flow rate in compartment j	$\mathrm{m^3\,s^{-1}}$
$\dot{V}^{\mathrm{mix}}_{\mathrm{L}}$	outlet volumetric liquid electrolyte flow rate of mixer	$\mathrm{m^3\,s^{-1}}$
w_{KOH}	mass fraction of potassium hydroxide in electrolyte solution	1
$x^j_{\mathrm{out},i}$	outlet mole fraction of component i in compartment j	1
z	number of transferred electrons in electrode reaction	1
β^j	contact angle of gas-solid interface in compartment j	1
γ	surface tension	$\mathrm{N\,m^{-1}}$

ε	porosity	1
$\varepsilon_{\mathrm{g}}^{j}$	gas voidage in compartment j	1
$\varepsilon_{\mathrm{g,out}}^{j}$	outlet gas voidage in compartment j	1
η_{L}	electrolyte viscosity	$\mathrm{Pa\,s}$
ϑ	temperature	°C
κ_{L}	electrical conductivity of electrolyte solution	$\mathrm{S\,m^{-1}}$
ν_i^j	stoichiometric coefficient of component i in compartment j	1
ρ_{G}^{j}	gaseous density in compartment j	$\mathrm{kg\,m^{-3}}$
ρ_{L}	electrolyte density	$\mathrm{kg\,m^{-3}}$
τ	tortuosity	1

Abbrevations

ano	anode
cat	cathode
CFD	computational fluid dynamics
CSTR	continuous stirred-tank reactor
DC	direct current
PEM	proton exchange membrane/polymer exchange membrane

References

[1] D. Parra, M. K. Patel. Techno-economic implications of the electrolyser technology and size for power-to-gas systems. *Int J Hydrogen Energ*, 41(6):3748–3761, 2016. DOI: 10.1016/j.ijhydene.2015.12.160.

[2] D. Ipsakis, S. Voutetakis, P. Seferlis, F. Stergiopoulos, C. Elmasides. Power management strategies for a stand-alone power system using renewable energy sources and hydrogen storage. *Int J Hydrogen Energ*, 34(16):7081–7095, 2009. DOI: 10.1016/j.ijhydene.2008.06.051.

[3] F. Díaz-González, A. Sumper, O. Gomis-Bellmunt, R. Villafáfila-Robles. A review of energy storage technologies for wind power applications. *Renew Sust Energ Rev*, 16(4):2154–2171, 2012. DOI: 10.1016/j.rser.2012.01.029.

[4] M. Ludwig, C. Haberstroh, U. Hesse. Exergy and cost analyses of hydrogen-based energy storage pathways for residual load management. *Int J Hydrogen Energ*, 40 (35):11348–11355, 2015. DOI: 10.1016/j.ijhydene.2015.03.018.

[5] G. Gahleitner. Hydrogen from renewable electricity: An international review of power-to-gas pilot plants for stationary applications. *Int J Hydrogen Energ*, 38(5): 2039–2061, 2013. DOI: 10.1016/j.ijhydene.2012.12.010.

[6] A. Ursúa, E. L. Barrios, J. Pascual, I. San Martín, P. Sanchis. Integration of commercial alkaline water electrolysers with renewable energies: Limitations and improvements. *Int J Hydrogen Energ*, 41(30):12852–12861, 2016. DOI: 10.1016/j.ijhydene.2016.06.071.

[7] B. Bensmann, R. Hanke-Rauschenbach, G. Müller-Syring, M. Henel, K. Sundmacher. Optimal configuration and pressure levels of electrolyzer plants in context of power-to-gas applications. *Appl Energ*, 167:107–124, 2016. DOI: 10.1016/j.apenergy.2016.01.038.

[8] M. Momirlan, T. N. Veziroglu. The properties of hydrogen as fuel tomorrow in sustainable energy system for a cleaner planet. *Int J Hydrogen Energ*, 30(7):795–802, 2005. DOI: 10.1016/j.ijhydene.2004.10.011.

[9] M. Götz, J. Lefebvre, F. Mörs, A. McDaniel Koch, F. Graf, S. Bajohr, R. Reimert, T. Kolb. Renewable power-to-gas: A technological and economic review. *Renew Energ*, 85:1371–1390, 2016. DOI: 10.1016/j.renene.2015.07.066.

[10] R. L. LeRoy. Industrial water electrolysis: Present and future. *Int J Hydrogen Energ*, 8(6):401–417, 1983. DOI: 10.1016/0360-3199(83)90162-3.

[11] M. Carmo, D. L. Fritz, J. Mergel, D. Stolten. A comprehensive review on PEM water electrolysis. *Int J Hydrogen Energ*, 38(12):4901–4934, 2013. DOI: 10.1016/j.ijhydene.2013.01.151.

[12] S. G. Bratsch. Standard electrode potentials and temperature coefficients in water at 298.15 K. *J Phys Chem Ref Data*, 18(1):1–21, 1989. DOI: 10.1063/1.555839.

[13] A. Ursúa, I. San Martín, E. L. Barrios, P. Sanchis. Stand-alone operation of an alkaline water electrolyser fed by wind and photovoltaic systems. *Int J Hydrogen Energ*, 38(35):14952–14967, 2013. DOI: 10.1016/j.ijhydene.2013.09.085.

[14] G. Tjarks, J. Mergel, D. Stolten. *Dynamic Operation of Electrolyzers – Systems Design and Operating Strategies*. Hydrogen Science and Engineering: Materials, Processes, Systems and Technology. Wiley-VCH, Weinheim, 2016. DOI: 10.1002/9783527674268.ch14.

[15] M. Schalenbach, M. Carmo, D. L. Fritz, J. Mergel, D. Stolten. Pressurized PEM water electrolysis: Efficiency and gas crossover. *Int J Hydrogen Energ*, 38(35):14921–14933, 2013. DOI: 10.1016/j.ijhydene.2013.09.013.

[16] V. Schroeder, B. Emonts, H. Janssen, H.-P. Schulze. Explosion limits of hydrogen/oxygen mixtures at initial pressures up to 200 bar. *Chem Eng Technol*, 27(8):847–851, 2004. DOI: 10.1002/ceat.200403174.

[17] W. Hug, J. Divisek, J. Mergel, W. Seeger, H. Steeb. Highly efficient advanced alkaline electrolyzer for solar operation. *Int J Hydrogen Energ*, 17(9):699–705, 1992. DOI: 10.1016/0360-3199(92)90090-J.

[18] Ø. Ulleberg. Modeling of advanced alkaline electrolyzers: A system simulation approach. *Int J Hydrogen Energ*, 28(1):21–33, 2003. DOI: 10.1016/s0360-3199(02)00033-2.

[19] L. M. Gandia, R. Oroz, A. Ursua, P. Sanchis, P. M. Dieguez. Renewable hydrogen production: Performance of an alkaline water electrolyzer working under emulated wind conditions. *Energ Fuel*, 21(3):1699–1706, 2007. DOI: 10.1021/ef060491u.

[20] E. Amores, J. Rodríguez, C. Carreras. Influence of operation parameters in the modeling of alkaline water electrolyzers for hydrogen production. *Int J Hydrogen Energ*, 39(25):13063–13078, 2014. DOI: 10.1016/j.ijhydene.2014.07.001.

[21] M. Hammoudi, C. Henao, K. Agbossou, Y. Dubé, M. L. Doumbia. New multi-physics approach for modelling and design of alkaline electrolyzers. *Int J Hydrogen Energ*, 37(19):13895–13913, 2012. DOI: 10.1016/j.ijhydene.2012.07.015.

[22] C. Henao, K. Agbossou, M. Hammoudi, Y. Dubé, A. Cardenas. Simulation tool based on a physics model and an electrical analogy for an alkaline electrolyser. *J Power Sources*, 250:58–67, 2014. DOI: 10.1016/j.jpowsour.2013.10.086.

[23] J. Milewski, G. Guandalini, S. Campanari. Modeling an alkaline electrolysis cell through reduced-order and loss-estimate approaches. *J Power Sources*, 269:203–211, 2014. DOI: 10.1016/j.jpowsour.2014.06.138.

[24] L. Abdelouahed, R. Hreiz, S. Poncin, G. Valentin, F. Lapicque. Hydrodynamics of gas bubbles in the gap of lantern blade electrodes without forced flow of electrolyte: Experiments and CFD modelling. *Chem Eng Sci*, 111:255–265, 2014. DOI: 10.1016/j.ces.2014.01.028.

[25] J. Schillings, O. Doche, J. Deseure. Modeling of electrochemically generated bubbly flow under buoyancy-driven and forced convection. *Int J Heat Mass Tran*, 85:292–299, 2015. DOI: 10.1016/j.ijheatmasstransfer.2015.01.121.

[26] M. Schalenbach, G. Tjarks, M. Carmo, W. Lueke, M. Mueller, D. Stolten. Acidic or alkaline? Towards a new perspective on the efficiency of water electrolysis. *J Electrochem Soc*, 163(11):3197–3208, 2016. DOI: 10.1149/2.0271611jes.

[27] M. Schalenbach, W. Lueke, D. Stolten. Hydrogen diffusivity and electrolyte permeability of the Zirfon PERL separator for alkaline water electrolysis. *J Electrochem Soc*, 163(14):1480–1488, 2016. DOI: 10.1149/2.1251613jes.

[28] O. Levenspiel. *Chemical Reaction Engineering*. Wiley-India, New Delhi, 2012.

[29] H. Vogt. The role of single-phase free convection in mass transfer at gas evolving electrodes - I. Theoretical. *Electrochim Acta*, 38(10):1421–1426, 1993. DOI: 10.1016/0013-4686(93)80079-F.

[30] H. Vogt, G. Kreysa, S. Vasudevan, R. Wüthrich, J. D. Abou Ziki, R. El-Haddad. *Electrochemical Reactors*. Ullmann's Encyclopedia of Industrial Chemistry. Wiley-VCH, Weinheim, 2013. DOI: 10.1002/14356007.l09_l01.pub2.

[31] R. Hreiz, L. Abdelouahed, D. Fünfschilling, F. Lapicque. Electrogenerated bubbles induced convection in narrow vertical cells: PIV measurements and Euler–Lagrange CFD simulation. *Chem Eng Sci*, 134:138–152, 2015. DOI: 10.1016/j.ces.2015.04.041.

[32] J. Eigeldinger, H. Vogt. The bubble coverage of gas-evolving electrodes in a flowing electrolyte. *Electrochim Acta*, 45(27):4449–4456, 2000. DOI: 10.1016/S0013-4686(00)00513-2.

[33] R. J. Balzer, H. Vogt. Effect of electrolyte flow on the bubble coverage of vertical gas-evolving electrodes. *J Electrochem Soc*, 150(1):11–16, 2003. DOI: 10.1149/1.1524185.

[34] H. Vogt. The rate of gas evolution of electrodes - I. An estimate of the efficiency of gas evolution from the supersaturation of electrolyte adjacent to a gas-evolving electrode. *Electrochim Acta*, 29(2):167–173, 1984. DOI: 10.1016/0013-4686(84)87043-7.

[35] H. Vogt. The rate of gas evolution at electrodes - II. An estimate of the efficiency of gas evolution on the basis of bubble growth data. *Electrochim Acta*, 29(2):175–180, 1984. DOI: 10.1016/0013-4686(84)87044-9.

[36] K. Kikuchi, S. Nagata, Y. Tanaka, Y. Saihara, Z. Ogumi. Characteristics of hydrogen nanobubbles in solutions obtained with water electrolysis. *J Electroanal Chem*, 600(2):303–310, 2007. DOI: 10.1016/j.jelechem.2006.10.005.

[37] P. Atkins, J. de Paula. *Atkins' Physical Chemistry - 8th Edition*. Oxford University Press, Oxford, 2006.

[38] K. Feldkamp. Die Oberflächenspannung wässriger NaOH- und KOH-Lösungen. *Chem Ing Tech*, 41(21):1181–1183, 1969. DOI: 10.1002/cite.330412107.

[39] R. L. LeRoy, C. T. Bowen, D. J. LeRoy. The thermodynamics of aqueous water electrolysis. *J Electrochem Soc*, 127(9):1954–1962, 1980. DOI: 10.1149/1.2130044.

[40] J. Balej. Water vapour partial pressures and water activities in potassium and sodium hydroxide solutions over wide concentration and temperature ranges. *Int J Hydrogen Energ*, 10(4):233–243, 1985. DOI: 10.1016/0360-3199(85)90093-X.

[41] H. Vogt. On the gas-evolution efficiency of electrodes I - Theoretical. *Electrochim Acta*, 56(3):1409–1416, 2011. DOI: 10.1016/j.electacta.2010.08.101.

[42] C. A. C. Sequeira, D. M. F. Santos, B. Šljukić, L. Amaral. Physics of electrolytic gas evolution. *Braz J Phys*, 43(3):199–208, 2013. DOI: 10.1007/s13538-013-0131-4.

[43] H. Vogt. Studies on gas-evolving electrodes: The concentration of dissolved gas in electrolyte bulk. *Electrochim Acta*, 30(2):265–270, 1985. DOI: 10.1016/0013-4686(85)80092-X.

[44] J. St-Pierre, N. Massé, M. Bergeron. Dissolved oxygen concentration in a divided rotating cylinder electrode reactor. *Electrochim Acta*, 40(8):1013–1024, 1995. DOI: 10.1016/0013-4686(94)00337-Z.

[45] J. M. Chin Kwie Joe, L. J. J. Janssen, S. J. D. van Strelen, J. H. G. Verbunt, W. M. Sluyter. Bubble parameters and efficiency of gas bubble evolution for a chlorine-, a hydrogen- and an oxygen-evolving wire electrode. *Electrochim Acta*, 33(6):769–779, 1988. DOI: 10.1016/S0013-4686(98)80006-6.

[46] J. A. Wesselingh, R. Krishna. *Mass Transfer in Multicomponent Mixtures*. VSSD, Delft, 2006.

[47] D. M. Himmelblau. Solubilities of inert gases in water. 0 °C to near the critical point of water. *J Chem Eng Data*, 5(1):10–15, 1960. DOI: 10.1021/je60005a003.

[48] S. Weisenberger, A. Schumpe. Estimation of gas solubilites in salt solutions at temperatures from 273 K to 363 K. *AIChE J*, 42(1):298–300, 1996. DOI: 10.1002/aic.690420130.

[49] M. B. Knaster, L. A. Apel'baum. Solubility of hydrogen and oxygen in concentrated potassium hydroxide solution. *Russ J Phys Ch*, 38:120–122, 1964.

[50] H. Brauer, D. Mewes. Strömungswiderstand sowie stationärer Stoff- und Wärmeübergang an Blasen und Tropfen. *Chem Ing Tech*, 44(15):953–956, 1972. DOI: 10.1002/cite.330441513.

[51] F. N. Peebles, H. J. Garber. Studies on the motion of gas bubbles in liquids. *Chem Eng Prog*, 49(2):88–97, 1953.

[52] P. Grassmann. *Physikalische Grundlagen der Verfahrenstechnik*. Sauerländer, Frankfurt/Main, 1970.

[53] V. Kienzlen. *Potentialverteilung an gasentwickelnden Elektroden*. Institut für Technische Thermodynamik, DLR Forschungsbericht, 1992.

[54] G. Kreysa, M. Kuhn. Modelling of gas evolving electrolysis cells. I. The gas voidage problem. *J Appl Electrochem*, 15(4):517–526, 1985. DOI: 10.1007/BF01059293.

[55] H. Brauer, H. Thiele. Bewegung von Partikelschwärmen. *Chem Ing Tech*, 45(13): 909–912, 1973. DOI: 10.1002/cite.330451317.

[56] N. Guillet, P. Millet. *Alkaline Water Electrolysis.* Hydrogen Production by Electrolysis. Wiley-VCH, Weinheim, 2015. DOI: 10.1002/9783527676507.ch4.

[57] F. Marangio, M. Santarelli, M. Cali. Theoretical model and experimental analysis of a high pressure PEM electrolyser for hydrogen production. *Int J Hydrogen Energ*, 34(3):1143–1158, 2009. DOI: 10.1016/j.ijhydene.2008.11.083.

[58] S. A. Grigoriev, V. I. Porembskiy, S. V. Korobtsev, V. N. Fateev, F. Auprête, P. Millet. High-pressure PEM water electrolysis and corresponding safety issues. *Int J Hydrogen Energ*, 36(3):2721–2728, 2011. DOI: 10.1016/j.ijhydene.2010.03.058.

[59] H. Kim, M. Park, K. S. Lee. One-dimensional dynamic modeling of a high-pressure water electrolysis system for hydrogen production. *Int J Hydrogen Energ*, 38(6): 2596–2609, 2013. DOI: 10.1016/j.ijhydene.2012.12.006.

[60] P. Trinke, B. Bensmann, S. Reichstein, R. Hanke-Rauschenbach, K. Sundmacher. Hydrogen permeation in PEM electrolyzer cells operated at asymmetric pressure conditions. *J Electrochem Soc*, 163(11):3164–3170, 2016. DOI: 10.1149/2.0221611jes.

[61] M. K. Tham, R. D. Walker, K. E. Gubbins. Diffusion of oxygen and hydrogen in aqueous potassium hydroxide solutions. *J Phys Chem*, 74(8):1747–1751, 1970. DOI: 10.1021/j100703a015.

[62] Brochure Zirfon Perl UTP 500. `https://www.agfa.com/sp/global/en/binaries/ZirfonPerl_UTP500_tcm611-56748.pdf`. Accessed: 29 September 2016.

[63] H. Vogt. Mechanisms of mass transfer of dissolved gas from a gas-evolving electrode and their effect on mass transfer coefficient and concentration overpotential. *J Appl Electrochem*, 19(5):713–719, 1989. DOI: 10.1007/BF01320646.

[64] P. Haug, M. Koj, T. Turek. Influence of process conditions on gas purity in alkaline water electrolysis. *Int J Hydrogen Energ*, 42(15):9406–9418, 2017. DOI: 10.1016/j.ijhydene.2016.12.111.

[65] C. A. Schug. Operational characteristics of high-pressure, high-efficiency water-hydrogen-electrolysis. *Int J Hydrogen Energ*, 23(12):1113–1120, 1998. DOI: 10.1016/S0360-3199(97)00139-0.

[66] H. Vogt, R. J. Balzer. The bubble coverage of gas-evolving electrodes in stagnant electrolytes. *Electrochim Acta*, 50(10):2073–2079, 2005. DOI: 10.1016/j.electacta.2004.09.025.

[67] J. Venczel. Über Gasblasen bei elektrochemischen Prozessen. *Electrochim Acta*, 15 (12):1909–1920, 1970. DOI: 10.1016/0013-4686(70)85028-9.

[68] L. J. J. Janssen, J. G. Hoogland. The effect of electrolytically evolved gas bubbles on the thickness of the diffusion layer - II. *Electrochim Acta*, 18(8):543–550, 1973. DOI: 10.1016/0013-4686(73)85016-9.

[69] D. Landolt, R. Acosta, R. H. Muller, C. W. Tobias. An optical study of cathodic hydrogen evolution in high-rate electrolysis. *J Electrochem Soc*, 117(6):839–845, 1970. DOI: 10.1149/1.2407646.

[70] N. Ibl, E. Adam, J. Venczel, E. Schalch. Stofftransport bei der Elektrolyse mit Gasrührung. *Chem Ing Tech*, 43(4):202–215, 1971. DOI: 10.1002/cite.330430418.

[71] L. J. J. Janssen, C. W. M. P. Sillen, E. Barendrecht, S. J. D. van Stralen. Bubble behaviour during oxygen and hydrogen evolution at transparent electrodes in KOH solution. *Electrochim Acta*, 29(5):633–642, 1984. DOI: 10.1016/0013-4686(84)87122-4.

[72] L. Sigrist, O. Dossenbach, N. Ibl. On the conductivity and void fraction of gas dispersions in electrolyte solutions. *J Appl Electrochem*, 10(2):223–228, 1980. DOI: 10.1007/BF00726089.

[73] Olin Chlor Alkali Products - KOH Viscosity. `https://koh.olinchloralkali.com/TechnicalInformation/KOH%20Viscosity.pdf`. Accessed: 09 February 2017.

[74] D. Tromans. Oxygen solubility modeling in inorganic solutions: Concentration, temperature and pressure effects. *Hydrometallurgy*, 50(3):279–296, 1998. DOI: 10.1016/S0304-386X(98)00060-7.

[75] A. Schumpe. The estimation of gas solubilities in salt solutions. *Chem Eng Sci*, 48 (1):153–158, 1993. DOI: 10.1016/0009-2509(93)80291-W.

[76] R. Gilliam, J. Graydon, D. Kirk, S. Thorpe. A review of specific conductivities of potassium hydroxide solutions for various concentrations and temperatures. *Int J Hydrogen Energ*, 32(3):359–364, 2007. DOI: 10.1016/j.ijhydene.2006.10.062.

[77] G. S. Kell. Density, thermal expansivity, and compressibility of liquid water from 0 °C to 150 °C: Correlations and tables for atmospheric pressure and saturation reviewed and expressed on 1968 temperature scale. *J Chem Eng Data*, 20(1):97–105, 1975. DOI: 10.1021/je60064a005.

5 Hydrogen crossover in PEM and alkaline water electrolysis: Mechanisms, direct comparison and mitigation strategies

P. Trinke, P. Haug, J. Brauns, B. Bensmann, R. Hanke-Rauschenbach, T. Turek
J Electrochem Soc **2018**, *165 (7)*, F502-F513
https://doi.org/10.1149/2.0541807jes

Abstract

This study provides a direct comparison of hydrogen crossover in PEM (Nafion 117) and alkaline water electrolysis (Zirfon^{TM}) at a temperature of 60 °C applying state-of-the-art separating unit materials. To this end, occurring crossover mechanisms are described first, before experimental data of the anodic hydrogen content are shown in dependence of current density, system pressure and process management strategy. The results suggest that permeation in PEM electrolyzers is mainly governed by diffusion due to a supersaturated concentration of dissolved hydrogen within the catalyst layer, showing a share of 98 % of the total permeation flux at 1 A cm^{-2} and atmospheric pressure. Permeation in alkaline electrolyzers also exhibits a significant influence of supersaturation, but the overall crossover is mainly influenced by mixing the electrolyte cycles, which makes up a share of 90 % at 0.7 A cm^{-2} and 1 bar. Generally it becomes evident that hydrogen permeation

across the separating unit is more than one order of magnitude smaller in alkaline electrolysis, which is mainly a consequence of the significantly lower hydrogen solubility in concentrated KOH electrolyte. Finally, this study concludes with an assessment of the impact of separating unit thickness and provides mitigation strategies to reduce hydrogen crossover.

Keywords: anodic hydrogen content, crossover comparison, water electrolysis

5.1 Introduction

Proton exchange membrane (PEM) and alkaline water electrolysis (AEL) represent two promising technologies, which are capable of the future production of renewable hydrogen. It has already been demonstrated that both technologies can react quickly to dynamic power profiles from renewable energy sources [1, 2]. Generally, both electrolysis technologies are operated in a similar range of parameters to split water into the constituents hydrogen and oxygen (Eq. (5.1)). Thus, temperatures between 50 °C and 80 °C or system pressures up to 30 bar represent the current state of the art [3].

$$\mathrm{H_2O} \longrightarrow \mathrm{H_2} + 0.5\,\mathrm{O_2} \tag{5.1}$$

The main difference between these two technologies lies in the application of either an acid or alkaline electrolyte. In PEM electrolysis protons are used for the charge transport as it is shown in the anodic and cathodic half cell reactions (Eq. (5.2) and (5.3)).

$$\text{Anode:} \quad \mathrm{H_2O} \longrightarrow 2\,\mathrm{H^+} + 0.5\,\mathrm{O_2} + 2\,\mathrm{e^-} \tag{5.2}$$

$$\text{Cathode:} \quad 2\,\mathrm{H^+} + 2\,\mathrm{e^-} \longrightarrow \mathrm{H_2} \tag{5.3}$$

On the contrary, hydroxide ions are responsible for the charge exchange in AEL (Eq. (5.4) and (5.5)).

$$\text{Anode:} \quad 2\,\mathrm{OH^-} \longrightarrow 0.5\,\mathrm{O_2} + \mathrm{H_2O} + 2\,\mathrm{e^-} \tag{5.4}$$

$$\text{Cathode:} \quad 2\,\mathrm{H_2O} + 2\,\mathrm{e^-} \longrightarrow \mathrm{H_2} + 2\,\mathrm{OH^-} \tag{5.5}$$

However, both technologies face similar issues, which need to be solved for a successful coupling with renewable energy sources. Thus, gas crossover represents one of the main issues in PEM and alkaline water electrolysis so far. Especially the permeation of hydrogen

into the anodic half cell is of special importance, as explosive gas mixtures can form in the part-load operation range of the electrolyzers, e.g. [4–7]. However, this problem can be solved relatively easy by the application of recombination catalysts as it has already been demonstrated for PEM electrolysis. Grigoriev et al. [8] showed that the anodic hydrogen content could be significantly reduced using a recombination catalyst, which was applied at the backside of the porous transport layer (PTL). A further improvement of the anodic gas purity could be achieved when the recombination catalyst was placed in the product gas conduits downstream of the gas separators. Another possibility is the utilization of electrocatalysts, which also promote the oxidation of hydrogen and recombination with evolved oxygen to water. Ito et al. [9] reported a decrease of the measured hydrogen fraction if a platinum based reversed catalyst coated membrane (CCM) was used for fuel cell and electrolysis operation. However, it is important to emphasize that recombination catalysts only reduce the risk of safety issues, but do not address the origin of crossover directly. Two further negative side effects of gas crossover, degradation [10, 11] and reduction of Faraday efficiency [8, 12], are still present. However, especially degradation, which has been observed in PEM electrolysis, should not be neglected as the trend towards thinner membranes may further enhance gas crossover. So far, for AEL no publication could be found that establishes a link between gas crossover and electrode degradation, although this dependency also could exist. Nevertheless, the safety problem still represents a major issue in AEL.

Most recent publications on gas crossover in PEM electrolysis are focused on the investigation of the current density influence. It could be shown so far that hydrogen and oxygen crossover increases linearly with the applied current density [5, 13, 14]. The publications on AEL in contrast are mostly focused on the influence of separator and membrane materials, as well as process conditions on the anodic hydrogen fractions. Furthermore, strategies are provided, which may be used for an improved anodic gas purity [7, 15, 16].

The present contribution firstly provides a summary on the occurring crossover mechanisms in PEM and alkaline water electrolysis. Subsequently, experimental data of the influence of current density, system pressure and various process management possibilities on the anodic hydrogen content is shown for both electrolysis technologies. In order to create comparable crossover data, the experiments of both technologies are carried out with state-of-the-art separating unit materials (PEM: Nafion 117, AEL: Zirfon^{TM}) and at

identical process temperatures. The obtained results are then used to identify the most influential crossover mechanism in PEM and alkaline electrolysis. Finally, the study provides an estimation of the influence of separating unit thickness on hydrogen crossover and makes proposals on possible crossover mitigation strategies.

5.2 Experimental setup and method

5.2.1 Cell design

PEM electrolysis

The PEM water electrolysis experiments in this study were conducted with a commercially available electrolysis cell (Sylatech Analysetechnik GmbH, type ZE 200), which is shown in Fig. 5.1 (a). The cell has a circular design with an active area of $62\,\mathrm{cm}^2$ without flow field structures. On the anode side a titanium mesh serves as a water distributor. Between the mesh and the CCM a PTL is incorporated, which consists of sintered titanium fibres. In the cathodic half cell a porous graphite plate is implemented, whereas an O-ring is used for sealing of the electrolysis cell. The CCM is based on a Nafion 117 membrane, which was manufactured by HIAT gGmbH with anode and cathode catalyst loadings of $2\,\mathrm{mg_{Ir}cm^{-2}}$ and $1\,\mathrm{mg_{Pt}cm^{-2}}$, respectively. The dry Nafion membrane has a thickness of approximately $180\,\mu\mathrm{m}$, the porosity amounts to $\varepsilon = 0.37$ (water volume) and the channel diameter is roughly $d = 2.5\,\mathrm{nm}$ [17][1]. The whole cell was encased with thermal insulating fabric for isothermal operating conditions.

Alkaline electrolysis

The AEL experiments were conducted with a custom-built single electrolysis cell, which consists of two end plates, current collectors, electrode mounts, electrodes and a separator for keeping the product gases apart. Fig. 5.1 (b) depicts a choice of these cell components. The end plates are made of nickel coated 304 steel and are used for the electrolyte supply and removal. Additionally, each end plate provides a circular electrolyte volume of roughly $300\,\mathrm{mL}$. The electrolysis voltage can be applied through current collectors out of 316Ti steel, which are connected to the electrode mounts via bolted connections.

[1] porosity and diameter were measured for a Nafion 115 membrane

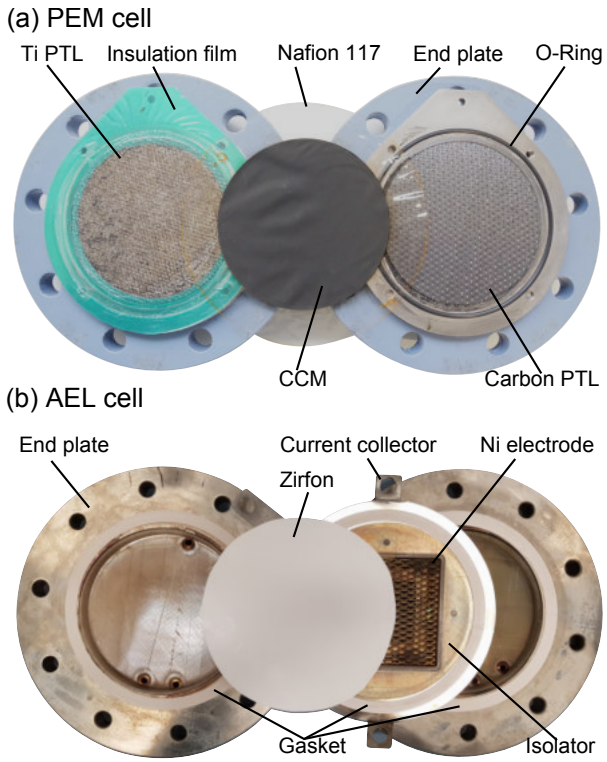

Fig. 5.1: Cell designs of the applied PEM (a) and alkaline (b) electrolysis cells (pictures are not scaled).

The active electrodes themselves consist of quadratic Nickel (Alloy 201) expanded metal with a geometrical area of 100 cm^2 and are welded on the electrode mounts of the same material. These electrodes are directly pressed onto a circular Zirfon$^{\mathrm{TM}}$ Perl UTP 500 separator with a geometrical area of 227 cm^2, so that a zero-gap cell arrangement is achieved. The manufacturer AGFA specifies the separator thickness with $\delta_{\mathrm{sep}} = (500 \pm 50)$ µm, the separator porosity with $\varepsilon = 0.5 \pm 0.1$ and the pore diameter with $d = (150 \pm 50)$ nm [18]. Furthermore the cell contains 3D-printed polypropylene inlays, which are necessary for the electrical insulation of the current collectors from other cell components.

5.2.2 Test station

PEM electrolysis

A Greenlight test station (E100) supplies the anodic compartment of the PEM electrolysis cell with (150 ± 5) mg min^{-1} deionized water at a temperature of 60 °C. The galvanostatic steps are applied by an Ametek Sorensen XG 6-220 power supply with an accuracy of ± 0.2 % of the output current reading. The flow sheet of the test station is shown in

Fig. 5.2 (a). On each side the gas-water mixture is separated by two gas separators and an intermediate cooling step of the gas after the outlet of the first separator. The water of the anode is cycled, whereas on the cathode the separated water is drained.

Pressure control valves regulate the absolute cathodic gas pressure to 1 bar, 10 bar and 20 bar, whereas on the anode side pressures of 1 bar and 10 bar are applied. The error of this regulation is less than ± 0.2 bar. Every three minutes a micro-GC (Agilent 490) takes a gas sample of the anodic product gas to measure the concentration of hydrogen in oxygen. This micro-GC is equipped with a 10 m long 5 Å molesieve column and a thermal conductivity detector for permanent gas separation and detection. Test gas mixtures with hydrogen concentrations of 0.1 vol%, 1 vol% and 2.5 vol% in oxygen (accuracy of reading ± 2 %, Linde) were used for calibration of the GC. The calibration measurements indicated a standard deviation of ± 0.006 vol%. Furthermore, it is possible to directly feed the electrolysis cell with oxygen (Linde 5.0) and hydrogen (Linde 5.0) to the corresponding cell inlet with an accuracy of ± 1 % of the reading. This gas feed is mandatory for reference measurements, which will be described later in this study.

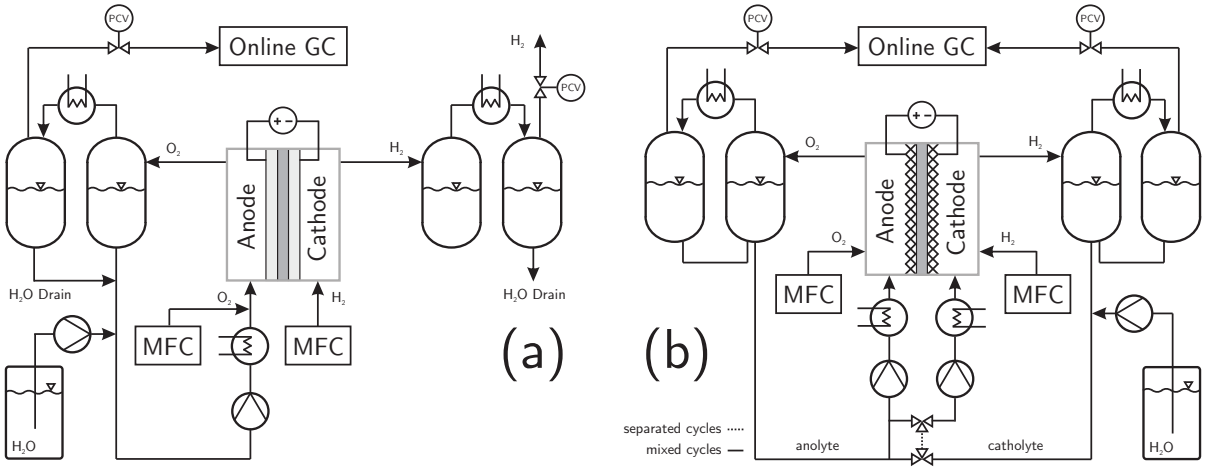

Fig. 5.2: Schematic flow sheets of the PEM (a) and AEL (b) test stations applied in this study.

Alkaline electrolysis

The alkaline test cell was connected to a Greenlight test station (E40), which continuously supplies the anodic and cathodic half cell with a 32 wt% KOH electrolyte solution at a flow rate of (0.350 ± 0.002) L min^{-1}, a temperature of 60 °C and absolute system pressures of 1 bar, 10 bar and 20 bar. Here, both half cell compartments are always operated at

equalized pressure. With the given volumetric flow rate, the electrolyte of each half cell is replaced 70 times per hour, which is defined as the recirculation rate within this work. The electrolysis power is supplied by an Ametek Sorensen XG 12-140 power supply, which is used for galvanostatic measurements with an accuracy of ± 0.2 % of the rated output current.

Downstream of the electrolysis cell the gas-liquid mixtures are fed to gas separators, where the evolved gaseous products are removed from the electrolyte solution. The rising gas flows are then cooled down to approximately 25 °C to reduce the water content of the product gases. The condensed water is collected in a tank and fed back into the gas separators. The remaining gaseous water content is then further reduced by desiccant dryers, before the composition of the product gas streams is analyzed in an online gas chromatograph (Agilent 7820A) every 5 minutes, which is also equipped with a molesieve column and a thermal conductivity detector. Calibration of the GC was carried out with test gas compositions of 0.02 vol%, 0.2 vol% and 1 vol% hydrogen in argon, which could be determined with a maximum error of ± 0.01 vol%. The liquid electrolyte from the gas separators, however, is led back to the mixing point of the electrolyte cycles in order to compensate the concentration difference caused by the electrode reactions (Eqs. (5.4) and (5.5)). Besides the classical electrolyzer operation with mixed electrolyte cycles, this test station also possesses the possibility to separate the cycles by changing the valve position of the 3/2-way valves, which are shown in the flow sheet in Fig. 5.2 (b). It can further be seen in the flow sheet that it is possible to feed the cell via Bronkhorst mass flow controllers with hydrogen (Linde 5.0) to the cathodic and oxygen (Linde 3.5) to the anodic half cell with an accuracy of ± 0.5 % of the desired setpoint.

5.2.3 Methods

In this study the stationary anodic hydrogen contents at a fixed temperature of 60 °C, absolute pressures of 1 bar, 10 bar and 20 bar and various current densities in the range of 0.05 A cm^{-2} to 1 A cm^{-2} were determined by online gas chromatography for PEM and alkaline water electrolysis. In both experimental setups stationary data was achieved in such way that a specific current density was applied to the electrolysis cell and chromatograms were recorded simultaneously. The current density was kept constant until the measured hydrogen fraction remained unchanged for at least 1 h before it was changed

to the next operating point. For determination of the hydrogen content with separated electrolyte cycles in AEL, the cycles were remixed after each operating point to account for the arisen electrolyte concentration difference.

Similarly experiments were carried out in which the PEM and alkaline electrolysis cells were disconnected from the power supply, but fed with hydrogen and oxygen according to their volumetric flow rates representing a current density range from $0.05\,\mathrm{A\,cm^{-2}}$ to $0.9\,\mathrm{A\,cm^{-2}}$. In the following these experiments are referred to as reference measurements, which have only been conducted at atmospheric pressure and 60 °C.

With the experimental data from the electrolysis and reference measurements it is possible to derive the hydrogen permeation rate through the membrane or separator while presuming that the anodic catalyst materials are inactive for the oxidation of hydrogen. Thus, all the permeating hydrogen can be measured in the anodic product gas stream. For the AEL this is only valid for experiments with separated electrolyte cycles. Additionally, it has to be assumed that the oxygen permeation rate is negligibly small compared to the evolution rate of oxygen. This assumption can be made for PEM electrolysis as the oxygen permeation through a Nafion membrane is reported to be least two times smaller than its hydrogen counterpart [19]. For AEL this assumption is also admissible as the hydrogen diffusion coefficient in 32 wt% KOH at 60 °C is about three times larger than that of oxygen [20]. The measured water-free anodic hydrogen fraction $\Phi_{\mathrm{H_2}}$ can then be described according to Eq. (5.6).

$$\Phi_{\mathrm{H_2}} = \frac{N_{\mathrm{H_2}}^{\mathrm{perm}}}{N_{\mathrm{O_2}}^{\mathrm{ano}} + N_{\mathrm{H_2}}^{\mathrm{perm}}} \tag{5.6}$$

Within Eq. (5.6) $N_{\mathrm{H_2}}^{\mathrm{perm}}$ denotes the hydrogen permeation flux, whereas the anodically evolving oxygen flux is represented by $N_{\mathrm{O_2}}^{\mathrm{ano}}$. This oxygen flux in turn can be obtained by insertion of the applied current density i into Faraday's law (Eq. (5.7)) for the anodic half cell reaction.

$$N_{\mathrm{O_2}}^{\mathrm{ano}} = \frac{i}{4F} \tag{5.7}$$

With these two equations it is now possible to derive the hydrogen permeation flux from the experimentally determined anodic hydrogen content. Therefore Eq. (5.7) needs to be inserted into Eq. (5.6) and solved for the hydrogen permeation flux $N_{\mathrm{H_2}}^{\mathrm{perm}}$.

$$N_{\mathrm{H_2}}^{\mathrm{perm}} = \frac{i}{4F}\frac{\Phi_{\mathrm{H_2}}}{1-\Phi_{\mathrm{H_2}}} \tag{5.8}$$

It has to be kept in mind that this equation is only valid if the separating unit surface area equals the geometrical area of the electrodes. Otherwise Eq. (5.8) needs to be multiplied by the ratio of electrode and separating unit area to account for the additional permeation area (Eq. (5.9)).

$$N_{\mathrm{H_2}}^{\mathrm{perm}} = \frac{i}{4F} \frac{\Phi_{\mathrm{H_2}}}{1 - \Phi_{\mathrm{H_2}}} \frac{A_{\mathrm{el}}}{A_{\mathrm{sep}}} \tag{5.9}$$

Pressure drop method

For the PEM setup further crossover measurements were conducted with the so called pressure drop method. Therefore, the cathode is pumped up with hydrogen gas. After reaching the targeted pressure, a valve on the cathode side is closed. The pressure drop is recorded by a pressure sensor (P-30: 0 bar - 40 bar, Wika). The gas leakage rate of the applied cell was negligibly low in comparison to the crossover. Consequently, the measured pressure decreasing rate is proportional to the hydrogen crossover that can be calculated by the cathodic mass balance. This method can be classified as a dynamical pressure measurement with a constant volume [21].

5.3 Crossover mechanisms

For both electrolysis technologies several possibilities exist, which cause hydrogen crossover. In general these permeation routes can be divided into diffusive and convective mass transfer mechanisms. This chapter will give an overview on the occurring mass transfer mechanisms and will rather point out, which of them are technology specific.

5.3.1 Diffusion

One of the possible crossover mechanisms is the diffusion of electrolysis products across the membrane or separator into the opposite half cell compartment for both technologies. Generally, the products may diffuse through the solid and aqueous phase of the separating unit. However, it is reported that diffusion through the solid phase of a fully hydrated Nafion membrane is roughly one order of magnitude smaller compared to its liquid phase [22, 23]. Similar information can be found for Zirfon$^{\mathrm{TM}}$ as the diffusion through the separator's solid phase is also assumed to be negligible. Additionally, the separator is further presumed to be impermeable for gas bubbles at atmospheric pressure [24]. Thus,

it is comprehensible for both technologies that only species that are dissolved in water or KOH solution are considered for diffusion across the separating unit. This is typically done by application of Fick's law (Eq. (5.10)) in PEM [4, 25–28] and alkaline water electrolysis [16]:

$$N_{\mathrm{H_2}}^{\mathrm{diff}} = D_{\mathrm{H_2}}^{\mathrm{eff}} \frac{\Delta c_{\mathrm{H_2}}}{\delta_{\mathrm{sep}}} \tag{5.10}$$

Here, $\Delta c_{\mathrm{H_2}}$ represents the dissolved hydrogen concentration gradient across the separating unit with the thickness δ_{sep}, whereas $D_{\mathrm{H_2}}^{\mathrm{eff}}$ denotes the effective diffusion coefficient of hydrogen in the membrane or separator. The estimation of the effective diffusion coefficient in polymer electrolyte membranes [29] or porous media [30] is typically done by correction of the molecular diffusion coefficient in the aqueous solvent $D_{\mathrm{H_2}}$ with the porosity ε and tortuosity τ of the separating unit (Eq. (5.11)).

$$D_{\mathrm{H_2}}^{\mathrm{eff}} = \frac{\varepsilon}{\tau} D_{\mathrm{H_2}} \tag{5.11}$$

In PEM electrolysis the concentration gradient across the membrane $\Delta c_{\mathrm{H_2}}$ can be estimated with the cathodic concentration of dissolved hydrogen $c_{\mathrm{H_2}}^{\mathrm{cat}}$ as the anodic hydrogen concentration $c_{\mathrm{H_2}}^{\mathrm{ano}}$ is approximately zero. However, this assumption becomes also applicable for AEL if the electrolyzer is operated with separated electrolyte cycles.

$$\Delta c_{\mathrm{H_2}} \approx c_{\mathrm{H_2}}^{\mathrm{cat}} - \cancelto{0}{c_{\mathrm{H_2}}^{\mathrm{ano}}} \tag{5.12}$$

Henry's law (Eq. (5.13)) states that a species' dissolved concentration is directly proportional to its partial pressure in the gas phase. Therefore, this approach can be applied for the calculation of the cathodic dissolved hydrogen concentration. Within the following Eq. (5.13) $S_{\mathrm{H_2}}$ denotes the hydrogen solubility in the solvent, whereas the cathodic hydrogen partial pressure is represented by $p_{\mathrm{H_2}}^{\mathrm{cat}}$.

$$c_{\mathrm{H_2}}^{\mathrm{cat}} = S_{\mathrm{H_2}} p_{\mathrm{H_2}}^{\mathrm{cat}} \tag{5.13}$$

Data of the hydrogen solubility in pure water was published by Young et al. [31] for atmospheric pressure conditions. Further data for pressures ranging from 25 atm to 1000 atm can be found in the publication by Wiebe and Gaddy [32]. However, literature for the hydrogen solubility in concentrated potassium hydroxide solution is scarce. Ruetschi and Amlie [33] reported data for various electrolyte concentrations at a temperature of 30 °C and atmospheric pressure, whereas Knaster and Apel'baum [34] provided further values at temperatures of 21 °C, 45 °C and 75 °C.

The cathodic hydrogen partial pressure can be obtained if it is assumed that the cathodic oxygen partial pressure is negligible and that the hydrogen is saturated with water vapor. Then the following Eq. (5.14) applies, where p^{cat} denotes the total cathodic pressure:

$$p_{\mathrm{H_2}}^{\mathrm{cat}} = p^{\mathrm{cat}} - p_{\mathrm{H_2O}}^{\mathrm{cat}} \tag{5.14}$$

The calculation of the water vapor pressure may be performed by application of the Antoine equation with parameters for pure water, e.g. [35]. However, the estimation of water vapor pressure above a potassium hydroxide solution necessitates the empirical correlations by Balej [36].

Finally, the diffusional hydrogen flux across the separating unit can be described with the following Eq. (5.15) if the aforementioned assumptions apply and Eq. (5.13) is inserted into Eq. (5.10).

$$N_{\mathrm{H_2}}^{\mathrm{diff}} = D_{\mathrm{H_2}}^{\mathrm{eff}} S_{\mathrm{H_2}} \frac{p_{\mathrm{H_2}}^{\mathrm{cat}}}{\delta_{\mathrm{sep}}} \tag{5.15}$$

The product of the effective diffusion and solubility coefficient $D_{\mathrm{H_2}}^{\mathrm{eff}} S_{\mathrm{H_2}}$ is frequently provided in form of the permeability coefficient $K_{\mathrm{H_2}}$, which is a classical material property for separating units.

5.3.2 Convection

Convection represents another general cause of crossover, which can be divided into several further mechanisms. Generally, convective mass transport is mathematically expressed by Eq. (5.16). There, v_{solv} describes the velocity of solvent (PEM: water, AEL: KOH solution) moving perpendicular to the separating unit, whereas $c_{\mathrm{H_2}}$ denotes the concentration of dissolved gas within the solvent.

$$N_{\mathrm{H_2}}^{\mathrm{conv}} = v_{\mathrm{solv}} c_{\mathrm{H_2}} \tag{5.16}$$

Differential pressure

One possible reason for convective permeation is the transport of electrolyte and dissolved species across the separating unit due to the presence of total pressure gradients. For the mathematical description of this transport mechanism commonly Darcy's law (Eq. (5.17)) is applied, e.g. [24, 25, 28, 37].

$$N_{\mathrm{H_2}}^{\mathrm{dp}} = \frac{K_{\mathrm{sep}}}{\eta} S_{\mathrm{H_2}} p_{\mathrm{H_2}}^{\mathrm{cat}} \frac{\Delta p}{\delta_{\mathrm{sep}}} \tag{5.17}$$

Here, K_{sep} denotes the permeability of the separating unit, η is the dynamic viscosity of the solvent, whereas Δp describes the absolute pressure difference between the cathodic and anodic compartment. The concentration of dissolved hydrogen is again estimated by the insertion of Henry's law (Eq. (5.13)). The hydraulic permeability K_{sep} of porous media such as membranes can be estimated by the Hagen-Poiseuille (Eq. (5.18)) or Kozeny-Carman (Eq. (5.19)) equations [38].

$$K_{\text{sep}} = \frac{\varepsilon d^2}{32\tau} \tag{5.18}$$

$$K_{\text{sep}} = \frac{\varepsilon^3}{K_{\text{koz}} a^2 \left(1-\varepsilon\right)^2} \tag{5.19}$$

Here, ε represents the porosity, d the pore diameter, τ the tortuosity and a the specific surface area of the separating unit, while K_{koz} denotes the Kozeny constant, which depends on the porous media [39]. For a rough estimation of the hydraulic permeability K_{sep} in this work the Hagen-Poiseuille equation (Eq. (5.18)) is used. The necessary porosities and pore diameters of both applied separating units are given within the setup section. In order to make a worst case estimate the tortuosity is chosen to be $\tau = 1.5$ for both systems. Therewith the permeability for the Nafion membrane and Zirfon$^{\text{TM}}$ separator are approximated to be $5 \cdot 10^{-20}\,\text{m}^2$ and $2 \cdot 10^{-16}\,\text{m}^2$, respectively. These estimates match literature data of both separating units quite well, e.g. [17, 40]. Hence, AEL with a porous separator is theoretically more prone to convective permeation. But it has to be noted that it is also more convenient to mix the electrolyte cycles at identical pressure levels, which is also an important reason for balanced pressure operation. However, if it is assumed that commonly applied back pressure control valves are capable of controlling the anodic and cathodic pressures with an accuracy of roughly 1 %, it becomes comprehensible that a differential pressure across the separator may be formed. Thus, it is conceivable that either dissolved hydrogen or oxygen could convectively be transported into the opposite half cell.

In contrast, literature suggests that no pressure-driven permeation is evident for Nafion membranes [23, 41], which is supported by the low calculated permeability of the membrane used in this study. This allows the operation of PEM electrolyzers under asymmetrical pressure conditions. Here, the cathode is typically pressurized, whereas the anodic cycle stays at atmospheric pressure, which can be favorable in terms of energy demand, e.g. [26, 42, 43]. However, if alternative membrane materials are applied, this operation

mode may also promote a permeation flux as the resulting pressure-driven water flow carries dissolved hydrogen into the anodic compartment [28].

Electro-osmostic drag

A further possibility to cause convective permeation is the electro-osmotic drag. Due to the electric field and the associated movement of ions, the electroneutral solvent can be dragged with them across the separating unit. Hence, dissolved gas may also be transported through it [26, 28, 44]. Thus, in PEM electrolysis dissolved oxygen may be dragged along with the transport of protons from the anodic into the cathodic half cell. In contrast, the electro-osmotic drag could also be capable of reducing hydrogen permeation as it may transport dissolved hydrogen back to the cathode. On the contrary, OH^- ions are responsible for the charge transport in AEL. According to the half cell reactions (Eq. (5.4)) and (5.5)) these hydroxide ions are transported from the cathodic to the anodic compartment, which therefore may enhance hydrogen and reduce oxygen crossover. However, no publication was found that could confirm or quantify this mechanism. A rough estimation of the electro-osmotic crossover flux can be carried out with the following Eq. (5.20):

$$N_{\mathrm{H_2}}^{\mathrm{drag}} = \frac{S_{\mathrm{H_2}} p_{\mathrm{H_2}}^{\mathrm{cat}}}{c_{\mathrm{solv}}} \frac{n_{\mathrm{drag}} i}{F} \tag{5.20}$$

Here, c_{solv} is the concentration of solvent within the separating unit and n_{drag} is the electro-osmotic drag coefficient, which describes the ratio between the flux of dragged solvent molecules to that of the charged ions. Jacobson et al. [45] compared drag coefficients of proton-conducting Nafion membranes to that of a hydroxide-conducting Tokuyama A201 membrane for the application in acid and alkaline fuel cells. Their results showed a smaller value for the anion-conducting membrane, which may be attributed to the different charge carrier or water domain. A temperature-dependent correlation for the estimation of the drag coefficient in a Nafion membrane used for PEM electrolysis can be found in the publication by Onda et al. [46].

Electrolyte mixing

The electrochemical reactions in AEL (Eq. (5.4) and (5.5)) cause a change in electrolyte concentration since water is consumed at the cathode, whereas it is produced in the anodic half cell. Therefore the anodic and cathodic electrolyte cycles are usually mixed

together to balance this concentration gradient [47]. However, this process management leads to a decrease of the resulting product gas purity as the electrolyte is saturated with dissolved electrolysis products. Thus, the electrolysis cell is continuously fed with dissolved hydrogen and oxygen from the gas separators, where they are then able to outgas. Of course, separating the electrolyte cycles prevents this crossover mechanism at all. But due to the shift in the anodic and cathodic electrolyte concentrations the cell efficiency may decrease, as the electrolyte conductivity is reduced with prolonged time.

5.3.3 Supersaturation

It is generally assumed for gas evolving electrodes that the electrolysis products are produced in dissolved form [48] before gas bubbles grow at active nucleation sites. Nucleation sites are small electrode surface irregularities, which depend on the material and its roughness [49]. For the nucleation sites to become active a sufficient deviation from equilibrium concentration of the generated product is mandatory [50]. Therefore, the electrolyte becomes supersaturated, which describes a higher concentration of dissolved hydrogen within the electrode boundary or catalyst layer than it would be expected through Henry's law (Eq. (5.13)). The existence of this supersaturated concentration of dissolved species could already be proven experimentally, e.g. [51, 52]. Consequently, the subsequent mass transfer of dissolved hydrogen is mainly controlled by two competing mechanisms. Thus, dissolved hydrogen is either transported to the electrolyte bulk in dissolved form or to the gas-liquid interface of gas bubbles present in the electrode boundary layer [53]. However, dissolved hydrogen may also be transported through the separating unit of the electrolysis cell [5].

As theory of the aforementioned diffusive and convective crossover mechanisms only supposed hydrogen equilibrium concentration (Henry's law), supersaturation enhances these crossover mechanisms in PEM and zero-gap alkaline electrolysis. However, the influence of supersaturation on crossover can only be accounted, if the previously mentioned equations are expressed in their concentration forms instead of the gas pressure expressions. Then Eq. (5.21) can be used for the calculation of the dissolved gas concentration within the catalyst layer in PEM electrolysis [5]:

$$c_{\mathrm{H_2}}^{\mathrm{cat}} = \frac{\frac{i}{2F} + k_{\mathrm{L}} p_{\mathrm{H_2}}^{\mathrm{cat}} S_{\mathrm{H_2}}}{k_{\mathrm{L}} + \frac{D_{\mathrm{H_2}}^{\mathrm{eff}}}{\delta_{\mathrm{sep}}}} \tag{5.21}$$

Here k_L denotes the mass transfer coefficient, which includes several transport and transfer steps: beginning with the desorption of the electrolysis product from the catalyst particles up to the transfer into the gas phase within the pore space. For the PEM catalyst layers it is suggested that this mass transfer coefficient is significantly affected by the diffusion of the dissolved gas from the catalyst particles to the pore space through the ionomer. Already small limitations can lead to a significant increase of the dissolved gas concentration [5]. Additionally, Eq. (5.21) reveals that supersaturation also increases towards higher current densities. So, it is necessary to consider that the concentration of dissolved gas is not solely a function of gas solubility, system pressure and the electrode specific mass transfer coefficient, but also of current density: $c_{H_2}^{cat} = f(p_{H_2}^{cat}, S_{H_2}, k_L, i)$.

5.3.4 Summary and comparison of crossover mechanisms

The previously described crossover mechanisms of both technologies are summarized and directly compared in Tab. 5.1. It is stated, which impact each individual crossover mechanism has on the overall crossover flux of the respective technology. The assessment of the individual influences is supported by a direct comparison of the key parameters controlling the mechanisms. Therefore, the crossover equations are given in their concentration forms.

For diffusive crossover through the separating unit every relevant parameter effects a higher permeation rate for PEM electrolysis compared to alkaline cells. The membrane is thinner and the diffusion coefficient of hydrogen in pure water is larger than in a KOH solution. Certainly, the solubility of hydrogen in pure water is also one order of magnitude higher than in a 30 wt% KOH electrolyte. For lower concentrations of KOH the diffusion and solubility coefficients increase towards the values of water. Consequently, the diffusive crossover increases in AEL with lower concentrated potassium hydroxide electrolytes.

The convective crossover is divided into the three different mechanisms: differential pressure, electro-osmotic drag and electrolyte mixing. As it was discussed previously, dissolved hydrogen can be carried into the anodic half cell due to a pressure-driven water or electrolyte flow. Therefore, low hydraulic permeabilities are essential to avoid this crossover mechanism. In this case, the Zirfon^{TM} separator applied in AEL shows a 3 to 4 orders of magnitude higher hydraulic permeability than the Nafion membrane. Although hydrogen solubility in concentrated alkaline electrolytes is low, the estimated permeabil-

Tab. 5.1: Comparison of the crossover mechanisms with key parameters and evaluation of the impact on the overall gas crossover of the respective technology. If no special information given, stated values are valid for a temperature of 60 °C and in case of AEL for a KOH concentration of 30 wt%.

Mechanism	Equation	Parameter / Symbol / Unit	PEM (Nafion)		AEL (Zirfon)
Diffusion	$N_{H_2}^{diff} = D_{H_2}^{eff} \frac{c_{H_2}^{cat}(p_{H_2}^{cat}, S_{H_2}, k_L, i)}{\delta_{sep}}$		very high	$\gg$	low
		thickness / δ_{sep} / µm	20 - 250	$<$	500
		solubility coefficient / S_{H_2} / mol Pa^{-1} m^{-3}	$3.8 \cdot 10^{-6}$[a] [33]	$\gg$	$3.6 \cdot 10^{-7}$[b] [31]
		diffusion coefficient in solvent / D_{H_2} / m^2 s^{-1}	$8.9 \cdot 10^{-9}$[c] [54]	$>$	$3.3 \cdot 10^{-9}$[c] [20]
Convective					
Differential pressure	$N_{H_2}^{dp} = \frac{K_{sep}}{\eta} c_{H_2}^{cat}(p_{H_2}^{cat}, S_{H_2}, k_L, i) \frac{\Delta p}{\delta_{sep}}$		low	$\ll$	possibly high
		hydraulic permeability / K_{sep} / m^2	$5 \cdot 10^{-20}$[d]	$\ll$	$2 \cdot 10^{-16}$[d]
Electro-osmotic drag	$N_{H_2}^{drag} = \frac{c_{H_2}^{cat}(p_{H_2}^{cat}, S_{H_2}, k_L, i)}{c_{solv}} \frac{n_{drag} i}{F}$		low[e]	$>$	even lower[e]
		drag coeff. / n_{drag} / –	2.8 [45] - 4.5 [46]	$>$	1.3[f] [45]
		solvent conc. / c_{solv} / mol m^{-3}	$55 \cdot 10^3$[g]	$\approx$	$56 \cdot 10^3$[g]
Electrolyte mixing	$N_{H_2}^{mix} = f(p_{H_2}^{cat}, S_{H_2}, k_L, i, \dot{V})$		no mixing	$\ll$	very high

[a] value for 30 °C in pure water

[b] value for 30 °C in 32.3 wt% KOH

[c] diffusion coefficient for water and 30 wt% KOH - the effective coefficient can be estimated via Eq. (5.11)

[d] calculated within this work via Eq. (5.18)

[e] absolute convective drag may be lower for AEL, but due to opposite ion migration hydrogen permeation is increased in AEL and decreased in PEM

[f] value for a Tokuyama A 201 anion exchange membrane

[g] estimated by the following equation: $c_{solv} \approx \frac{\varrho_{solv}}{M_{solv}}$

ity of the Zirfon^{TM} separator allows a distinct crossover at moderate pressure gradients already.

In contrast, the second convective crossover through the separating unit caused by the electro-osmotic drag is higher for PEM electrolysis as the water drag coefficient and solubility is larger in this case. However, the electro-osmotic drag is assumed to reduce hydrogen, but increase oxygen crossover in PEM electrolysis. This is different for AEL as the ions migrate into opposite directions in the two technologies. Nevertheless, the influence of this crossover mechanism is assumed to be small, since the estimation only suggests a small flow of dragged water or electrolyte with low concentrations of dissolved gas. However, at high current densities and high system pressures this mechanism can become more important as the concentration of dissolved gas is increased.

Since mixing of the anodic and cathodic electrolyte cycles is not performed in PEM electrolysis, this represents no crossover mechanism here. In contrast, this is one of the main sources of crossover in AEL. The mixing of gas saturated electrolyte cycles leads to a high exchange of both gases. This phenomenon is mainly influenced by the dissolved gas concentrations and the electrolyte flow rates, but also by the applied gas separators. Consequently no single equation can be used to calculate hydrogen crossover through electrolyte mixing. Nevertheless, a mathematical model was presented in a previous publication [16], which can be used for an estimation of this crossover effect.

5.4 Results and discussion

Firstly, this section illustrates the influence of current density and system pressure on the measured gas purity in PEM and alkaline electrolysis. Subsequently, the permeation fluxes through the separating units are derived from these experimental results in order to clarify the influence of current density. Following this, a breakdown of the individual crossover mechanisms of both technologies is shown. Finally, the chapter is concluded by a study of the influence of the separating unit thickness on the anodic hydrogen content.

5.4.1 Anodic hydrogen impurity

Fig. 5.3 (a) and (b) summarize the measured anodic hydrogen fractions of the experiments conducted in this work for a current density range from 0.05 A cm^{-2} to 1 A cm^{-2}, pressures

ranging from 1 bar to 20 bar, a temperature of 60 °C and different process management possibilities. Additionally, the results of the reference measurements without electrolysis operation are shown.

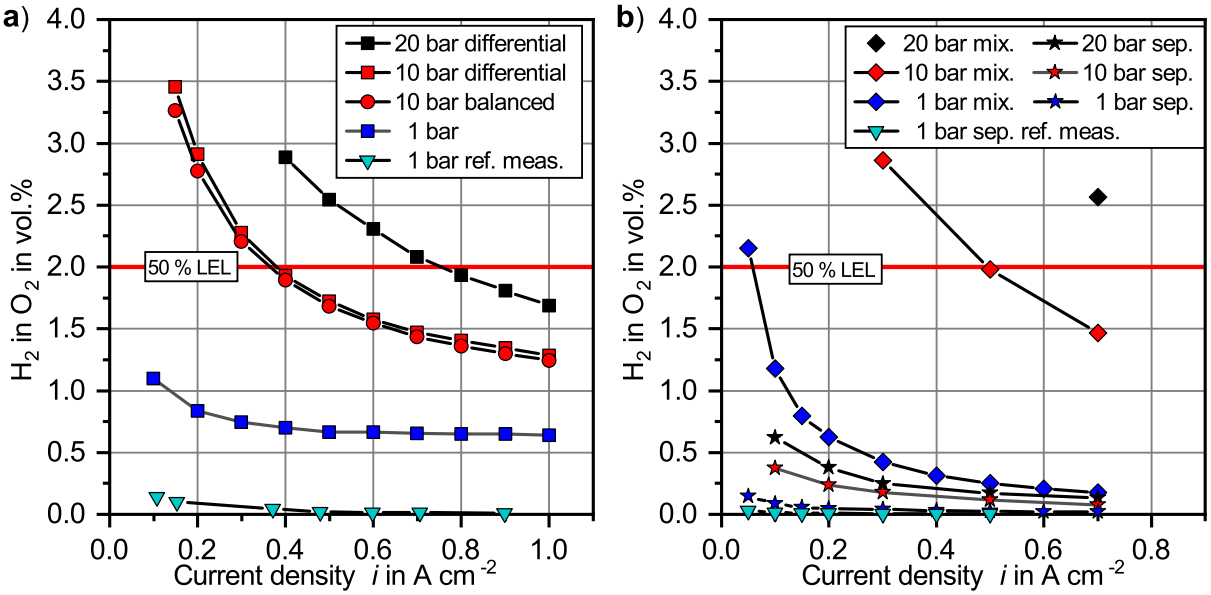

Fig. 5.3: Measured anodic hydrogen content as a function of current density for the PEM (a) and alkaline (b) electrolysis setup at a temperature of 60 °C, different system pressures and process management strategies.

Firstly, it becomes obvious for both electrolysis technologies that higher applied current densities lead to a decrease of the anodic hydrogen contamination. This can be explained with a rising oxygen evolution rate $N_{O_2}^{ano}$ towards higher current densities, which dilutes the permeating hydrogen and therefore reduces its fraction (s. Eq. (5.6) and (5.7)).

It can further be seen in both experimental data sets that an increase of the operating pressure effects a drastic increase of the anodic hydrogen content. Thus, in PEM electrolysis a pressure change from 1 bar to 20 bar leads to an increase of the anodic hydrogen content from 0.654 vol% to 2.08 vol% at a current density of 0.7 A cm^{-2}. Accordingly, in AEL equal operating conditions caused an increase from 0.018 vol% to 0.130 vol% with separated electrolyte cycles, whereas mixed cycles yielded a change from 0.178 vol% to 2.564 vol%. So, it becomes clear that alkaline process management possibilities reveal distinct differences in the resulting anodic hydrogen fraction. This huge deviation is caused by the mixing of the anodic and cathodic electrolyte cycles. Thus, depending on the separation performance of the gas separators, dissolved or even gaseous hydrogen is

transported into the anodic half cell where it contaminates the evolving oxygen. This effect becomes more relevant towards rising system pressures as the amount of dissolved gas within the electrolyte increases, whereas the mean gas bubble diameter decreases, which further complicates a proper gas separation. However, it has to be stated that hydrogen crossover due to electrolyte cycle mixing becomes less important with a growing electrolysis plant size if the electrolyte recirculation rate is kept constant [7, 55]. The alkaline electrolyzer in this study was operated with a recirculation rate of 70 electrolyte replacements an hour. For minimum crossover through electrolyte mixing, the recirculation rate should always be kept as low as possible. It must be ensured though that the flow rate is high enough to keep the temperature increase within the cell below certain limits. Furthermore, it is important to emphasize that a reduction of the electrolyte recirculation may lead to an increase of the electrode bubble coverage, which effects an increase of cell voltage. In PEM electrolysis, by contrast, no significant distinction between differential and balanced pressure operation is noticeable at a system or cathodic pressure of 10 bar.

As it was described earlier, both electrolysis test cells were also fed with hydrogen and oxygen according to their volumetric flow rates in a current density range from $0.05\,\mathrm{A\,cm^{-2}}$ to $0.9\,\mathrm{A\,cm^{-2}}$ while being disconnected from the power supply. In the following, these experiments will be referred to as reference measurements. The obtained results are also included in Fig. 5.3. It can easily be seen that the measured hydrogen fractions are well below the results of the electrolysis measurements. While only a value of 0.022 vol% was measured in the PEM setup, the alkaline cell yielded a concentration of 0.004 vol% with separated electrolyte cycles at a current density of $0.5\,\mathrm{A\,cm^{-2}}$.

In summary, the results indicate clearly that safety issues limit the pressurized operation of the PEM and classical alkaline electrolysis setup with mixed electrolyte cycles as the anodic hydrogen content rises above 2 vol%, which corresponds to approximately 50 % of the lower explosion limit [47]. Consequently, electrolyzers are typically shut down as soon as this concentration is exceeded [1, 6]. Therefore, both electrolysis test stations cannot be operated safely under specific current density and pressure conditions if no measures are taken to reduce the crossover or the hydrogen content within the anodic half cell. Subsequently to this chapter different mitigation strategies are discussed.

5.4.2 Hydrogen permeation through the separating unit

With the previously shown hydrogen fractions it is hard to assess the correlation between hydrogen crossover and current density. However, with Eq. (5.8) and the measured hydrogen content, the hydrogen crossover $N_{H_2}^{perm}$ can be achieved for the different applied current densities. In Fig. 5.4 (a) and (b) the determined hydrogen crossover through the Nafion 117 membrane and the Zirfon^{TM} separator is shown as a function of current density. In case of the alkaline system, measurement data with mixed electrolyte cycles are excluded, so that only hydrogen permeation through the separator is evaluated.

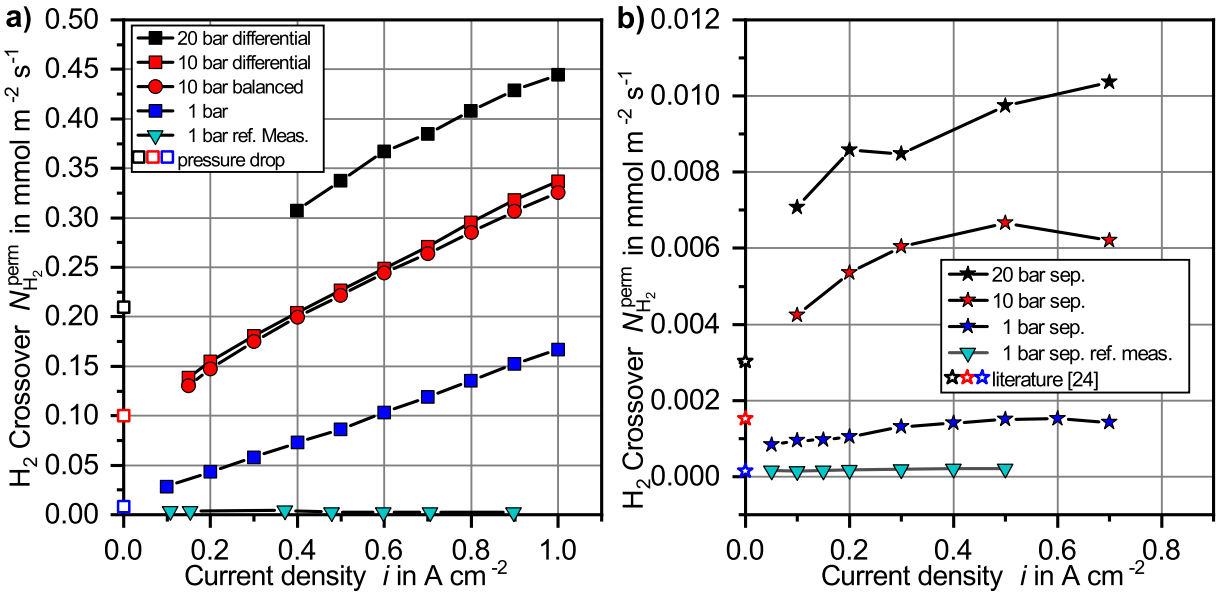

Fig. 5.4: Determined hydrogen crossover in the PEM (a) and alkaline (b) electrolysis setup at different pressure conditions and 60 °C. Hollow symbols at the y-axis represent pressure drop and literature data.

Furthermore, Fig. 5.4 also shows the results of the reference measurements. It can be seen for both technologies that the determined crossover fluxes remain constant with increasing current density and that the values are small compared to the results during electrolysis operation. These constant measurement values can be explained by the fact that the electrolyte is gas saturated by the continuous supply of hydrogen and oxygen, which results in a constant diffusive flux across the separating unit (s. Eq. (5.15)), whereas no other crossover mechanisms occur as the experiments were conducted under atmospheric pressure conditions and no supersaturation can be formed. Additionally, Fig. 5.4 provides values for the purely diffusive hydrogen crossover at zero current, which

are represented by hollow symbols. For the PEM electrolysis experiments these values were determined according to the aforementioned pressure drop method, whereas the values for the alkaline system were calculated from data provided by Schalenbach et al. [24]. Here it is recognizable that the reference measurements of both electrolysis systems show excellent agreement with the zero current values of the pressure drop and literature data at atmospheric pressure, which therefore confirms the purely diffusive crossover occurring in these measurements.

In contrast to the data of the reference measurements, the results of both technologies show that hydrogen crossover through the separating unit primarily increases with rising current density and also system pressure during electrolysis operation.

Thus, Fig. 5.4 (a) reveals a clear linear dependency of the hydrogen crossover on the current density for the PEM electrolysis measurements, which has also been observed in the literature, e.g. [5, 14]. This linear growth can be explained with mass transport resistances within the cathode catalyst layer that cause an increasing supersaturation of dissolved hydrogen with increasing current density [5]. The slope of the crossover is approximately equal for all the investigated pressure stages, since the mass transport resistance is assumed to be mainly affected by geometrical and/or structural parameters and less by operating conditions [5, 13]. As the linear extension of the determined hydrogen crossover matches the zero current values excellently, a linear dependency of the hydrogen crossover is also assumed for even smaller current densities. Finally, it can also be seen that the balanced and differential pressure operation at a system or cathodic pressure of 10 bar show no significant difference in hydrogen crossover. This was expected, since literature also suggests no pressure-driven convective crossover for Nafion membranes at this pressure gradient [23, 41].

The AEL results are shown in Fig. 5.4 (b), where no specific trend becomes obvious at first. However, the data suggests that hydrogen crossover initially also increases with rising current density until a plateau is formed. Additionally, increasing system pressures seem to shift the formation of the plateau towards higher current densities. This effect may be explained with an increase of the hydrogen mass transfer coefficient from the liquid electrolyte into the gas phase at higher current densities. As previously mentioned, electrolysis products are assumed to be generated in dissolved form before gas is evolved in a subsequent physical step. Therefore, dissolved hydrogen may leave the elec-

trode either in gaseous state through the transport into adhering bubbles and subsequent bubble detachment or in dissolved form through transport into the electrolyte bulk or across the separator. For the description of this phenomenon Vogt [56] introduced the gas evolution efficiency, which describes the ratio of product transported into gas bubbles at the electrode to the total generated flux. Literature values for the gas evolution efficiency [57–59] show a strong increase at low current densities (up to approx. $0.2\,\mathrm{A\,cm^{-2}}$) until a linear dependency can be observed. Hence, at very small current densities nearly the total amount of product leaves the electrode in dissolved form. As the current density increases, the concentration of dissolved hydrogen becomes high enough to activate nucleation sites, which enable the evolution of gas bubbles at the electrode [50]. Therefore, the fraction of product leaving the electrode in dissolved form decreases with higher current densities, which consequently limits the flux of dissolved hydrogen across the separator. Furthermore, it is assumed that an increase in pressure moves the gas evolution efficiency towards higher current densities, which would explain the later plateau formation. Thus, a pressure increase enhances the mandatory dissolved gas concentration for activation of nucleation sites and reduces the mass transfer coefficient ($k_\mathrm{L} = f(Re)$) of dissolved hydrogen into adhering bubbles, as the Reynolds number $Re = u \cdot d_\mathrm{b}/\nu$ is decreased by smaller bubble diameters. Of course, it may also be possible that the determined crossover is superimposed by the convective transport of dissolved hydrogen across the separator. However, this is questioned with the current state of knowledge as the anodic cycle showed an approximately 20 mbar higher pressure at elevated pressure stages, which would have suppressed convective hydrogen permeation. Finally, in contrast to PEM electrolysis, where a linear dependency of the crossover can be assumed for the complete investigated current density range, the analysis of the alkaline zero current values suggests a strong increase of the crossover at small current densities. However, further investigations are necessary to confirm this presumption.

The overall comparison of the electrolysis results shows that diffusive crossover in PEM electrolysis is more than one order of magnitude higher than in AEL, which is mainly a consequence of the lower hydrogen solubility in concentrated potassium hydroxide solution. So, in comparison to pure water the solubility is decreased by a factor of 8 in 30 wt% KOH at a temperature of 30 °C and a gas partial pressure of 1.013 bar [7]. Similar information was published by Schalenbach et al. [60], who reported a 38 times lower hydrogen

permeability coefficient in Zirfon^{TM} soaked with 30 wt% KOH compared to Nafion 117 immersed in water at a cell temperature of 80 °C.

5.4.3 Crossover breakdown

In this chapter the respective share of the different crossover mechanisms is graphically depicted in Fig. 5.5 for PEM and classical alkaline water electrolysis with mixed electrolyte cycles at atmospheric pressure conditions.

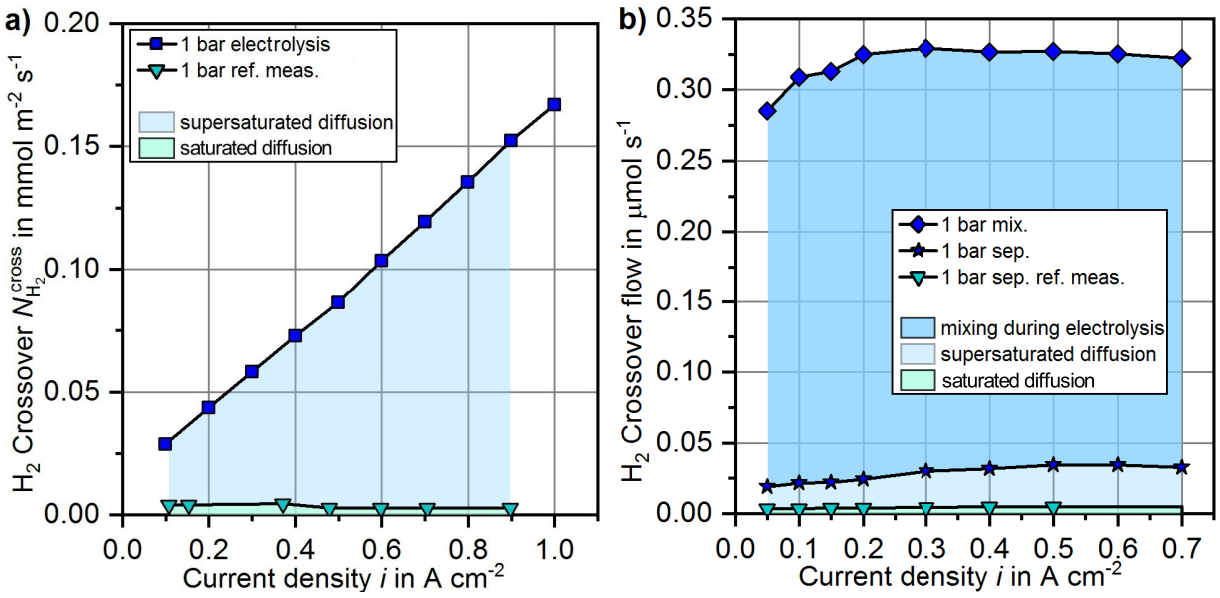

Fig. 5.5: Crossover breakdown for the PEM (a) and classical alkaline (b) electrolysis experiments under atmospheric pressure conditions. Since crossover through electrolyte mixing does not represent a cell-specific quantity, the y-axis of the alkaline experiments shows the actual molar flow rates.

Fig. 5.5 (a) shows the breakdown of the achieved PEM electrolysis results. Here, the hydrogen crossover can be divided into two different areas. Firstly, a small proportion of the overall crossover is caused by diffusion due to saturated dissolved hydrogen, which has been determined with the reference measurements. The second and major part is also a result of diffusion, but is caused by a supersaturated hydrogen concentration in the cathodic half cell. The percentage of this effect increases with current density. Whereas 86 % are transported across the membrane at 0.1 A cm^{-2}, a current density of 1 A cm^{-2} shows a share of 98 % since supersaturation increases linearly with current density as it was stated before.

Furthermore, the results indicate that the percentage of crossover due to supersaturation decreases with increasing cathodic pressure. The values for the higher cathodic pressures are based on the results of the pressure drop method. At a pressure of 10 bar the share is 70 %, while only 53 % are determined at 20 bar for a current density of 1 A cm^{-2}. This can be explained by the fact that diffusive crossover due to saturated dissolved hydrogen increases with raising pressure, whereas the supersaturation is nearly pressure independent. Thus, the current density effect loses importance at very high cathodic pressures.

The crossover breakdown for the atmospheric AEL experiments is shown in Fig. 5.5 (b). Since the classical process management with mixed electrolyte cycles is chosen for the evaluation of the individual crossover fractions, the previously shown area-related diffusive crossover fluxes need to be multiplied by the surface area of the separator as crossover by mixing the electrolyte cycles does not represent a cell-, but electrolyzer-specific value.

Therefore, Eq. (5.9) is used for the estimation of the overall crossover with mixed electrolyte cycles and then multiplied by the surface area of the separator. In order to simplify the evaluation, it is assumed that the diffusive crossover due to electrolyte saturation and supersaturation, which were determined with separated cycles, can also be transferred to mixed electrolyte cycles. However, the diffusive crossover should be slightly smaller with mixed electrolyte cycles, since the electrolyte entering the half cells is already saturated with hydrogen and oxygen, thus reducing the concentration gradient across the separator. Therefore, the share of crossover due to electrolyte mixing might be even larger for this specific test station than shown in the following. The trend of the diffusive crossover due to saturation and supersaturation of the electrolyte was already discussed in the previous section. At a current density of 0.7 A cm^{-2} their shares amount to 1.4 % and 8.6 %, respectively. Here, similar to PEM electrolysis, a slight increase of the diffusional crossover due to supersaturation can be observed with rising current density as the share at 0.1 A cm^{-2} is determined to be 6.0 %.

However, it is obvious that the mixing of the electrolyte cycles represents the largest source for transferring hydrogen into the anodic half cell. This crossover flow remains approximately constant over the whole investigated current density range as regardless of the applied current density gas-saturated electrolyte is always fed into the half cells. Only at smaller current densities a minor increase of this mechanism is recognizable, which

might be regarded to not only dissolved species, but also gas bubbles being transported back into the electrolysis cell. The percentage of crossover due to electrolyte mixing is the highest for all investigated pressure stages, yielding 90 % at atmospheric pressure, 88 % at 10 bar and 95 % at 20 bar for a current density of 0.7 A cm^{-2}. These high values exemplify once more that an improvement of the anodic hydrogen concentration can in particular be achieved by an optimized lye circulation strategy.

5.4.4 Variation of separating unit thickness

The experimental results showed that safety issues can limit the operating ranges of the electrolyzers under certain conditions with the investigated state-of-the-art separating unit materials. In the following section, the influence of the separating unit thickness on the anodic hydrogen content is studied. Therefore, the anodic gas contamination is estimated for thinner separating units on basis of the obtained experimental data.

It is assumed for the PEM system that neither supersaturation nor the permeability coefficient are influenced by the membrane thickness. Thus, the overall crossover flux $N_{\mathrm{H_2}}^{\mathrm{cross}}$ for different membrane thicknesses can be calculated according to Eq. (5.22).

$$N_{\mathrm{H_2,PEM}}^{\mathrm{cross}} = N_{\mathrm{H_2,exp}}^{\mathrm{perm}} \frac{\delta_{\mathrm{N117}}}{\delta_{\mathrm{sep}}} \tag{5.22}$$

The same assumptions also apply for the alkaline system. Furthermore, crossover through electrolyte mixing is also independent on separator thickness. Therefore, Eq. (5.23) may be used for the calculation of the overall crossover flux at alternative separator thicknesses.

$$N_{\mathrm{H_2,AEL}}^{\mathrm{cross}} = N_{\mathrm{H_2,exp}}^{\mathrm{mix}} + N_{\mathrm{H_2,exp}}^{\mathrm{perm}} \frac{\delta_{\mathrm{Zirfon}}}{\delta_{\mathrm{sep}}} \tag{5.23}$$

Subsequently, the hydrogen content can be calculated with Eq. (5.6) for both technologies in variation of the separating unit thickness. The obtained results are depicted in Fig. 5.6 for atmospheric pressure conditions and a temperature of 60 °C. The ohmic resistances R_{sep} shown there are calculated according to Eq. (5.24).

$$R_{\mathrm{sep}} = \frac{\delta_{\mathrm{sep}}}{\sigma_{\mathrm{sep}}} \tag{5.24}$$

Here, σ_{sep} denotes the ionic conductivity of the separating units, which were achieved from the literature. For a Nafion 117 membrane immersed in water the conductivity is given with roughly 13.5 S m^{-1} at 60 °C [61]. Vermeiren et al. [62] provide a value of

$0.166\,\Omega\,\mathrm{cm}^2$ for a Zirfon^{TM} separator with a thickness of 500 µm at a temperature of 60 °C and a potassium hydroxide concentration of 30 wt%. Correspondingly, the insertion into Eq. (5.24) yields an ionic conductivity of $30.1\,\mathrm{S\,m^{-1}}$. Although the electrolyte applied in this study is slightly higher concentrated, the value of Vermeiren et al. can still give an approximate estimation.

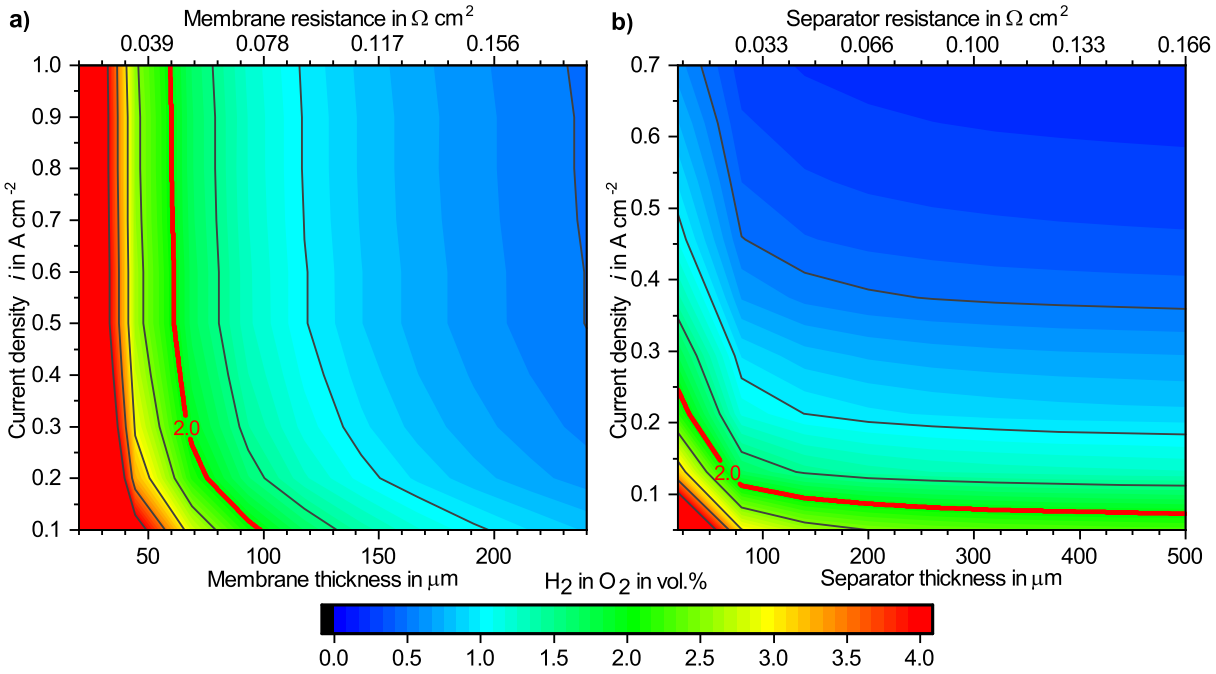

Fig. 5.6: Anodic hydrogen content as a function of separating unit thickness and current density for PEM (a) and alkaline electrolysis (b) at atmospheric pressure, a temperature of 60 °C and 32 wt% KOH. Calculations are based on the obtained experimental data for the N117 membrane and the Zirfon^{TM} separator.

The heatmaps of Fig. 5.6 show the correlation between the separating unit thickness on the bottom or the respective electrical resistance on the top x-axis and current density on the y-axis. The hydrogen content itself is depicted in form of contour lines. A comparison of the two technologies shows that the contour lines point in different directions. Thus, in PEM electrolysis the lines are ordered vertically, while the hydrogen content in AEL roughly shows a horizontal curve.

The contour plot for PEM electrolysis reveals that the hydrogen content strongly increases with a decreasing membrane thickness. This results from the purely diffusive character of hydrogen crossover in the PEM setup, which increases inversely proportional with a decreasing membrane thickness (s. Eq. (5.10)). Consequently, the trend towards thinner membranes to reduce ohmic losses can only be realized with a simultaneous re-

duction of the hydrogen content in the anode or the crossover itself.

Fig. 5.6 (b) shows a totally different trend for the hydrogen content with a decreasing separator thickness in AEL. Here, the hydrogen content is nearly independent on the separator thickness. An increase of the hydrogen concentration due to diffusion can only be observed at thicknesses below 100 µm. This can be explained with the fact that the main portion of hydrogen crossover is caused by mixing of the electrolyte cycles, whereas diffusive crossover only represents a very small share. So, the alkaline cell, equipped with a Zirfon^{TM} separator, shows that the reduction of the separator thickness offers high potential for improving ohmic losses if the mechanical stability can be maintained and this is technically feasible. However, it has to be said that convective crossover gains in importance with a decreasing separator thickness, which necessitates a complex pressure control to keep the differential pressure at a minimum.

5.5 Mitigation strategies

In this section strategies for the mitigation of crossover and corresponding side effects are discussed for both technologies. These strategies are summarized in Tab. 5.2 and divided into five categories. The different strategies are evaluated regarding the five following criteria: safety issues (H_2 in O_2), degradation (catalyst layer/electrode, membrane) due to crossover, Faraday efficiency, electrochemical performance and costs.

Separating unit

Particularly in PEM electrolysis the use of highly ion-conductive membranes with lower hydrogen permeability is an interesting possibility to solve existing safety issues. This may not only increase the Faraday efficiency, but the overall performance of the electrolyzer. In literature some promising candidates can be found, e.g. radiation grafted membranes [63] or hydrocarbon-based materials [64]. In contrast, for AEL the previous results suggest that diffusive crossover may not be significantly reduced with advanced materials, as the diffusional flux is already very limited due to the poor solubility of hydrogen and oxygen in the highly concentrated electrolyte. However, if lower electrolyte concentrations are to be used in the future, this approach will become more important as better cell efficiencies can be achieved with ion-conductive membranes in this operating regime, e.g. [65, 66].

Another possibility for a reduction of the anodic hydrogen content would be the increase of the membrane thickness, which of course would be linked to a reduction of the electrolyzer performance. So, this is not a real option and also does not reflect the trend of research and development.

Recombination catalyst

A totally different approach is the application of recombination catalysts, which enable the reaction of permeated hydrogen back to water. For PEM electrolysis, it has already been shown that the incorporation of platinum is able to reduce the anodic hydrogen content significantly if the catalyst is applied to the backside of the current collectors. Even better results were obtained, when the recombiner was positioned downstream of the gas separators as the optimal operation necessitates dry gases [8]. Additionally, it is also conceivable to integrate the catalyst directly into the electrode [9] or separating unit in order to provide a large contact area between the permeating gases and the recombination catalyst. But it is important to emphasize that the introduction of recombination catalysts only reduces the risk of explosive mixtures, whereas the Faraday efficiency is not improved as this measure does not address the origin of crossover.

Reduction of supersaturation

As it was discussed before, supersaturation strongly enhances the diffusional crossover in both technologies. Therefore, especially when membrane electrode assemblies are applied, it should be examined whether transport resistances that contribute to the formation of supersaturation can be reduced by improved geometrical and structural properties of the electrodes or catalyst layers. The comparison of literature data for PEM electrolysis reveals different slopes for the crossover increase with rising current density, which is presumed to be mainly an effect of different geometrical or structural properties [5].

Furthermore, the influence of external impacts on the electrolysis cell on supersaturation of the electrolyte could be investigated. Li et al. [67] reported that they were able to reduce the energy demand in AEL, when the cell was operated under the influence of ultrasound as the evolving gas bubbles were removed from the electrode surface more quickly. Here, it is also conceivable that an ultrasonic field could promote the formation of gas bubbles from the supersaturated electrolyte, which consequently would reduce the

dissolved concentration of electrolysis products. Similar approaches are the application of magnetic [68] or gravitational [69] fields, which have already been shown to reduce cell voltage in AEL. It is difficult to estimate in which way these technologies influence supersaturation of dissolved gas within the respective electrolysis technology, but certainly represent an interesting field of research, since performance, crossover and also Faraday efficiency could be improved.

Interlayer

Another option to reduce crossover or the corresponding negative effects is placing thin interlayers within the separator or between the electrode and the separating unit. These interlayers could consist of a material that is characterized by a low permeability coefficient, but capable for the ionic transport. For instance, this approach was shown using hexagonal boron nitride and graphene in methanol fuel cells, e.g. [70]. For PEM fuel cells this was also successfully demonstrated through the application of a graphene oxide / cerium oxide interlayer [71]. This method could be very effective, because of the reduction of crossover at its origin and therefore all negative effects.

Another interlayer could be realized in form of a third electrode that is electrically connected to the hydrogen evolving cathode and supplied by an additional power source. In case of PEM water electrolysis the permeating hydrogen can be oxidized to protons at the third electrode, which will then be pumped back to the cathode electrochemically. This method was already successfully demonstrated by Schalenbach et al. [72]. They also showed that this third electrode can work in combination with the oxygen evolving anode. In this case permeating hydrogen is oxized at the additional electrode, while the anode works as a fuel cell locally. Furthermore, a four electrode arrangement supplied by two additional power sources could also be used to send back permeating hydrogen and oxygen in AEL. Here, one electrode each would have to be connected to the anode and cathode of the electrolysis cell, whereby the reverse reactions of the corresponding gas-evolving electrode would then take place there. However, placing additional electrodes is expensive and further complicates cell stack design.

Finally, it is also possible to apply a recombination catalyst as an interlayer, which has already been described before (s. Tab. 5.2 2.d).

Process management

It could be shown for AEL that mixing of the electrolyte cycles represents the most important crossover mechanism. For this reason advanced gas separators should ensure that no gaseous species are transported back into the cell even at high system pressures.

Furthermore, Schug [55] reported that the amount of recycled dissolved species can be reduced with an adequate electrolyte circulation control. Here, the recirculation rate should be chosen as low as possible to minimize the convective crossover of electrolysis products through mixing anolyte and catholyte. Furthermore, this crossover mechanism loses importance with a growing electrolysis plant size or electrode area as the gas production rate is increased, whereas the amount of recycled species stays equal at identical electrolyte flow rates.

Additionally, it could be demonstrated before [7] that periodic switching between mixed and separated cycles is capable of reducing the mean anodic hydrogen content while maintaining an equal electrolyte concentration in the anolyte and catholyte. It may also be conceivable that electrolysis is carried out with separated cycles under part-load operation, whereas a merging of the cycles is initiated as soon as a specific minimum current density is exceeded.

Eventually an advanced mixing appliance is proposed in Tab. 5.2. This could be realized by an additional electrolyte mixing tank equipped with an ion-exchange membrane that still enables an equalization of the anodic and cathodic electrolyte concentration. Consequently, the transport of cycled gas bubbles could be prevented. Furthermore, crossover due to the transport of dissolved species into the opposite half cell can be reduced in comparison to the direct mixing of anolyte and catholyte as the applied membrane serves as an additional diffusion barrier.

5.6 Conclusions

This study provides a summary of the crossover mechanisms occurring in PEM and alkaline water electrolysis and experimentally investigates the influence of current density, system pressure and various process management strategies on the resulting gas purity. In addition, reference measurements for the determination of purely diffusive crossover in both technologies are conducted. For a fair comparison of the two technologies, a uniform

Tab. 5.2: Approaches for crossover reduction and negative consequences in PEM (left) / AEL (right). Meaning of the symbols: ++ very effective, + good, o no effect or slightly positive / negative, - negative, - - very negative, ? effect cannot be estimated.

	H_2 in O_2 (safety)	Degradation	Faraday	Performance	Cost
1. Separating unit					
a) advanced materials with high ionic conductivity and low permeability [63, 64]	+/o	?/?	+/o	++/+	?/?
b) thicker separating units	+/o	+/o	+/o	- -/- -	-/-
2. Recombination catalyst					
a) external recombination [8]	+/+	o/o	o/o	o/o	-/-
b) on the backing layers [8] (PTL, bipolar plate)	+/+	o/o	o/o	o/o	-/-
c) within the catalyst layer / electrode [9]	++/+	?/?	?/o	o/o	-/-
d) within the membrane / separator	+/+	?/o	o/o	-/o	-/-
3. Supersaturation					
a) improved catalyst layers / electrodes, less transport resistances	++/+	+/o	+/+	++/++	o/o
b) ultrasonic field [67]	+/+	?/?	+/+	+/+	- -/- -
c) magnetic field [51, 68, 73–76]	+/?	?/?	+/?	+/+	- -/- -
d) super gravity field [69, 77]	?/?	?/?	?/?	+/+	- -/- -
4. Interlayer					
a) thin layers / sheets that are capable for the ionic transport, but gas-tight [70, 71]	++/o	+/o	++/o	?/o	-/-
b) 3rd / 4th electrode [72]	++/+	?/?	+/+	-/-	- -/- -
5. Process management (AEL)					
a) advanced gas / liquid separators	/+	/o	/+	/o	/-
b) mixing strategies [7, 55]	/++	/o	/+	/o	/o
c) advanced mixing appliances	/++	/o	/++	/o	/- -

operating temperature of 60 °C and state-of-the-art separating unit materials, Nafion 117 in PEM and Zirfon^{TM} in alkaline electrolysis, were chosen.

Generally the results of both technologies indicate that the anodic gas contamination increases significantly with decreasing current density and rising system pressure, which is mainly a consequence of increased dissolved gas concentration at elevated pressures. In fact, under specific operating conditions the determined hydrogen concentrations even exceeded 2 vol% in the anodic product gas stream, so that a safe plant operation was no longer possible. Here, the comparison of different process management strategies in AEL showed that the anodic hydrogen concentration is particularly influenced by mixing anolyte and catholyte, since a safe operation of the electrolyzer with separated cycles could be ensured at all investigated system pressures. Furthermore, the PEM experiments revealed that no distinction in the anodic hydrogen concentration is recognizable between balanced and differential pressure operation at an applied pressure gradient of 10 bar.

In a subsequent step the measured anodic hydrogen concentrations of both technologies were converted into permeation fluxes to illustrate the influence of current density and system pressure more clearly. As a result a linear increase of hydrogen permeation towards rising current densities could be observed in PEM electrolysis at all pressure levels. It is assumed that this linear growth is caused by a supersaturation of dissolved hydrogen, which is caused by mass transport resistances within the cathode catalyst layer. The supersaturation increases with current density, thus enhancing the diffusive permeation across the membrane. In comparison to the reference measurements, which showed no current density dependence of permeating hydrogen, supersaturation multiplied the diffusive crossover by a factor of 20 at a current density of 1 A cm^{-2} and a system pressure of 1 bar. However, the influence of supersaturation is seen to decrease with increasing system pressure. While the share on the overall crossover flux amounts to 98 % at 1 A cm^{-2} and 1 bar, only 53 % are determined at a pressure of 20 bar.

In contrast, the hydrogen permeation data of the alkaline experiments did not show such a clear dependency on the current density. However, it is observed at all investigated pressure stages that hydrogen crossover initially also increases with rising current density until a maximum permeation flux is reached. Similarly to PEM electrolysis it is assumed that the diffusive crossover is enhanced by a supersaturated electrolyte. But this effect is presumed to lose influence at higher current densities as a greater proportion

of evolved hydrogen is directly transported into gas bubbles adhering to the electrode, which consequently limits the diffusive crossover flux. Electrolyte mixing represents the most influential crossover mechanism with a share of 90 % under atmospheric pressure conditions and a current density of $0.7\,\mathrm{A\,cm^{-2}}$. Consequently diffusion due to saturation and supersaturation only yields 1.4 % and 8.6 % for this experimental setup.

Overall, PEM electrolysis showed a more than one order of magnitude higher diffusive crossover flux than AEL, which is particularly a consequence of the significantly lower hydrogen solubility in concentrated potassium hydroxide solution. Therefore, this study also provides an estimation of the influence of the separating unit thickness on the expected anodic gas contamination. Due to the inversely proportional dependency of the hydrogen crossover on the membrane thickness, a strong increase of the anodic hydrogen contamination is evident with decreasing membrane thicknesses in PEM electrolysis. Contrarily, the estimation shows a huge optimization potential for a reduction of the separator thickness in AEL as no meaningful increase of the anodic hydrogen concentration is observable down to thicknesses of 100 µm as crossover is mainly influenced by electrolyte mixing.

Finally, this study provides a summary of possible mitigation strategies that could help to reduce hydrogen crossover or at least the anodic foreign gas content. To this end, literature references are mentioned in which initial investigations have already been reported.

Acknowledgements

The authors gratefully acknowledge the financial support by the Federal Ministry of Education and Research of Germany in the framework of PowerMEE (project number 03SF0536B) and the DFG in the framework of the projects INST 189/182-1 FUGG and TU 89/18-1.

List of symbols

a	specific surface area	$\mathrm{m^{-1}}$
A_{el}	cross-sectional electrode area	$\mathrm{m^2}$
A_{sep}	cross-sectional separating unit area	$\mathrm{m^2}$

c_{H_2}	dissolved hydrogen concentration	$mol\,m^{-3}$
c_{solv}	concentration of solvent within separating unit	$mol\,m^{-3}$
d	pore diameter of separating unit	m
d_b	gas bubble diameter	m
D_{H_2}	diffusion coefficient of dissolved hydrogen in solvent	$m^2\,s^{-1}$
F	Faraday constant, 96485	$A\,s\,mol^{-1}$
i	current density	$A\,m^{-2}$
k_L	mass transfer coefficient	$m\,s^{-1}$
K_{H_2}	hydrogen permeability coefficient	$mol\,Pa^{-1}\,m^{-1}\,s^{-1}$
K_{koz}	Kozeny constant	-
K_{sep}	hydraulic permeability	m^2
n_{drag}	drag coefficient	-
N_{H_2}	hydrogen flux	$mol\,m^{-2}\,s^{-1}$
N_{O_2}	oxygen flux	$mol\,m^{-2}\,s^{-1}$
p	absolute pressure	Pa
p_i	partial pressure of component i	Pa
R_{sep}	ohmic resistance of separating unit	$\Omega\,cm^2$
Re	Reynolds number	-
S_{H_2}	solubility of hydrogen in solvent	$mol\,Pa^{-1}\,m^{-3}$
T	temperature	K
u	velocity	$m\,s^{-1}$
u_{solv}	hydraulic velocity of solvent	$m\,s^{-1}$
$\dot{V}$	volumetric flow rate of electrolyte	$m^3\,s^{-1}$

Greek

δ_{sep}	separating unit thickness	m
ε	porosity	-
η	dynamic viscosity of solvent	$Pa\,s$
ν	kinematic viscosity of solvent	$m^2\,s^{-1}$
σ_{sep}	ionic conductivity	$S\,m^{-1}$
τ	tortuosity	-
Φ_{H_2}	anodic hydrogen fraction	-

Subscripts/Superscripts	
ano	anode
cat	cathode
conv	convective
cross	crossover
diff	diffusive
dp	differential pressure
drag	drag
eff	effective
mix	electrolyte mixing
perm	permeation
sep	separator
solv	solvent

References

[1] L. M. Gandia, R. Oroz, A. Ursua, P. Sanchis, P. M. Dieguez. Renewable hydrogen production: Performance of an alkaline water electrolyzer working under emulated wind conditions. *Energ Fuel*, 21(3):1699–1706, 2007. DOI: 10.1021/ef060491u.

[2] R. E. Clarke, S. Giddey, S. P. S. Badwal. Stand-alone PEM water electrolysis system for fail safe operation with a renewable energy source. *Int J Hydrogen Energ*, 35(3): 928–935, 2010. DOI: 10.1016/j.ijhydene.2009.11.100.

[3] M. Carmo, D. L. Fritz, J. Mergel, D. Stolten. A comprehensive review on PEM water electrolysis. *Int J Hydrogen Energ*, 38(12):4901–4934, 2013. DOI: 10.1016/j.ijhydene.2013.01.151.

[4] S. A. Grigoriev, V. I. Porembskiy, S. V. Korobtsev, V. N. Fateev, F. Auprête, P. Millet. High-pressure PEM water electrolysis and corresponding safety issues. *Int J Hydrogen Energ*, 36(3):2721–2728, 2011. DOI: 10.1016/j.ijhydene.2010.03.058.

[5] P. Trinke, B. Bensmann, R. Hanke-Rauschenbach. Current density effect on hydrogen

permeation in PEM water electrolyzers. *Int J Hydrogen Energ*, 42(21):14355–14366, 2017. DOI: 10.1016/j.ijhydene.2017.03.231.

[6] W. Hug, J. Divisek, J. Mergel, W. Seeger, H. Steeb. Highly efficient advanced alkaline electrolyzer for solar operation. *Int J Hydrogen Energ*, 17(9):699–705, 1992. DOI: 10.1016/0360-3199(92)90090-J.

[7] P. Haug, M. Koj, T. Turek. Influence of process conditions on gas purity in alkaline water electrolysis. *Int J Hydrogen Energ*, 42(15):9406–9418, 2017. DOI: 10.1016/j.ijhydene.2016.12.111.

[8] S. A. Grigoriev, P. Millet, S. V. Korobtsev, V. I. Porembskiy, M. Pepic, C. Etievant, C. Puyenchet, V. N. Fateev. Hydrogen safety aspects related to high-pressure polymer electrolyte membrane water electrolysis. *Int J Hydrogen Energ*, 34(14):5986–5991, 2009. DOI: 10.1016/j.ijhydene.2009.01.047.

[9] H. Ito, N. Miyazaki, M. Ishida, A. Nakano. Cross-permeation and consumption of hydrogen during proton exchange membrane electrolysis. *Int J Hydrogen Energ*, 41 (45):20439–20446, 2016. DOI: 10.1016/j.ijhydene.2016.08.119.

[10] M. Inaba, T. Kinumoto, M. Kiriake, R. Umebayashi, A. Tasaka, Z. Ogumi. Gas crossover and membrane degradation in polymer electrolyte fuel cells. *Electrochim Acta*, 51(26):5746–5753, 2006. DOI: 10.1016/j.electacta.2006.03.008.

[11] M. Chandesris, V. Médeau, N. Guillet, S. Chelghoum, D. Thoby, F. Fouda-Onana. Membrane degradation in PEM water electrolyzer: Numerical modeling and experimental evidence of the influence of temperature and current density. *Int J Hydrogen Energ*, 40(3):1353–1366, 2015. DOI: 10.1016/j.ijhydene.2014.11.111.

[12] M. Schalenbach. Corrigendum to "Pressurized PEM water electrolysis: Efficiency and gas crossover" [Int J Hydrogen Energy 38 (2013) 14921–14933]. *Int J Hydrogen Energ*, 41(1):729–732, 2016. DOI: 10.1016/j.ijhydene.2015.11.009.

[13] P. Trinke, B. Bensmann, R. Hanke-Rauschenbach. Experimental evidence of increasing oxygen crossover with increasing current density during PEM water electrolysis. *Electrochem Commun*, 82:98–102, 2017. DOI: 10.1016/j.elecom.2017.07.018.

[14] S. Al Shakhshir, X. Cui, S. Frensch, S. K. Kær. In-situ experimental characterization of the clamping pressure effects on low temperature polymer electrolyte membrane electrolysis. *Int J Hydrogen Energ*, 42(34):21597–21606, 2017. DOI: 10.1016/j.ijhydene.2017.07.059.

[15] A. Manabe, H. Domon, J. Kosaka, T. Hashimoto, T. Okajima, T. Ohsaka. Study on separator for alkaline water electrolysis. *J Electrochem Soc*, 163(11):3139–3145, 2016. DOI: 10.1149/2.0191611jes.

[16] P. Haug, B. Kreitz, M. Koj, T. Turek. Process modelling of an alkaline water electrolyzer. *Int J Hydrogen Energ*, 42(24):15689–15707, 2017. DOI: 10.1016/j.ijhydene.2017.05.031.

[17] Q. Duan, H. Wang, J. Benziger. Transport of liquid water through Nafion membranes. *J Membrane Sci*, 392-393:88–94, 2012. DOI: 10.1016/j.memsci.2011.12.004.

[18] Brochure Zirfon Perl UTP 500. `https://www.agfa.com/sp/global/en/binaries/ZirfonPerl_UTP500_tcm611-56748.pdf`. Accessed: 15 January 2018.

[19] T. Sakai, H. Takenada, N. Wakabayashi, Y. Kawami, E. Torikai. Gas permeation properties of solid polymer electrolyte (SPE) membranes. *J Electrochem Soc*, 132(6):1328–1332, 1985. DOI: 10.1149/1.2114111.

[20] M. K. Tham, R. D. Walker, K. E. Gubbins. Diffusion of oxygen and hydrogen in aqueous potassium hydroxide solutions. *J Phys Chem*, 74(8):1747–1751, 1970. DOI: 10.1021/j100703a015.

[21] B. Bensmann, R. Hanke-Rauschenbach, K. Sundmacher. In-situ measurement of hydrogen crossover in polymer electrolyte membrane water electrolysis. *Int J Hydrogen Energ*, 39(1):49–53, 2014. DOI: 10.1016/j.ijhydene.2013.10.085.

[22] T. Sakai, H. Takenaka, E. Torikai. Gas diffusion in the dried and hydrated Nafions. *J Electrochem Soc*, 133(1):88–92, 1986. DOI: 10.1149/1.2108551.

[23] M. Schalenbach, T. Hoefner, P. Paciok, M. Carmo, W. Lueke, D. Stolten. Gas permeation through Nafion. Part 1: Measurements. *J Phys Chem C*, 119(45):25145–25155, 2015. DOI: 10.1021/acs.jpcc.5b04155.

[24] M. Schalenbach, W. Lueke, D. Stolten. Hydrogen diffusivity and electrolyte permeability of the Zirfon PERL separator for alkaline water electrolysis. *J Electrochem Soc*, 163(14):1480–1488, 2016. DOI: 10.1149/2.1251613jes.

[25] F. Marangio, M. Santarelli, M. Cali. Theoretical model and experimental analysis of a high pressure PEM electrolyser for hydrogen production. *Int J Hydrogen Energ*, 34(3):1143–1158, 2009. DOI: 10.1016/j.ijhydene.2008.11.083.

[26] M. Schalenbach, M. Carmo, D. L. Fritz, J. Mergel, D. Stolten. Pressurized PEM water electrolysis: Efficiency and gas crossover. *Int J Hydrogen Energ*, 38(35):14921–14933, 2013. DOI: 10.1016/j.ijhydene.2013.09.013.

[27] H. Kim, M. Park, K. S. Lee. One-dimensional dynamic modeling of a high-pressure water electrolysis system for hydrogen production. *Int J Hydrogen Energ*, 38(6): 2596–2609, 2013. DOI: 10.1016/j.ijhydene.2012.12.006.

[28] P. Trinke, B. Bensmann, S. Reichstein, R. Hanke-Rauschenbach, K. Sundmacher. Hydrogen permeation in PEM electrolyzer cells operated at asymmetric pressure conditions. *J Electrochem Soc*, 163(11):3164–3170, 2016. DOI: 10.1149/2.0221611jes.

[29] J. Fimrite, B. Carnes, H. Struchtrup, N. Djilali. Transport phenomena in polymer electrolyte membranes - II. Binary friction membrane model. *J Electrochem Soc*, 152 (9):1815–1823, 2005. DOI: 10.1149/1.1952647.

[30] R. B. Evans, G. M. Watson. Gaseous diffusion in porous media at uniform pressure. *J Chem Phys*, 35(6):2076–2083, 1961. DOI: 10.1063/1.1732211.

[31] C. L. Young. *Hydrogen and deuterium*. Solubility data series, 5/6. Pergamon Press, Oxford, 1981.

[32] R. Wiebe, V. L. Gaddy. The solubility of hydrogen in water at 0, 50, 75 and 100 °C from 25 to 1000 atmospheres. *J Am Chem Soc*, 56(1):76–79, 1934. DOI: 10.1021/ja01316a022.

[33] P. Ruetschi, R. F. Amlie. Solubility of hydrogen in potassium hydroxide and sulfuric acid. Salting-out and hydration. *J Phys Chem*, 70(3):718–723, 1966. DOI: 10.1021/j100875a018.

[34] M. B. Knaster, L. A. Apel'baum. Solubility of hydrogen and oxygen in concentrated potassium hydroxide solution. *Russ J Phys Ch*, 38:120–122, 1964.

[35] D. R. Stull. Vapor pressure of pure substances. Organic and inorganic compounds. *Ind Eng Chem*, 39(4):517–540, 1947. DOI: 10.1021/ie50448a022.

[36] J. Balej. Water vapour partial pressures and water activities in potassium and sodium hydroxide solutions over wide concentration and temperature ranges. *Int J Hydrogen Energ*, 10(4):233–243, 1985. DOI: 10.1016/0360-3199(85)90093-X.

[37] P. Medina, M. Santarelli. Analysis of water transport in a high pressure PEM electrolyzer. *Int J Hydrogen Energ*, 35(11):5173–5186, 2010. DOI: 10.1016/j.ijhydene.2010.02.130.

[38] M. Mulder. *Characterisation of membranes*. Basic principles of membrane technology. Springer, Dordrecht, 1996.

[39] T. Ozgumus, M. Mobedi, U. Ozkol. Determination of Kozeny constant based on porosity and pore to throat size ratio in porous medium with rectangular rods. *Eng Appl Comp Fluid*, 8(2):308–318, 2014. DOI: 10.1080/19942060.2014.11015516.

[40] M. Schalenbach. Erratum: Hydrogen diffusivity and electrolyte permeability of the Zirfon PERL separator for alkaline water electrolysis [J. Electrochem. Soc., 163, F1480 (2016)]. *J Electrochem Soc*, 164(14):23, 2017. DOI: 10.1149/2.0051802jes.

[41] F. Barbir. PEM electrolysis for production of hydrogen from renewable energy sources. *Sol Energy*, 78(5):661–669, 2005. DOI: 10.1016/j.solener.2004.09.003.

[42] B. Bensmann, R. Hanke-Rauschenbach, I. K. Peña Arias, K. Sundmacher. Energetic evaluation of high pressure PEM electrolyzer systems for intermediate storage of renewable energies. *Electrochim Acta*, 110:570–580, 2013. DOI: 10.1016/j.electacta.2013.05.102.

[43] B. Bensmann, R. Hanke-Rauschenbach, G. Müller-Syring, M. Henel, K. Sundmacher. Optimal configuration and pressure levels of electrolyzer plants in context of power-to-gas applications. *Appl Energ*, 167:107–124, 2016. DOI: 10.1016/j.apenergy.2016.01.038.

[44] S. A. Grigoriev, A. A. Kalinnikov, P. Millet, V. I. Porembskiy, V. N. Fateev. Mathematical modeling of high-pressure PEM water electrolysis. *J Appl Electrochem*, 40 (5):921–932, 2010. DOI: 10.1007/s10800-009-0031-z.

[45] L. C. Jacobson, X. Ren, V. Molinero. Assessing the effects of crowding, pore size, and interactions on electro-osmotic drag coefficients. *J Phys Chem C*, 118(4):2093–2103, 2014. DOI: 10.1021/jp410910r.

[46] K. Onda, T. Murakami, T. Hikosaka, M. Kobayashi, R. Notu, K. Ito. Performance analysis of polymer-electrolyte water electrolysis cell at a small-unit test cell and performance prediction of large stacked cell. *J Electrochem Soc*, 149(8):1069–1078, 2002. DOI: 10.1149/1.1492287.

[47] V. Schroeder, B. Emonts, H. Janssen, H.-P. Schulze. Explosion limits of hydrogen/oxygen mixtures at initial pressures up to 200 bar. *Chem Eng Technol*, 27(8): 847–851, 2004. DOI: 10.1002/ceat.200403174.

[48] J. Eigeldinger, H. Vogt. The bubble coverage of gas-evolving electrodes in a flowing electrolyte. *Electrochim Acta*, 45(27):4449–4456, 2000. DOI: 10.1016/S0013-4686(00) 00513-2.

[49] R. J. Balzer, H. Vogt. Effect of electrolyte flow on the bubble coverage of vertical gas-evolving electrodes. *J Electrochem Soc*, 150(1):11–16, 2003. DOI: 10.1149/1.1524185.

[50] H. Vogt, G. Kreysa, S. Vasudevan, R. Wüthrich, J. D. Abou Ziki, R. El-Haddad. *Electrochemical Reactors*. Ullmann's Encyclopedia of Industrial Chemistry. Wiley-VCH, Weinheim, 2013. DOI: 10.1002/14356007.l09_l01.pub2.

[51] H. Matsushima, D. Kiuchi, Y. Fukunaka. Measurement of dissolved hydrogen supersaturation during water electrolysis in a magnetic field. *Electrochim Acta*, 54(24): 5858–5862, 2009. DOI: 10.1016/j.electacta.2009.05.044.

[52] K. Kikuchi, H. Takeda, B. Rabolt, T. Okaya, Z. Ogumi, Y. Saihara, H. Noguchi. Hydrogen particles and supersaturation in alkaline water from an alkali–ion–water electrolyzer. *J Electroanal Chem*, 506(1):22–27, 2001. DOI: 10.1016/S0022-0728(01) 00517-4.

[53] H. Vogt. On the gas-evolution efficiency of electrodes I - Theoretical. *Electrochim Acta*, 56(3):1409–1416, 2011. DOI: 10.1016/j.electacta.2010.08.101.

[54] R. T. Ferrell, D. M. Himmelblau. Diffusion coefficients of hydrogen and helium in water. *AIChE J*, 13(4):702–708, 1967. DOI: 10.1002/aic.690130421.

[55] C. A. Schug. Operational characteristics of high-pressure, high-efficiency water-hydrogen-electrolysis. *Int J Hydrogen Energ*, 23(12):1113–1120, 1998. DOI: 10.1016/S0360-3199(97)00139-0.

[56] H. Vogt. The rate of gas evolution of electrodes - I. An estimate of the efficiency of gas evolution from the supersaturation of electrolyte adjacent to a gas-evolving electrode. *Electrochim Acta*, 29(2):167–173, 1984. DOI: 10.1016/0013-4686(84)87043-7.

[57] H. Vogt. Studies on gas-evolving electrodes: The concentration of dissolved gas in electrolyte bulk. *Electrochim Acta*, 30(2):265–270, 1985. DOI: 10.1016/0013-4686(85)80092-X.

[58] J. M. Chin Kwie Joe, L. J. J. Janssen, S. J. D. van Strelen, J. H. G. Verbunt, W. M. Sluyter. Bubble parameters and efficiency of gas bubble evolution for a chlorine-, a hydrogen- and an oxygen-evolving wire electrode. *Electrochim Acta*, 33(6):769–779, 1988. DOI: 10.1016/S0013-4686(98)80006-6.

[59] J. St-Pierre, N. Massé, M. Bergeron. Dissolved oxygen concentration in a divided rotating cylinder electrode reactor. *Electrochim Acta*, 40(8):1013–1024, 1995. DOI: 10.1016/0013-4686(94)00337-Z.

[60] M. Schalenbach, G. Tjarks, M. Carmo, W. Lueke, M. Mueller, D. Stolten. Acidic or alkaline? Towards a new perspective on the efficiency of water electrolysis. *J Electrochem Soc*, 163(11):3197–3208, 2016. DOI: 10.1149/2.0271611jes.

[61] H. Ito, T. Maeda, A. Nakano, H. Takenaka. Properties of Nafion membranes under PEM water electrolysis conditions. *Int J Hydrogen Energ*, 36(17):10527–10540, 2011. DOI: 10.1016/j.ijhydene.2011.05.127.

[62] P. Vermeiren, W. Adriansens, J. Moreels, R. Leysen. Evaluation of the Zirfon separator for use in alkaline water electrolysis and Ni-H_2 batteries. *Int J Hydrogen Energ*, 23(5):321–324, 1998. DOI: 10.1016/S0360-3199(97)00069-4.

[63] A. Albert, A. O. Barnett, M. S. Thomassen, T. J. Schmidt, L. Gubler. Radiation-grafted polymer electrolyte membranes for water electrolysis cells: Evaluation of key membrane properties. *ACS Appl Mater Inter*, 7(40):22203–22212, 2015. DOI: 10.1021/acsami.5b04618.

[64] C. K. Mittelsteadt, J. A. Staser. *Electrolyzer membranes*. Polymer Science: A Comprehensive Reference. Elsevier, 2012. DOI: 10.1016/B978-0-444-53349-4.00296-X.

[65] L. A. Diaz, J. Hnat, N. Heredia, M. M. Bruno, F. A. Viva, M. Paidar, H. R. Corti, K. Bouzek, G. C. Abuin. Alkali doped poly (2,5-benzimidazole) membrane for alkaline water electrolysis: Characterization and performance. *J Power Sources*, 312: 128–136, 2016. DOI: 10.1016/j.jpowsour.2016.02.032.

[66] M. R. Kraglund, D. Aili, K. Jankova, E. Christensen, Q. Li, J. O. Jensen. Zero-gap alkaline water electrolysis using ion-solvating polymer electrolyte membranes at reduced KOH concentrations. *J Electrochem Soc*, 163(11):3125–3131, 2016. DOI: 10.1149/2.0161611jes.

[67] S. Li, C. Wang, C. Chen. Water electrolysis in the presence of an ultrasonic field. *Electrochim Acta*, 54(15):3877–3883, 2009. DOI: 10.1016/j.electacta.2009.01.087.

[68] M. Lin, L. Hourng, C. Kuo. The effect of magnetic force on hydrogen production efficiency in water electrolysis. *Int J Hydrogen Energ*, 37(2):1311–1320, 2012. DOI: 10.1016/j.ijhydene.2011.10.024.

[69] M. Wang, Z. Wang, Z. Guo. Water electrolysis enhanced by super gravity field for hydrogen production. *Int J Hydrogen Energ*, 35(8):3198–3205, 2010. DOI: 10.1016/j.ijhydene.2010.01.128.

[70] S. M. Holmes, P. Balakrishnan, V. S. Kalangi, X. Zhang, M. Lozada-Hidalgo, P. M. Ajayan, R. R. Nair. 2D crystals significantly enhance the performance of a working fuel cell. *Adv Energy Mater*, 7(5):1601216, 2017. DOI: 10.1002/aenm.201601216.

[71] M. Breitwieser, T. Bayer, A. Büchler, R. Zengerle, S. M. Lyth, S. Thiele. A fully spray-coated fuel cell membrane electrode assembly using Aquivion ionomer with a graphene oxide/cerium oxide interlayer. *J. Power Sources*, 351:145–150, 2017. DOI: 10.1016/j.jpowsour.2017.03.085.

[72] M. Schalenbach, D. Stolten. High-pressure water electrolysis: Electrochemical mitigation of product gas crossover. *Electrochim Acta*, 156:321–327, 2015. DOI: 10.1016/j.electacta.2015.01.010.

[73] H. Lee, J. Tsau, C. Lee. HER catalytic activity of electrodeposited Ni-P nanowires under the influence of magnetic field. *J Nanomater*, 2013:1–9, 2013. DOI: 10.1155/2013/191728.

[74] H. Matsushima, T. Iida, Y. Fukunaka. Gas bubble evolution on transparent electrode during water electrolysis in a magnetic field. *Electrochim Acta*, 100:261–264, 2013. DOI: 10.1016/j.electacta.2012.05.082.

[75] D. Baczyzmalski, F. Karnbach, X. Yang, G. Mutschke, M. Uhlemann, K. Eckert, C. Cierpka. On the electrolyte convection around a hydrogen bubble evolving at a microelectrode under the influence of a magnetic field. *J Electrochem Soc*, 163(9):248–257, 2016. DOI: 10.1149/2.0381609jes.

[76] L. Elias, A. Chitharanjan Hegde. Effect of magnetic field on HER of water Electrolysis on Ni–W alloy. *Electrocatalysis*, 8(4):375–382, 2017. DOI: 10.1007/s12678-017-0382-x.

[77] H. Matsushima, D. Kiuchi, Y. Fukunaka, K. Kuribayashi. Single bubble growth during water electrolysis under microgravity. *Electrochem Commun*, 11(8):1721–1723, 2009. DOI: 10.1016/j.elecom.2009.07.009.

6 Concluding discussion

In this work alkaline water electrolysis was investigated as a technological option for the future sustainable hydrogen supply. Research on water electrolysis technologies has increased considerably in recent years, as it is considered a key technology in the PtG concept. For a successful realization of this concept, exact knowledge of the electrolysis system behavior, even under dynamic conditions, is therefore mandatory.

It was the special aim of this thesis to examine the product gas quality influencing parameters quantitatively and to derive optimization potentials. This is of particular importance as safety issues may arise, when electrolyzers are operated at small loads or current densities, respectively. This can be attributed to crossover mechanisms that lead to a contamination of the product gases, hydrogen and oxygen, with the respective other gas. However, gas crossover does not only cause safety issues, but may also promote degradation of the applied electrodes. Consequently, there is great interest in the reduction of gas crossover, as not only safety issues can be minimized, but also an increase in efficiency is possible to achieve.

This constitutes the basic motivation for this work. In order to identify influencing factors and to determine possible improvements, experimental investigations were carried out and a mathematical model was developed to provide information on the predominant crossover mechanisms. The experimental part of this work can basically be divided into two main experimental sets. While the experiments under atmospheric pressure were conducted in a custom-built laboratory test bench, product gas compositions at a system pressure of up to 20 bar were determined in a purposely designed commercial electrolyzer. The majority of these results have been published in peer-reviewed scientific journals, which are a core element of this manuscript. Apart from a summary of these results, this final chapter is further intended to also present unpublished findings. Therefore, the experimental determination of the hydraulic permeability of a Zirfon^{TM} separator is

described first, before the occuring crossover mechanisms, the influence of various process conditions and management strategies are summarized and an outlook for future work is given afterwards.

6.1 Permeability determination

In chapter 5.3 the crossover mechanisms occurring in alkaline water electrolysis have been described in detail. One of these mechanisms is the convective permeation of electrolyte through the separator due to the presence of a total pressure gradient between the half cells. Since the electrolyte contains dissolved species, this results in a contamination of the evolving product gases. Usually the magnitude of this permeation flux is described by the application of Darcy's law (Eq. (5.17)), which necessitates the hydraulic permeability K_{sep} of the porous separator. As this value was still unknown when the manuscript of chapter 5 was published, measurements were carried out to determine the hydraulic permeability of Zirfon$^{\text{TM}}$ Perl UTP 500 afterwards.

For this purpose, the apparatus shown schematically in Fig. 6.1 was used. It was provided by the Department of Inorganic Technology of the University of Chemistry and Technology Prague.

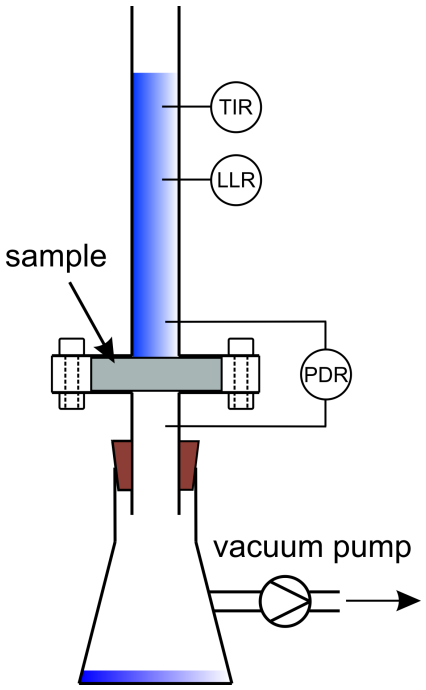

Fig. 6.1: Schematic illustration of the apparatus for the determinaton of the hydraulic permeability of porous separator materials.

The material of interest (sample) had to be inserted into a test cell whose inlet was pressurized through a vertical water column with a height of about 1 m and a temperature of 24.0 °C. The output of the cell, on the other hand, was connected to a vacuum pump (KNF LABOPORT N 816.3 KT.18) by which the test sample could be subjected to different pressure gradients. With this setup three consecutive series of measurements were carried out, in which the separator with a circular area of $A_{\mathrm{sep}} = 0.968\,\mathrm{cm}^2$ was exposed to differential pressures between $|\Delta p| = 150\,\mathrm{mbar}$ - $500\,\mathrm{mbar}$. The absolute differential pressure across the separator can be calculated from the sum of the inlet pressure $p_{\mathrm{H_2O}}$ (water column) and the outlet pressure p_{vac} (negative pressure generated by vacuum pump).

$$|\Delta p| = p_{\mathrm{H_2O}} + p_{\mathrm{vac}} \tag{6.1}$$

This differential pressure causes water to flow through the separator material, which reduces the height of the water column. By measuring the change of the water column height Δh in certain time steps (here: every 5 min), it is possible to determine the resulting volumetric flow rate $\dot{V}$ as a function of the differential pressure. The obtained measurement data are shown in Fig. 6.2 and approximated by a linear fit.

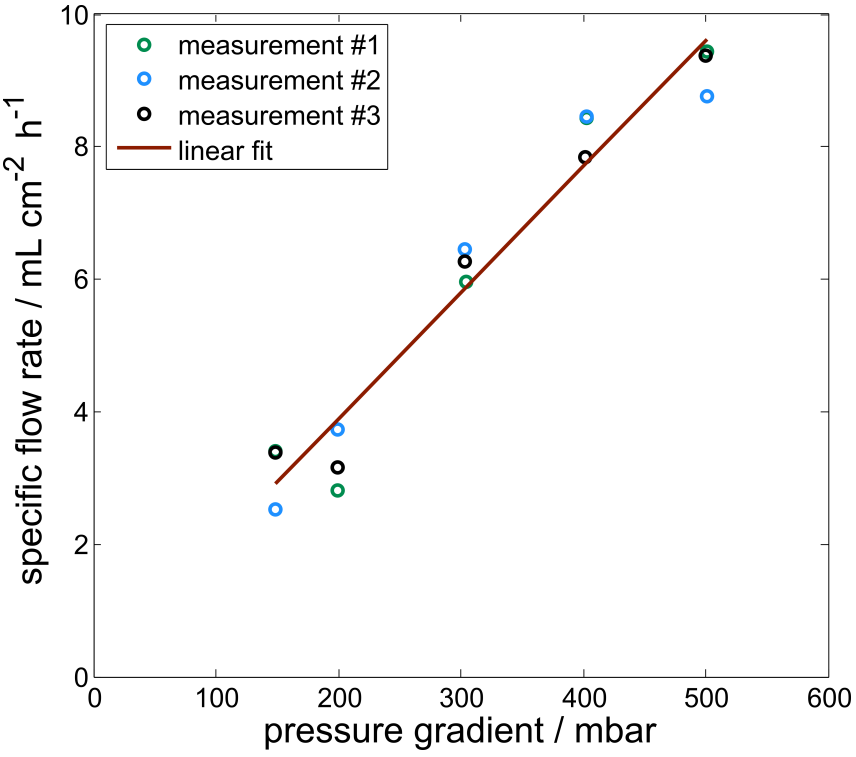

Fig. 6.2: Dependency of the specific volumetric water flow rate through a Zirfon$^{\mathrm{TM}}$ separator on the differential pressure.

With these data and the known dynamic viscocity of water $\eta = 0.9107\,\mathrm{mPa\,s}$ at $24.0\,^{\circ}\mathrm{C}$ [47] and a separator thickness of $\delta_{\mathrm{sep}} = 504\,\mu\mathrm{m}$, the permeability of the material can be determined through the rearrangement of Darcy's law.

$$K_{\mathrm{sep}} = \frac{\dot{V} \cdot \eta \cdot \delta_{\mathrm{sep}}}{A_{\mathrm{sep}} \cdot \Delta p} \tag{6.2}$$

Consequently, a hydraulic permeability of $K_{\mathrm{sep}} = 2.46 \cdot 10^{-16}\,\mathrm{m}^2 \pm 12.3\,\%$ is obtained as an average over all measuring points for Zirfon$^{\mathrm{TM}}$. This value shows good agreement with the thereotically estimated value in chapter 5.3.2, as well as experimental data from Schalenbach [48], who determined the permeability to lie between $6 \cdot 10^{-16}\,\mathrm{m}^2$ and $1 \cdot 10^{-15}\,\mathrm{m}^2$. Thus, this value can be taken as a reliable estimate for the future calculation of pressure-driven permeation.

In comparison, values of about $10^{-20}\,\mathrm{m}^2$ are given for Nafion in the literature [49]. Therefore, it can be concluded that the pressure-driven permeation of hydrogen and oxygen can actually be reduced if membrane materials are applied. However, it still needs to be examined to what extent the diffusive mass transfer is influenced by ion exchanging membranes.

6.2 Crossover mechanisms

In principle, gas crossover occurring in alkaline water electrolysis can be divided into diffusive and convective mass transfer mechanisms.

Diffusion. Diffusion processes enable the product gases to pass through the separator and contaminate the other half cell. Until now, it is assumed that only dissolved gases can diffuse through the separator under atmospheric conditions, as the pores of Zirfon$^{\mathrm{TM}}$ are too small to allow gas bubbles to enter. However, this possibility has to be studied more thoroughly at higher electrolysis pressures, as the gas bubble diameter of the product gases shrinks towards elevated system pressures. In this work it could be shown experimentally and with the aid of mathematical process modelling that the assumption of a saturated electrolyte in vicinity of the separator is insufficient for a description of the observed diffusive crossover flux. Therefore, the hypothesis is suggested that the electrolyte has to be supersaturated, which increases the diffusive crossover significantly. Thus, the results of this work estimate an approximately 5 - 10 times higher amount of dissolved gas than theoretical calculations would suggest. Since the electrolysis products are initially

generated in the liquid phase, it is assumed that this supersaturation originates from mass transport limitations from the liquid into the gaseous phase. The results further indicate that the largest proportion of the formed products remain in the liquid phase at low current densities, while higher current densities promote mass transport into the gaseous phase. A more comprehensive explanation of this phenomenon is provided in chapter 5.4.2. In this context, it was also found that the applied solubility model is of particular importance for a meaningful calculation of the diffusion processes and the product gas compositions, respectively. Here, the Setchenov relationship has proven to be a suitable way to accurately describe the decreasing gas solubility with increasing electrolyte concentrations. For the application of this equation measured data of Knaster and Apel'baum [50] were selected, from which the necessary Setchenov constants could be conducted.

Convective gas crossover can be divided into further mechanisms: Differential pressure, electrolyte mixing and electro-osmotic drag.

Differential pressure. One of these mechanisms is the crossover through the presence of a absolute pressure gradient between the anodic and cathodic half cell, which causes hydrogen and oxygen containing electrolyte to flow through the separator. While this mechanism is rather negligible under atmospheric pressure conditions, it becomes more important with increasing electrolysis pressure, since commercially available back pressure control valves provide an accuracy of roughly $\pm$ 1 % of the system pressure. In addition to the underlying pressure gradient, this mechanism is particularly influenced by the material properties of the separating unit. For instance, the convective crossover can be reduced by choosing separator materials with small hydraulic permeabilities or high thicknesses. However, the latter should be avoided due to the increase of the ohmic cell resistance. The present work cannot yet provide any specific predictions about the magnitude of this crossover mechanism as it is always superimposed by diffusion processes. Therefore, in order to evaluate the influence of this mechanism precisely, investigations should be carried out under variation of the differential pressure. However, the aforementioned hydraulic permeability of Zirfon^{TM} (cf. chapter 6.1) can be used as a first approximation in future calculations.

Electrolyte mixing. The mixing of the anodic and cathodic electrolyte cycles represents another convective crossover mechanism in alkaline water electrolysis in the broadest

sense. By mixing the cycles, dissolved species are transported into the opposite half-cell, where they outgas and contaminate the actual product. This process management strategy is necessary to maintain a constant electrolyte concentration and balanced liquid levels in the gas separators due to the different consumption and production of water in the half-cell reactions. The experiments and simulations carried out clearly show that electrolyte mixing accounts for the greatest proportion of gas crossover by far. Thus, under the process conditions mentioned in chapter 5.2.2, a share of about 90 % of the total hydrogen crossover could be determined experimentally for a current density range between $0.5\,\mathrm{kA\,m^{-2}}$ - $7\,\mathrm{kA\,m^{-2}}$ and atmospheric pressure. These experimental results are supported by simulation data, which also estimate an identical crossover share under the assumption of a gas-saturated electrolyte and similar process conditions (cf. chapter 4.4.5). Thus, this crossover mechanism provides high optimization potential for the improvement of the partial load range of alkaline electrolyzers. It can be assumed that an increase in electrolysis pressure further extends this potential, as not only the quantity of dissolved gas increases, but also smaller gas bubbles are produced, which are more difficult to separate.

Electro-osmotic drag. Furthermore, the electro-osmotic drag is another convective permeation mechanism. Due to the electric field in the electrolysis cell, ions move through the separator, which drag solvent and dissolved species with them. Since the ions in alkaline water electrolysis migrate from the cathodic to the anodic compartment, it is assumed that this mechanism could increase hydrogen permeation and reduce the crossover of oxygen. However, this mechanism was not examined in detail in this study as it is assumed to be negligible unter usual electrolysis conditions. This assumption can be made by the analysis of Eq. (5.20), which only suggests a small flow of dragged electrolyte through the separator.

Thus, within the framework of this work, electrolyte mixing and diffusion through the separator could be identified as decisive crossover mechanisms in alkaline water electrolysis. Therefore, relevant process conditions and their influence on the presented crossover mechanisms will be discussed in the following.

6.3 Process conditions

Obviously, all the previously described mechanisms are influenced by adjustable process conditions, such as the electrolyte flow rate, concentration, temperature and pressure. Therefore, subsequently the impact of these process parameters on the product gas quality is illustrated in order to derive an optimized process window.

Flow rate. When the electrolyzer is operated with combined electrolyte cycles, the resulting product gas quality is considerably effected by the chosen electrolyte flow rate. Thus, experimental and simulative studies have clearly shown that an increase in the flow rate leads to a decline in product purity. Here, the results reveal a linear dependence between the product gas quality and electrolyte flow rate for a constant current density in the applied laboratory setup and under the selected process conditions. The decrease in product gas quality can be explained by the fact that the mixing of the electrolyte cycles at higher electrolyte flow rates leads to an increased supply of dissolved species into the half cells. In addition, it is conceivable that the residence time within the gas separators is no longer sufficient to ensure a proper separation of gas bubbles from the electrolyte. Accordingly, the volumetric flow rate should be chosen as low as possible in order to keep the contamination of the product gases small. However, a minimum flow rate still needs to be ensured in order to prevent the temperature rise within the electrolysis cell from exceeding certain limits. Furthermore, it should be considered that a reduction of the flow rate may lead to an increase of the electrode bubble coverage, which is accompanied by an increase in cell voltage. Consequently, it would be imaginable to select small flow rates at low current densities, as the overvoltages and the electrode bubble converages are also small in this region in order to achieve an increased product gas quality. If the current density is increased, however, the flow rate should be raised accordingly to account for the additional heat production and gas evolution rate.

Electrolyte concentration. Furthermore, the product gas quality can be significantly influenced by the choice of the electrolyte concentration, as this determines the maximum gas solubility in the electrolyte. Correspondingly, the gas solubility in the electrolyte decreases with an increase of its salt concentration, which is often referred to as salting-out effect. Since the dissolved gas concentration influences all diffusive and convective crossover mechanisms, an improvement in product gas quality can be achieved by increasing the electrolyte salt concentration. In addition, the diffusion coefficients of

hydrogen and oxygen in higher concentrated KOH solutions are reduced, which also leads to a decrease in diffusional crossover. A comparison of experimental and simulated product gas quality data for constant current densities in the range between 27 wt% - 35 wt% KOH is presented in chapter 4.4.3, which supports this hypothesis. However, it has to be considered that KOH solutions exhibit a maximum electrical conductivity in the range of about 30 wt% under usual electrolysis conditions. Accordingly, a further increase in the electrolyte concentration above this maximum leads to a decrease in cell performance and should therefore be avoided. It can further be concluded from these results, that novel alkaline electrolysis systems, which operate at low electrolyte concentrations or even with pure water, will strongly have to struggle with increased gas crossover. Thus, hydrogen solubility in 30 wt% KOH at 30 °C and a partial pressure of 1.013 bar is reduced by a factor of 8 in comparison to pure water.

Temperature. The temperature can also have a significant influence on the product gas quality, as many physical properties of the product gases and the electrolyte are temperature-dependent. However, in contrast to the previous process parameters, it is not so straightforward to make a prediction about the overall influence of temperature, as contradictory phenomena come into play here. In general, a decrease of the hydrogen and oxygen solubility in 30 wt% KOH can be observed if the temperature is raised from 21 °C to 75 °C according to Knaster and Apel'baum [50]. Nevertheless, this does not directly reflect a reduction of crossover, as a temperature increase is accompanied by rising binary diffusion coefficients or a smaller electrolyte viscosity, which would indicate an increase of the diffusive or differential pressure-driven crossover. These contrasts are also apparent in the obtained measurement data. Thus, an increase of the process temperature from 50 °C to 80 °C showed an improvement of the product gas quality under mixed electrolyte cycles. This behavior could also be proven by model calculations, which leads to the assumption that the gas solubility is responsible for the overall crossover using this process management. In contrast, higher temperatures lead to an increase of the product gas contamination when the electrolyzer is operated with separated electrolyte cycles, as the intensified diffusional crossover represents the decisive factor in this case. It is reported in the literature [51, 52] that higher temperatures lead to a decline of the product gas quality. However, it is not clearly defined whether the measurement data were obtained under separated or combined electrolyte cycles. However, this demonstrates that the

influence of temperature has to be specifically determined for each electrolyzer, as the diffusive and convective mass transfer mechanisms can make up different proportions of the entire crossover in individual systems.

Pressure. It is the advantage of pressurized water electolysis that subsequent compression stages can be avoided. In addition, the increase in electrolysis pressure could be capable of reducing the cell voltage, as the evolved gas bubbles exhibit smaller diameters and thus cover a reduced fraction of the electrode surface. However, it is questionable if the necessary cell voltage can be reduced by this effect, since the thermodynamic equilibrium voltage rises with an increase of system pressure. In the context of this work, no influence of the pressure on cell voltage was apparent. It could be deduced from this observation that the two effects neutralise each other. For a reliable conclusion it is necessary to carry out future investigations. Nevertheless, it was experimentally found that elevated pressures lead to a significant decrease of the product gas quality, since a larger amount of the product gases dissolves in the electrolyte as predicted by Henry's law. Accordingly, the diffusive and convective components of the entire crossover increase. Furthermore, smaller gas bubbles are more difficult to separate from the electrolyte, so that gaseous products may also be recycled to the electrolysis cell at higher pressures. Consequently, low system pressures should be selected for a small gas crossover.

Operation window. In summary, it can be concluded from the results of this study that a high electrolyte concentration and a low system pressure should be chosen for a reduction of gas crossover, since the solubility of the product gases in the electrolyte can thus be reduced. However, this does not have universal validity, as not only the product gas quality but also the voltage efficiency and the necessary downstream compressor power must be taken into account for the overall system efficiency. Nevertheless, it is possible to overcome safety problems that would otherwise involve the shutdown of the electrolyzer. Further measures leading to a decrease of crossover are the reduction of the electrolyte flow rate, as well as an increase of temperature, if the electrolyzer is operated with combined cycles. However, it should be noted that although the overall crossover can be reduced by elevated temperatures, the diffusive permeation flux is increased. Fig. 6.3 shows a summary of all described crossover mechanisms and also provides a recommendation for the choice of process parameters to reduce the respective fluxes.

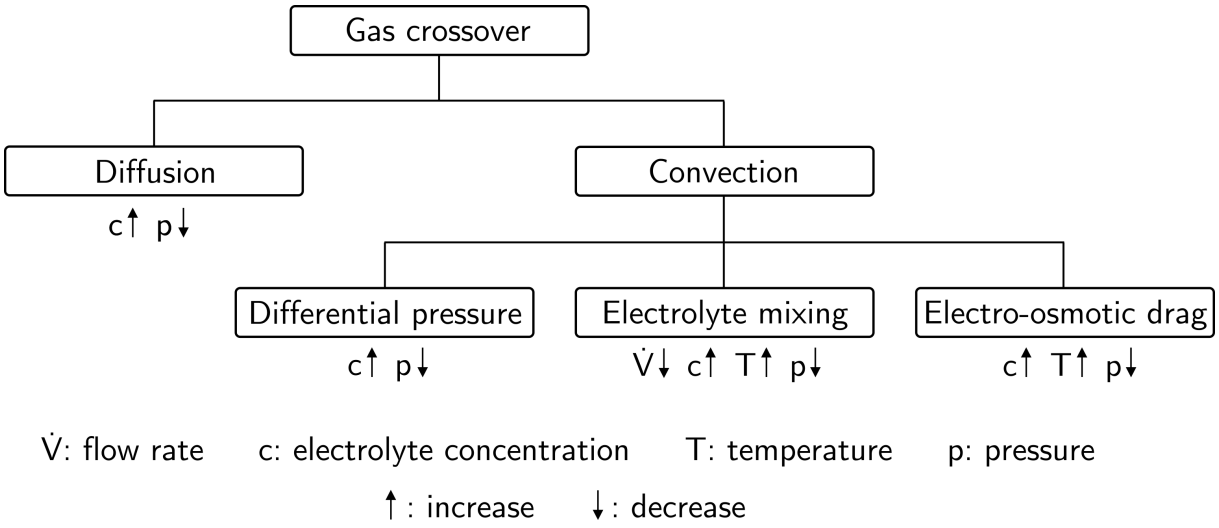

Fig. 6.3: Overview of crossover mechanisms with recommendation of process parameters for the reduction of each crossover flux.

6.4 Process management

In addition to an adjustment of the process parameters, it is also feasible to improve the product gas quality by a modification of the process management. Thus, a considerable reduction of the product gas contamination can be achieved by the simple separation of the anodic and cathodic electrolyte cycles, as the gas crossover through mixing of the cycles is completely avoided. In this case, only the diffusive and convective permeation fluxes through the separator cause contamination of the products. The experimental data showed that the electrolyzer could not be operated safely below $5\,\mathrm{kA\,m^{-2}}$ at 10 bar and mixed electrolyte cycles, as the safety limit of 2 vol% H_2 in O_2 was already reached. However, the separated operation enabled a determination of the anodic hydrogen content within the desired range from $1\,\mathrm{kA\,m^{-2}}$ - $7\,\mathrm{kA\,m^{-2}}$, as even at the lowest current density of $1\,\mathrm{kA\,m^{-2}}$ only a concentration of 0.372 vol% H_2 in O_2 was determined. This demonstrates that the separated operation is able to expand the partial-load regime of alkaline water electrolyzers substantially. However, this operation mode is only suitable for a limited period of time as the electrolyte concentration of the anolyte and catholyte is shifted towards a lower electrical conductivity, which is associated with a reduction of the voltage efficiency. Furthermore, the liquid levels in the gas separators change due to the different consumption and production of water in the half-cell reactions, which necessitates the occasional compensation of the levels.

Based on this knowledge, a dynamic process management strategy was developed that addresses the disadvantages of the separated operation mode. This strategy involves continuous switching between combined and separated cycles, which minimizes the aforementioned electrolyte concentration and liquid level shifts, while improving the mean product gas quality. For this purpose, a corresponding valve connection of the cycles is required, which allows such a process control. Within the scope of this work, only identical time periods for the combination and separation were investigated, which led to an oscillation of the anodic hydrogen content. The vertices of this concentration oscillation ranged between the stationary values of the two process variants, whereby the mean concentration approximately corresponded to the arithmetic average of both stationary values. An increase in the switching frequency led to a smaller amplitude, shorter oscillation period and an identical mean concentration. It can therefore be concluded that an increase in switching frequency flattens the amplitude even further so that a more or less constant output concentration can be achieved. A refinement of this process control could be the optimization of the times for mixing and separating the cycles. It is therefore conceivable that the cycles stay separated for a longer period in order to additionally improve the product gas quality. In this context, a simultaneous analysis of the product gas quality and the cell voltage is essential to maximize the system efficiency. An alternative operation strategy could also be the separation at low current densities and the merging of the cycles when a minimum required current density is exceeded.

Next to the modification of the proces management, it is also imaginable to modify or implement additional cell materials or to perform constructive measures, which promise a reduction of product permeation through the separator. An overview and description of possible mitigation strategies is provided in chapter 5.5.

6.5 Outlook

Finally, this study provides additional suggestions that could be of interest for a better understanding and further optimization of the process in future work. For this purpose, experiments and model adjustments should be carried out, which will be described in the following.

First of all, the experimental determination of the stationary product gas quality at elevated system pressures under variation of the electrolyte flow rate and the temperature would be useful, as no data are available yet. This allows a deeper insight into the influence of these parameters and provides a broader database for model adjustments. Besides a variation of these parameters, it might also be helpful to investigate alternative electrode geometries in a zero-gap arrangement, since it is conceivable that the dissolved gas concentration in vicinity of the separator is influenced by the prevailing flow conditions. In a further step, it would also be interesting to quantify the pressure-driven permeation flux as a function of the differential pressure. For this reason, the electrolysis cell needs to be equipped with an additional sensor for the exact determination of the differential pressure between the anodic and cathodic half-cells. However, precise knowledge of the diffusive crossover share is indispensable for this evaluation, which necessitates an apparatus that allows exact differential pressure control. Thus, the change of the total crossover could be measured and analyzed in depedence of the differential pressure. Further experiments that have to be conducted for an enhancement of the overall process understanding is the determination of various physical properties of the product gases in concentrated caustic potash solution. This includes the determination of the solubility and diffusion coefficients in the lye as well as typical separator materials under usual electrolysis conditions, as these are only partially available in the literature.

Firstly, the model presented in this work should be advanced by the system pressure as only simulations under atmospheric pressure are possible so far. Furthermore, it should be extended by the experimentally determined solubility and diffusion coefficients as well as the crossover mechanism due to differential pressure, which will allow a more precise prediction of the crossover shares and the product gas quality, respectively. In a second step, dynamic mass balances should be integrated into the model so that the experimentally presented dynamic process management strategies can also be reproduced. This would significantly simplify the optimization process by the prediction of ideal valve switching

intervals. Finally, an electrochemical model for the estimation of the individual cell resistances and the overall cell voltage should be implemented into the process model. Thus, a mathematical determination of the overall efficiency, which is influenced by the cell performance and the product gas quality becomes feasible. Through all these activities, it is eventually conceivable that a further improvement of the partial-load capability of alkaline water electrolyzers can be achieved.

References

[1] Energy Roadmap 2050, 2012. https://ec.europa.eu/energy/sites/ener/files/documents/2012_energy_roadmap_2050_en_0.pdf. Accessed: 08 June 2018.

[2] Energy 2020 - A strategy for competitive, sustainable and secure energy, 2011. https://ec.europa.eu/energy/sites/ener/files/documents/2011_energy2020_en_0.pdf. Accessed: 08 June 2018.

[3] Renewables 2018 - Global status report. http://www.ren21.net/wp-content/uploads/2018/06/17-8652_GSR2018_FullReport_web_-1.pdf. Accessed: 08 June 2018.

[4] M. Götz, J. Lefebvre, F. Mörs, A. McDaniel Koch, F. Graf, S. Bajohr, R. Reimert, T. Kolb. Renewable power-to-gas: A technological and economic review. *Renew Energ*, 85:1371–1390, 2016. DOI: 10.1016/j.renene.2015.07.066.

[5] J. Newton. Power-to-gas & methanation – Pathways to a »Hydrogen Economy«, 2014. http://www.apgtf-uk.com/files/workshops/14thWorkshop2014/212JohnNewton.pdf. Accessed: 09 June 2018.

[6] G. Gahleitner. Hydrogen from renewable electricity: An international review of power-to-gas pilot plants for stationary applications. *Int J Hydrogen Energ*, 38(5): 2039–2061, 2013. DOI: 10.1016/j.ijhydene.2012.12.010.

[7] T. Grundt, K. Christiansen. Hydrogen by water electrolysis as basis for small scale ammonia production. A comparison with hydrocarbon based technologies. *Int J Hydrogen Energ*, 7(3):247–257, 1982. DOI: 10.1016/0360-3199(82)90088-X.

[8] T. Smolinka, M. Günther, J. Garche. NOW-Studie: Stand und Entwicklungspotenzial der Wasserelektrolyse zur Herstellung von Wasserstoff aus regenerativen Energien. *Abschlussbericht*, 2011.

[9] K. Zeng, D. Zhang. Recent progress in alkaline water electrolysis for hydrogen production and applications. *Prog Energ Combust*, 36(3):307–326, 2010. DOI: 10.1016/j.pecs.2009.11.002.

[10] S. Satyapal. Hydrogen and Fuel Cells Overview, 2017. `https://www.energy.gov/sites/prod/files/2017/06/f34/fcto-h2-fc-overview-dla-worldwide-energy-conf-2017-satyapal.pdf`. Accessed: 11 June 2018.

[11] J. D. Holladay, J. Hu, D. L. King, Y. Wang. An overview of hydrogen production technologies. *Catal Today*, 139(4):244–260, 2009. DOI: 10.1016/j.cattod.2008.08.039.

[12] A. Godula-Jopek. *Introduction*. Hydrogen Production by Electrolysis. Wiley-VCH, Weinheim, 2015. DOI: 10.1002/9783527676507.ch1.

[13] G. Collodi. Hydrogen production via steam reforming with CO_2 capture. *Chem Engineer Trans*, 19:37–42, 2010.

[14] B. Decourt, B. Lajoie, R. Debarre, O. Soupa. Hydrogen-based energy conversion - More than storage: System flexibility. *SBC Energy Institute*, 2014.

[15] S. Trasatti. Water electrolysis: who first? *J Electroanal Chem*, 476(1):90–91, 1999. DOI: 10.1016/S0022-0728(99)00364-2.

[16] A. Ursua, L. M. Gandia, P. Sanchis. Hydrogen production from water electrolysis: Current status and future trends. *P IEEE*, 100(2):410–426, 2012. DOI: 10.1109/JPROC.2011.2156750.

[17] M. R. Kraglund, E. Christensen. Alkaline membrane water electrolysis with non-noble catalysts. *Kgs. Lyngby: Department of Energy Conversion and Storage, Technical University of Denmark*, 2017.

[18] M. Carmo, D. L. Fritz, J. Mergel, D. Stolten. A comprehensive review on PEM water electrolysis. *Int J Hydrogen Energ*, 38(12):4901–4934, 2013. DOI: 10.1016/j.ijhydene.2013.01.151.

[19] D. Pletcher, X. Li, S. Wang. A comparison of cathodes for zero gap alkaline water electrolysers for hydrogen production. *Int J Hydrogen Energ*, 37(9):7429–7435, 2012. DOI: 10.1016/j.ijhydene.2012.02.013.

[20] Y. Cheng, S. P. Jiang. Advances in electrocatalysts for oxygen evolution reaction of water electrolysis-from metal oxides to carbon nanotubes. *Prog Nat Sci-Mater*, 25 (6):545–553, 2015. DOI: 10.1016/j.pnsc.2015.11.008.

[21] L. M. Rodriguez-Valdez, I. Estrada-Guel, F. Almeraya-Calderon, M. A. Neri-Flores, A. Martinez-Villafane, R. Martinez-Sanchez. Electrochemical performance of hydrogen evolution reaction of Ni-Mo electrodes obtained by mechanical alloying. *Int J Hydrogen Energ*, 29(11):1141–1145, 2004. DOI: 10.1016/j.ijhydene.2003.11.005.

[22] J. Divisek, H. Schmitz, J. Balej. Ni and Mo coatings as hydrogen cathodes. *J Appl Electrochem*, 19(4):519–530, 1989. DOI: 10.1007/BF01022108.

[23] D. E. Brown, M. N. Mahmood, M. C. M. Man, A. K. Turner. Preparation and characterization of low overvoltage transition metal alloy electrocatalysts for hydrogen evolution in alkaline solutions. *Electrochim Acta*, 29(11):1551–1556, 1984. DOI: 10.1016/0013-4686(84)85008-2.

[24] X. Zhang, J. Hampshire, K. Cooke, X. Li, D. Pletcher, S. Wright, K. Hyde. High surface area coatings for hydrogen evolution cathodes prepared by magnetron sputtering. *Int J Hydrogen Energ*, 40(6):2452–2459, 2015. DOI: 10.1016/j.ijhydene.2014.12.107.

[25] C. C. L. McCrory, S. Jung, I. M. Ferrer, S. M. Chatman, J. C. Peters, T. F. Jaramillo. Benchmarking hydrogen evolving reaction and oxygen evolving reaction electrocatalysts for solar water splitting devices. *J Am Chem Soc*, 137(13):4347–4357, 2015. DOI: 10.1021/ja510442p.

[26] J. Suntivich, K. J. May, H. A. Gasteiger, J. B. Goodenough, Y. Shao-Horn. A perovskite oxide optimized for oxygen evolution catalysis from molecular orbital principles. *Science*, 334(6061):1383–1385, 2011. DOI: 10.1126/science.1212858.

[27] X. Li, F. C. Walsh, D. Pletcher. Nickel based electrocatalysts for oxygen evolution in high current density, alkaline water electrolysers. *Phys Chem Chem Phys*, 13(3): 1162–1167, 2011. DOI: 10.1039/C0CP00993H.

[28] J. OM. Bockris, T. Otagawa. The electrocatalysis of oxygen evolution on perovskites. *J Electrochem Soc*, 131(2):290–302, 1984. DOI: 10.1149/1.2115565.

[29] M. Hamdani, R. N. Singh, P. Chartier. Co_3O_4 and Co-based spinel oxides bifunctional oxygen electrodes. *Int J Electrochem Sc*, 5:556–577, 2010.

[30] F. Dionigi, P. Strasser. NiFe-based (oxy)hydroxide catalysts for oxygen evolution reaction in non-acidic electrolytes. *Adv Energy Mater*, 6(23), 2016. DOI: 10.1002/aenm.201600621.

[31] The European commission bans white asbestos. `http://europa.eu/rapid/press-release_IP-99-572_en.htm`. Accessed: 17 July 2018.

[32] Brochure Zirfon Perl UTP 500. `https://www.agfa.com/sp/global/en/binaries/ZirfonPerl_UTP500_tcm611-56748.pdf`. Accessed: 29 September 2016.

[33] J. Divisek, P. Malinowski, J. Mergel, H. Schmitz. Improved components for advanced alkaline water electrolysis. *Int J Hydrogen Energ*, 13(3):141–150, 1988. DOI: 10.1016/0360-3199(88)90014-6.

[34] H. Wendt, G. Imarisio. Nine years of research and development on advanced water electrolysis. A review of the research programme of the commission of the European communities. *J Appl Electrochem*, 18(1):1–14, 1988. DOI: 10.1007/BF01016198.

[35] I. Vincent, D. Bessarabov. Low cost hydrogen production by anion exchange membrane electrolysis: A review. *Renew Sust Energ Rev*, 81:1690–1704, 2018. DOI: 10.1016/j.rser.2017.05.258.

[36] L. A. Diaz, J. Hnat, N. Heredia, M. M. Bruno, F. A. Viva, M. Paidar, H. R. Corti, K. Bouzek, G. C. Abuin. Alkali doped poly (2,5-benzimidazole) membrane for alkaline water electrolysis: Characterization and performance. *J Power Sources*, 312:128–136, 2016. DOI: 10.1016/j.jpowsour.2016.02.032.

[37] M. R. Kraglund, D. Aili, K. Jankova, E. Christensen, Q. Li, J. O. Jensen. Zero-Gap Alkaline Water Electrolysis using ion-solvating Polymer Electrolyte Membranes at reduced KOH concentrations. *J Electrochem Soc*, 163(11):3125–3131, 2016. DOI: 10.1149/2.0161611jes.

[38] N. N. Greenwood, A. Earnshaw. *Cobalt, Rhodium and Iridium.* Chemistry of the Elements - Second Edition. Butterworth-Heinemann, Oxford, 1997.

[39] U. Babic, M. Suermann, F. N. Büchi, L. Gubler, T. J. Schmidt. Critical review - Identifying critical gaps for polymer electrolyte water electrolysis development. *J Electrochem Soc*, 164(4):387–399, 2017. DOI: 10.1149/2.1441704jes.

[40] P. Millet, S. A. Grigoriev. Electrochemical characterization and optimization of a PEM water electrolysis stack for hydrogen generation. *Chem Engineer Trans*, 41: 7–12, 2014. DOI: 10.3303/CET1441002.

[41] M. Rashid, M. Khaloofah Al Mesfer, H. Naseem, M. Danish. Hydrogen Production by Water Electrolysis: A Review of Alkaline Water Electrolysis, PEM Water Electrolysis and High Temperature Water Electrolysis. *IJEAT*, 4(3):80–93, 2015.

[42] Energiepark Mainz: Technische Daten. `http://www.energiepark-mainz.de/wissen/technische-daten/`. Accessed: 23 July 2018.

[43] M. Kopp, D. Coleman, C. Stiller, K. Scheffer, J. Aichinger, B. Scheppat. Energiepark Mainz: Technical and economic analysis of the worldwide largest Power-to-Gas plant with PEM electrolysis. *Int J Hydrogen Energ*, 42(19):13311–13320, 2017. DOI: 10.1016/j.ijhydene.2016.12.145.

[44] L. Bi, S. Boulfrad, E. Traversa. Steam electrolysis by solid oxide electrolysis cells (SOECs) with proton-conducting oxides. *Chem Soc Rev*, 43(24):8255–8270, 2014. DOI: 10.1039/C4CS00194J.

[45] W. Dönitz, E. Erdle. High-temperature electrolysis of water vapor - status of development and perspectives for application. *Int J Hydrogen Energ*, 10(5):291–295, 1985. DOI: 10.1016/0360-3199(85)90181-8.

[46] G. Tjarks, J. Mergel, D. Stolten. *Dynamic Operation of Electrolyzers – Systems Design and Operating Strategies.* Hydrogen Science and Engineering: Materials, Processes, Systems and Technology. Wiley-VCH, Weinheim, 2016. DOI: 10.1002/9783527674268.ch14.

[47] Viscosity of Water - viscosity table and viscosity chart. `https://wiki.anton-paar.com/en/water/`. Accessed: 02 February 2018.

[48] M. Schalenbach. Erratum: Hydrogen diffusivity and electrolyte permeability of the Zirfon PERL separator for alkaline water electrolysis [J. Electrochem. Soc., 163, F1480 (2016)]. *J Electrochem Soc*, 164(14):23, 2017. DOI: 10.1149/2.0051802jes.

[49] Q. Duan, H. Wang, J. Benziger. Transport of liquid water through nafion membranes. *J Membrane Sci*, 392-393:88–94, 2012. DOI: 10.1016/j.memsci.2011.12.004.

[50] M. B. Knaster, L. A. Apel'baum. Solubility of hydrogen and oxygen in concentrated potassium hydroxide solution. *Russ J Phys Ch*, 38:120–122, 1964.

[51] P. M. Dieguez, A. Ursua, P. Sanchis, C. Sopena, E. Guelbenzu, L. M. Gandia. Thermal performance of a commercial alkaline water electrolyzer: Experimental study and mathematical modeling. *Int J Hydrogen Energ*, 33(24):7338–7354, 2008. DOI: 10.1016/j.ijhydene.2008.09.051.

[52] A. Ursua, I. San Martin, E. L. Barrios, P. Sanchis. Stand-alone operation of an alkaline water electrolyser fed by wind and photovoltaic systems. *Int J Hydrogen Energ*, 38(35):14952–14967, 2013. DOI: 10.1016/j.ijhydene.2013.09.085.

Curriculum vitae

Personal details

Name	Haug, Philipp
Address	Viktoriastr. 53, 69126 Heidelberg
e-Mail	philipph198@gmail.com
Date of birth	05.12.1988
Place of birth	Lindau/Bodensee

Professional experience and education

since 09/2018	**Project Engineer**
	BASF SE, Ludwigshafen am Rhein
	Project Engineering E-FTE/ED
07/2014 - 06/2018	**Research assistant**
	TU Clausthal
	Institute of Chemical and Electrochemical Process Engineering
04/2012 - 06/2014	**Master of Science**
	TU Clausthal
	Process and Chemical Engineering
09/2008 - 03/2012	**Bachelor of Science**
	HAW Hamburg
	Process Engineering